RICE UNIVERSITY

Control Design and Stability Analysis of an Autonomous Gimbaled Engine Vehicle

by

Timothy Phillips, 2Lt USAF

A THESIS SUBMITTED
IN PARTIAL FULFILLMENT OF THE
REQUIREMENTS FOR THE DEGREE

Master of Science

APPROVED, THESIS COMMITTEE:

Pol Spanos, Chair
Mechanical Engineering & Materials Science

Andrew Meade
Mechanical Engineering & Materials Science

Andrew Dick
Mechanical Engineering & Materials Science

Nazareth Bedrossian
Mechanical Engineering & Materials Science

HOUSTON, TEXAS
MAY 2011

Abstract

Control Design and Stability Analysis of an Autonomous Gimbaled Engine Vehicle

by

Timothy Phillips

Robustly stable control architectures and designs are developed for autonomous flight of a gimbaled engine lander. The equations of motion describing the vehicle are linearized and stability analysis is performed to determine the optimally stable location of the propellant tanks relative to the airframe center of mass. Various controllers are designed to fly simulated planetary descent, x-prize, and hover trajectories. The various control designs apply a traditional Apollo approach as well as a new control design aiming to improve stability and performance. Optimal controller gains and filters are found for each design. Stability analysis is completed on the separate designs and simulated trajectories are flown in order to compare the performance of each design.

Acknowledgements

I would first like to thank my advisor Dr. Pol Spanos and Rice University for the opportunity to earn a graduate degree. Without Dr. Spanos and his guidance my education and this thesis would not have been possible. I would also like to thank Dr. Naz Bedrossian for his mentorship and help with conducting and completing the work of this thesis. The constant challenges presented to me added greatly to my academic experience. Special thanks to my friends and family who have supported me over the past two years. I would like to thank the Charles Stark Draper Laboratory for the ability to write this thesis. Thank you to all of the members of the Houston office for their help, especially to Jimmy Jang, Abran Alaniz, and Christine Appleby. I would like to extend many thanks to all of my friends and colleagues here at Rice University for all of their help and the great times that we had while here in Houston. I would like to offer special thanks to Wyatt Harris for the good memories down at Draper and for helping to create the 6DOF simulation and vehicle diagram we used in our theses. Wyatt's title as grand world champion of power point figure making while simultaneously reading Yahoo news and making personal phone calls is uncontested by anyone I have ever met. Thank you also to my roommate Matt for the good memories, adventures, and motorcycle rides, and for teaching me that it's ok to spend 2 hours in the gym every day. I would also like to thank Amy Davis for her support over the past year and for her help in editing the content of this thesis. I would finally like to thank everyone in my life that have supported me and helped me get to this point, without you I would not be where I am today.

The views expressed in this thesis are those of the author and do not reflect the official policy or position of the United States Air Force, Department of Defense, or the U.S. Government.

Contents

List of Figures

List of Tables

1 Introduction

The future exploration of the solar system and other celestial bodies is as much a challenge as it is a necessity. As mankind continues to grow and technology continues to advance both the need and ability for mankind to explore beyond the confines of this world will increase. However, before mankind can venture beyond the confines of the Earth and its' moon there will need to be further exploration by unmanned spacecraft to further investigate the solar system, blazing the trail for their manned counterparts to follow. An essential aspect for the success of these missions will be the ability of autonomy to succeed in conquering the harsh challenges of exploration. The extreme distances and environmental factors prohibit manual control of unmanned vehicles exploring the solar system. Therefore, the development of robust control designs for autonomous vehicles is critical to the success of these endeavors and to the future of exploration.

The most practical application of an autonomous vehicle is the exploration of a celestial body. This could include future missions to asteroids, moons, or even other planets. A powered descent vehicle is desirable because it allows the vehicle to land on the body of interest and still have the ability to takeoff continue exploring. This design allows the vehicle to maneuver, descend, land, and take-off again if necessary to explore other areas of interest to a particular mission. A typical design for a powered descent vehicle involves using a gimbaled rocket engine which can be used to control the attitude, pitch, and yaw of the vehicle. The gimbal motion allows the vehicle to rotate in both the pitch and the yaw directions and also translate in the vertical and horizontal directions.

A separate system of thrusters is typically used to control the roll of the vehicle which is usually not as significant as the control of pitch and yaw. Therefore, this thesis will restrict its focus to the design and analysis of control designs for the gimbaled engine since it is used as the primary control on the vehicle. The vehicle that will be considered is a 2-axis gimbaled rocket engine powered vehicle with four liquid propellant tanks centered on a fixed airframe.

1.1 Overview of GNC Architecture

In order for any vehicle to succeed in its mission, it will need to follow the commanded instructions it receives. The purpose of the Guidance, Navigation, and Control (GNC) system in the broadest sense is to figure out where the vehicle should be, where the vehicle is, and what to do to get the vehicle to where it should be. Guidance answers the question of where the vehicle should be by determining how it needs to command the vehicle in order to arrive at the correct destination. Navigation answers the question of where the vehicle is by using various sensors to determine the vehicle's state. Finally, Control answers the question of what to do to correct the vehicle to where it should be by determining the appropriate actuation to arrive at the desired state [1]. For the application of a gimbaled rocket engine vehicle these systems become more complicated but their overarching functions remain the same. The navigation subsystem determines the vehicles position, velocity, angular rotation, and angular rate using various sensors on the vehicle. The guidance subsystem uses the knowledge from the navigation subsystem and the desired trajectory to create throttle and directional commands to get the vehicle to the desired location. In between guidance and control is a steering block

which converts directional commands from guidance into vehicle attitude commands such as angular rotation and angular rate commands and/or position and velocity commands. The control subsystem compares the commanded attitude or state and throttle setting with the vehicle state estimates from the navigation subsystem in order to determine the appropriate gimbal angle and throttle setting to apply to the vehicle. A visual representation of a general GNC architecture is shown in Figure 1-1.

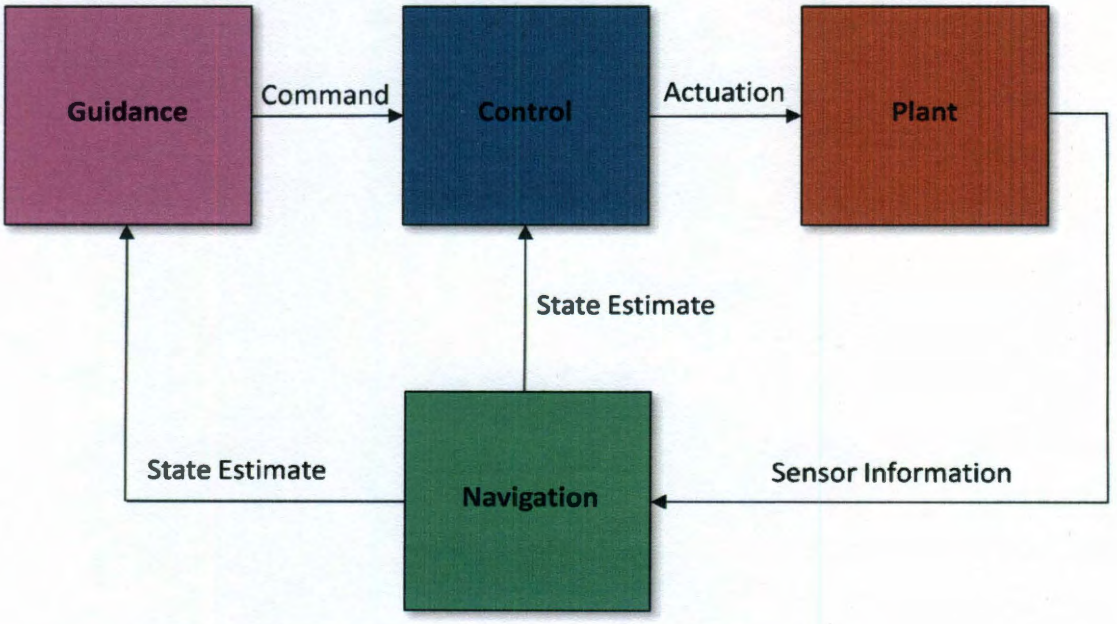

Figure 1-1: Overview of a General GNC Architecture

The GNC architecture allows the vehicle to autonomously fly a commanded trajectory in real-time.

1.2 Control Methods for Gimbaled Landers

There are several ways to approach the problem of control for a gimbaled engine lander. In order to control all degrees of freedom on the vehicle three controls are needed: a control on the throttle, a control on the gimbal angles of the engine, and a control on the

roll of the vehicle. The roll control on the lander is the least significant of the three controls because typical applications and trajectories do not require the vehicle to roll. For this reason, the focus of this thesis will be on the first two controls, throttle and engine gimbal. Roll control will be considered as a separate system that would be used to keep the vehicle from rolling. This thesis will examine the problem of gimbal and throttle control from a legacy perspective and propose a new approach to control design which offers several benefits over historical approaches.

1.2.1 Legacy Control Design

From a historical standpoint the problem of control for a descent vehicle has been viewed as a problem of correcting the attitude of the vehicle to point in a certain direction and to provide a necessary thrust to follow the trajectory. There are only a few historical examples of powered descent vehicles, the most famous of which being the Apollo Lunar Lander and it's designed but not flown modern successor Altair. The Apollo lander was not fully autonomous and the engine did not gimbal. A semi-autonomous system recommended the appropriate control to the pilot who served as the actual controller and the vehicle was rotated using roll control system jets instead of a gimbal [2]. The Altair vehicle design uses a gimbaled engine to control pitch and yaw, however, there is still manual control provided by a human pilot and therefore is not fully autonomous [3]. For these historical designs the direction the vehicle was commanded to point the vehicle in the proper direction to follow the trajectory. The thrust command was then determined by the guidance subsystem as the magnitude of the acceleration command. It was the responsibility of the controller to point the vehicle in the commanded direction by rotating the vehicle from its current state. In order to correct for error in the system, the

current position and velocity of the vehicle are fed back into the guidance subsystem which then uses that information to correct its pointing and thrust command [4]. A disadvantage of this approach is the thrust command is pre-determined by guidance therefore the controller is unable to change the thrust. Also, the controller has no knowledge of where it is or where it is trying to go. The controller only knows where it is supposed to point and where it is currently pointing. Although this design is simpler to understand it is not the most efficient way to solve the control problem. A visual representation of the typical legacy architecture is shown in Figure 1-2.

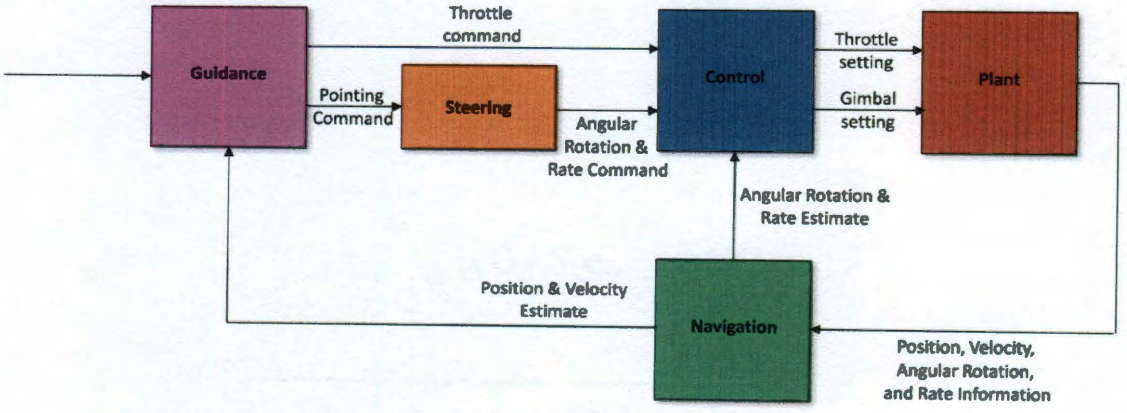

Figure 1-2: Overview of Legacy GNC Architecture

1.2.2 Proposed New Control Design

The proposed new control design corrects for several disadvantages of the legacy architecture and takes full advantage of the benefits of autonomy. The basic premise behind the new control design is to figure out where the vehicle would like to go in terms of position, velocity, and acceleration and then let the controller perform the work necessary to get it there.

The guidance block simply outputs a position and velocity command to the controller along with an acceleration direction which is predetermined and converted into a desired attitude by the steering block. The controller uses the angular rotation and rate information from navigation to point the vehicle in the commanded direction. However, the controller has the additional benefit of knowing position and velocity which it can reference with the commanded position and velocity of the trajectory. This not only allows the controller to accurately follow the trajectory by correcting for position and velocity errors, but it also allows the controller to determine the throttle command by referencing the error in the vehicle's vertical position. This design allows full control over the vehicle states to more accurately and robustly follow the trajectory. A general view of the new control design proposed by this thesis is shown in Figure 1-3.

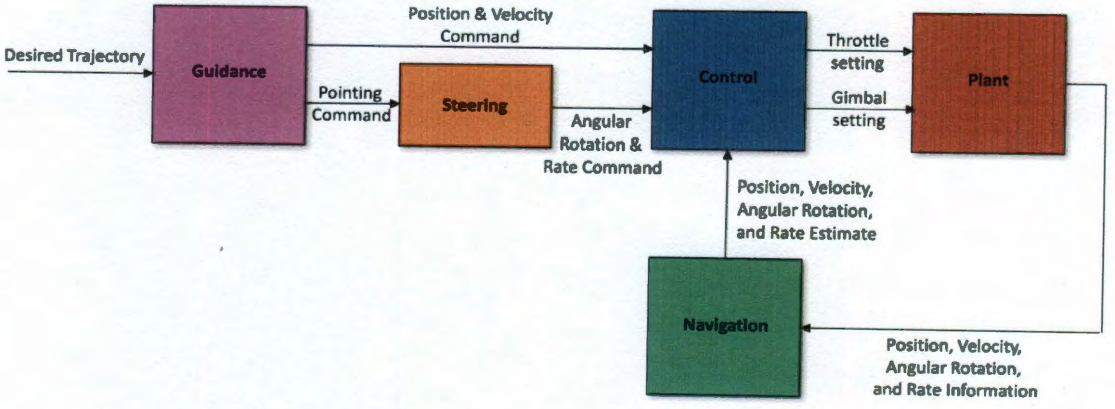

Figure 1-3: Overview of Proposed New GNC Architecture

This new approach has several benefits. The first main benefit is the controller is now able to adjust the throttle command as necessary. The throttle is no longer fixed by the guidance subsystem which is helpful from a thrust uncertainty robustness standpoint. The next major benefit is the guidance command can be run at a higher sampling rate

since it does not need to be updated on the fly and provides guaranteed stability margins whereas the traditional approach does not.

1.3 GNC Architecture subsystem comparison

In order to further understand the differences in the separate control designs it is important to understand the purpose of each of the components of the GNC architecture and how those change with the various designs. Due to the difference in designs not only are there significant differences in what each subsystem inputs and outputs but there are also differences in the responsibilities of the various GNC subsystems. The differences in the responsibilities of each of the subsystems are largely what create the advantages and disadvantages of each design.

1.3.1 Navigation

The purpose of navigation is to determine where the vehicle is at any given time. The navigation takes data from various vehicle sensors and calculates estimates for the vehicle's states [5]. In simulation the ideal knowledge of the states can be manipulated by various biases and errors to simulate realistic knowledge of the vehicle states. A comparison of the inputs and outputs of the navigation subsystem for each of the control designs is shown in Figure 1-4.

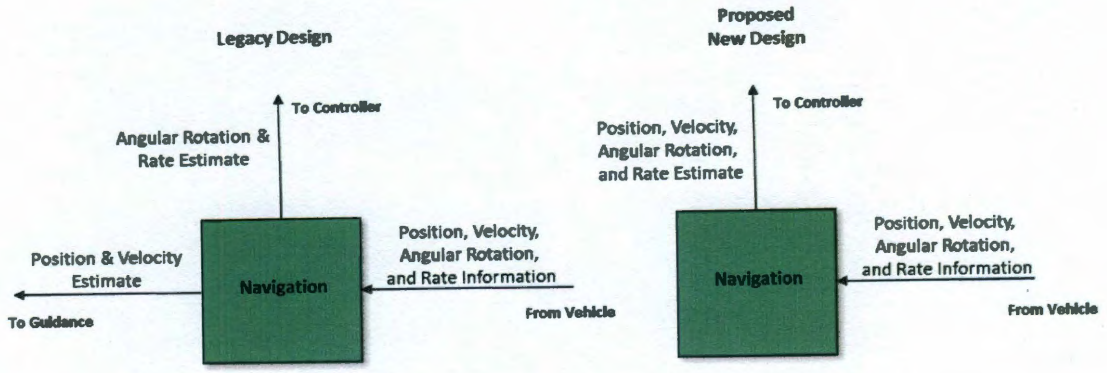

Figure 1-4: Overview of Navigation Subsystem Architectures

For both architectures the navigation subsystem takes in data from the vehicle sensors to determine the angular rotation and rate of the vehicle as well as the vehicle position and velocity. In the legacy design navigation passes the inertial position and velocity estimate to the guidance block so it can be used to update the guidance commands. The angular rotation and rate estimate is passed to the controller so the appropriate control can be applied to point the vehicle in the right direction. It is important to note there is no information going to the controller concerning the throttle setting. Therefore, the controller has no ability to adjust the throttle. In the proposed new design guidance no longer needs to position and velocity estimates from navigation. However, the inertial position and velocity are now also passed to the controller. This allows the controller to correct for both position and velocity errors as well as angular rotation and rate errors. Additionally, the throttle is now able to be controlled using inertial position information to determine the vertical position error of the vehicle.

1.3.2 Guidance

The responsibility of the guidance subsystem is generally to provide the commands to the system. Guidance essentially commands where the vehicle needs to go.

The guidance can be as simple as a fixed set of commands in order to fly a specified trajectory or as complex as recalculating the path to a specified target on the fly. Guidance can also include corrections by updating commands based off of state information. The various inputs and outputs of the guidance subsystem for each control design are shown in Figure 1-5.

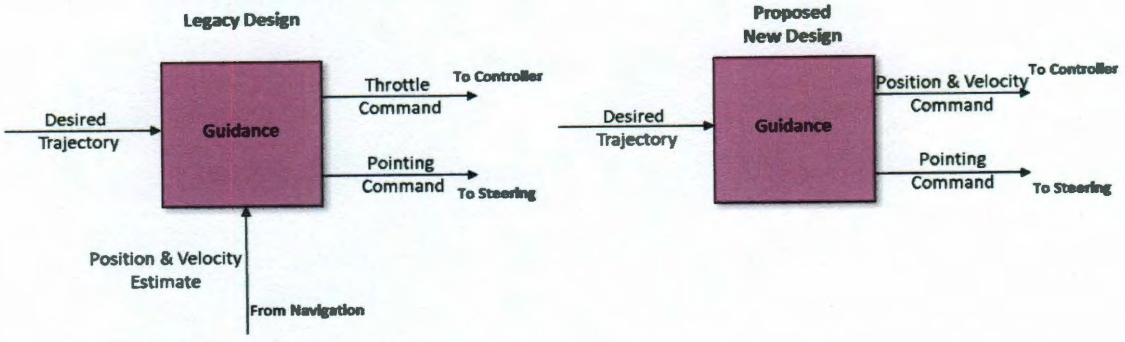

Figure 1-5: Overview of Guidance Subsystem Architectures

In the traditional Apollo approach the desired trajectory provides the main pointing command which is determined by the desired acceleration of the vehicle. This is accomplished through using a specified acceleration profile designed to place the vehicle at a specified state in a fixed time. The throttle is then determined by taking the magnitude of this acceleration. There is a correction to the acceleration using the error in position and velocity of the vehicle. This correction is inversely scaled by the time remaining until the target point is reached [6]. This is done to ensure the vehicle will reach the desired point at the desired time. The general acceleration command which determines vehicle direction and thrust is determined assuming a fixed time to target. In order to make the Apollo design more flexible the time to get to each target waypoint needs to be allowed to vary [7]. Selecting the algorithm to solve for the time to target essentially dictates the performance and optimality of the trajectory [8]. This is the

approach used in the legacy architecture. Guidance is given various waypoints and preplans a trajectory to arrive at the desired waypoints. The trajectory is then output in terms of a pointing and throttle command. There is an additional correction to these commands based off of real-time position and velocity error. In the proposed new control design architecture the guidance block simply takes the desired waypoints and outputs the desired position, velocity, and pointing direction based off the trajectory acceleration. There are no updates from guidance for error and no calculation of throttle setting.

1.3.3 Steering

The purpose of the steering block is to convert the pointing command from guidance which is in the form of an acceleration vector with unit magnitude into a commanded angular rotation and rate of the vehicle. The purpose of this system is purely the conversion of one form of a command into another form so guidance is essentially able to talk to the controller and vice versa. The inputs and outputs of the steering block do not change between control design architectures which can be seen below in Figure 1-6.

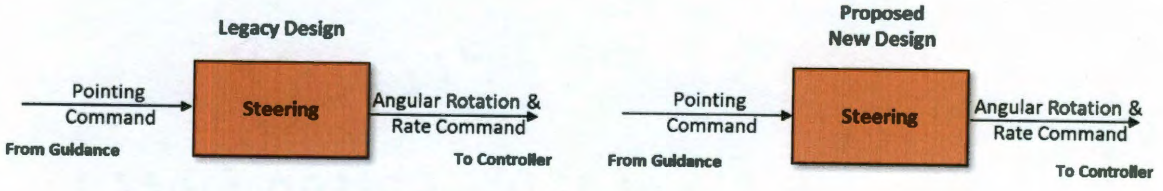

Figure 1-6: Overview of Steering Subsystem Architectures

1.3.4 Control

The purpose of the control subsystem is to apply the necessary inputs to the vehicle in order to fly the given trajectory. This is done by applying a control to eliminate the error between the commanded states and the actual states. In the Apollo program the controller referenced the desired angular rotation and rate which was determined by steering from the guidance command with the angular rotation and rate estimate given from the gimbal data through the navigation system. The angular rotation and rate command are adjusted through the guidance and steering blocks based off the position and velocity error [6]. The architectures for each of the control designs are shown in Figure 1-7.

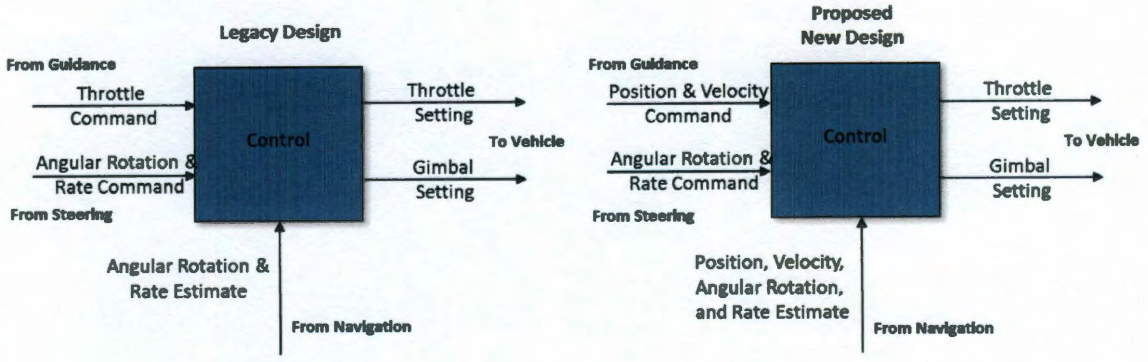

Figure 1-7: Overview of Control Subsystem Architectures

In the legacy design the throttle command is preset by the commanded acceleration from the guidance block. The controller only scales the acceleration by the vehicle mass estimate to provide the desired throttle setting. The angular rotation and rate command are referenced with the rotational state information from navigation in order to determine the gimbal angle setting to provide the necessary torque to rotate the vehicle to the desired orientation. In the new control design that is proposed by this thesis the controller

still references the desired vehicle rotation and rate with the angular state estimate from navigation to determine the gimbal angle. Additionally, in the new control design the controller determines the error in vehicle inertial position and velocity and determines the appropriate gimbal angle to provide a translational acceleration to correct the error. The gimbal controls from the rotational error and translational error are then combined to determine the appropriate overall gimbal angle. The thrust setting of the engine is determined by first commanding a thrust equal to that of the force of gravity in order to bias the throttle. Then the throttle setting is determined by referencing the desired vehicle altitude with the actual vehicle altitude and then adding this control to the biased thrust needed to balance the force of gravity.

1.4 Contributions

This thesis derives a full set of linear equations describing the motion of a gimbaled engine rocket with sloshing propellant mass. The linear set of equations is easily adapted to any gimbaled engine vehicle and has a significant variety of applications. This thesis provides a new control design to accurately control the gimbal and thrust of a gimbaled rocket. This control design uses a new architecture which offers greater overall stability and performance than previous designs. This thesis also provides an analysis of the optimal vehicle geometry for a gimbaled engine lander for vehicles with both spherical and cylindrical tanks.

2 Derivation of Linear Dynamics

It is essential to accurately predict and analyze the behavior of a gimbaled engine lander in order to design a control system capable of generating a desired response. In order to do this a model as close to the real world behavior of the system as possible is desired. The model is not only needed to predict the response of the system in order to design a control system for it, but it is also needed to test and verify the control system design before implementing it on the real system. The complexities of a fully accurate, non-linear model for a system as complex as a gimbaled engine rocket are magnified further when the problem of control is introduced. Therefore, a linear model is used to design and analyze controllers for the system. In order to create this linear model, the fully non-linear equations will be linearized in the sections below and simplifying assumptions will aid in producing a capable result.

2.1 Linearization

In order to accurately linearize the equations of motion for a system all non-linear terms need to be removed. These non-linear terms include bi-linear terms involving the coupling of two states as well as any non-constant terms of order greater than one. A critical component to accurately linearizing any equation is making sure terms are eliminated at the correct stage in the derivation. Eliminating terms before fully expanding the equations may result in neglecting important terms in the final linear equations. At the same time it is helpful to eliminate terms as soon as possible so as to avoid carrying unnecessary terms and avoid adding unnecessary complexity.

2.1.1 Methods of Linearization

The equations of motion can be linearized by eliminating higher order terms and nonlinear trigonometric functions. Methods for the linearization of equations of motion can be found in [9]. The linearization is accomplished through making appropriate assumptions to reduce the order of the equations of motion. Vehicle states such as translation and rotation as well as vehicle thrust are assumed to be constant. The assumptions in this linearization also include assuming that the effects of higher order terms are significantly small that they can be neglected and that angles are significantly small that trigonometric functions can become linear.

2.1.2 Small Angle Approximation

The small angle approximation is used to linearize trigonometric functions such as sine and cosine. These functions are periodic and therefore nonlinear however by assuming the angle within the function is significantly small, the functions can be approximated in a linear form. Assume there is an angle of interest, θ in radians, for small angles the trigonometric functions sine and cosine can be approximated as [10]

$$\begin{aligned} \sin\theta &\approx \theta \\ \cos\theta &\approx 1. \end{aligned} \tag{2.1}$$

By making this approximation these previously periodic terms now become linear. In order to accurately apply this approximation it is important that the range of angles which can be considered significantly small be properly defined. For the purposes of this thesis the assumption will be made that the angle of the gimbal and the angle of the vehicle body do not exceed .1745 radians (~10 degrees). At angles of less than 10 degrees the error in making this approximation is significantly less than 1 percent.

2.2 Linearization of 6 Degree of Freedom Equations of Motion

In order to design and analyze the control designs a generic vehicle setup is assumed and equations of motion are derived. This vehicle is assumed to have a rigid airframe with a single gimbaled rocket engine for control. The vehicle is assumed to have four total spherical propellant tanks, 2 fuel tanks and 2 oxidizer tanks. The entire propellant mass in each individual tank is assumed to slosh in the lateral direction.

2.2.1 Problem Setup

Equations of motion are developed in the body frame to describe the full motion of this vehicle. The setup of the derivation of the nonlinear equations of motion is given by [11] as:

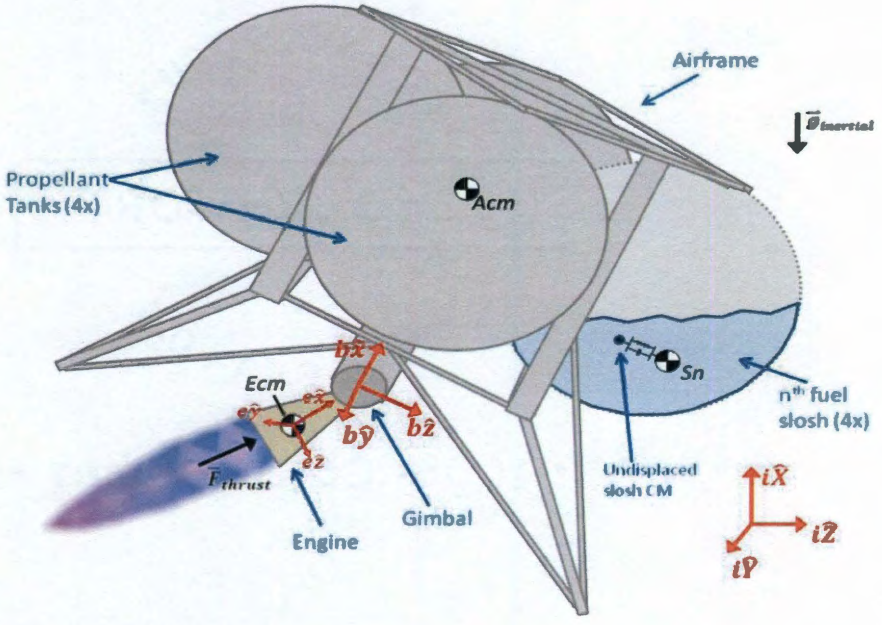

Figure 2-1: Vehicle Equation of Motion Problem Setup [11]

List of Terms:

Acm, Ecm, Sn -Airframe center of mass, engine center of mass, and n[th] slosh center of mass, respectively.

$\vec{r}^{\,\frac{Acm}{G}}, \vec{r}^{\,\frac{Ecm}{G}}$ -Position vector from body frame origin (rocket engine gimbal) to center of mass of airframe and engine respectively.

$\vec{l}_{sn}$ -Position vector from the gimbal to the undisplaced/equilibrium center of mass of *n*-th slosh mass.

$\vec{d}_{sn}$ -Displacement vector of *n*-th slosh mass from equilibrium position of associated slosh mass.

$\vec{r}^{\,\frac{Sn}{G}}$ - Position vector from body frame origin (rocket engine gimbal) to center of mass of *n*-th slosh mass:

$$\vec{r}^{\,\frac{Sn}{G}} = \vec{l}_{S_n} + \vec{d}_{S_n}$$

$\vec{r}^{\,\frac{Ccm}{G}}$ -Position vector from the gimbal to the composite center of mass of the entire system (including fuel):

$$\vec{r}^{\,\frac{Ccm}{G}} = \frac{m^a \vec{r}^{\,\frac{Acm}{G}} + m^e \vec{r}^{\,\frac{Ecm}{G}} + \sum_1^n m^{sn} \vec{r}^{\,\frac{Sn}{G}}}{m^t}$$

${}^i\vec{a}^g$ - Translational acceleration of the body frame origin (engine gimbal).

${}^i\vec{\alpha}^b$ - Angular acceleration of body frame about inertial frame.

${}^i\vec{\alpha}^e$ - Angular acceleration of engine frame about inertial frame.

${}^b\vec{\alpha}^e$ - Angular acceleration of engine frame about body frame:

$$ {}^{b}\vec{\alpha}^{e} = \begin{bmatrix} -\ddot{\beta}_y \sin(\beta_z) - \dot{\beta}_y \dot{\beta}_z \cos(\beta_z) \\ \ddot{\beta}_y \cos(\beta_z) - \dot{\beta}_y \dot{\beta}_z \sin(\beta_z) \\ \ddot{\beta}_z \end{bmatrix} $$

${}^{i}\vec{\omega}^{b}$ - Angular velocity of body frame about inertial frame.

${}^{i}\vec{\omega}^{e}$ - Angular velocity of engine frame about inertial frame.

${}^{b}\vec{\omega}^{e}$ - Angular velocity of engine frame about body frame:

$$ {}^{b}\vec{\omega}^{e} = \begin{bmatrix} -\dot{\beta}_y \sin(\beta_z) \\ \dot{\beta}_y \cos(\beta_z) \\ \dot{\beta}_z \end{bmatrix} $$

${}^{i}\vec{\varphi}^{b}$ - XYZ angle of rotation body frame to inertial frame.

${}^{b}\vec{\beta}^{e}$ - XYZ angle of rotation from engine frame to body frame:

$$ {}^{b}\vec{\beta}^{e} = \begin{bmatrix} 0 \\ \beta_y \\ \beta_z \end{bmatrix} $$

m^a - Mass of airframe.

m^e - Mass of engine.

m^{sn} - Equivalent mass of n-th slosh mass. For a spherical tank, the entire propellant mass is considered slosh.

m^t - Total mass of vehicle, including propellant (wet mass):

$$ m^t = m^a + m^e + \sum_{1}^{n} m^{sn} $$

$\underline{I}^{\overline{A}}_{\overline{Acm}}$ - Inertia dyadic of airframe about center of mass of airframe.

$\underline{I}^{\overline{E}}_{\overline{Ecm}}$ - Inertia dyadic of engine about center of mass of engine.

$\vec{g}_{body}$ - Acceleration due to gravity, in the body frame.

$\vec{F}_{thrust}$ - Thrust of rocket engine in the body frame.

$\vec{F}^{sys}$ - Sum of external forces on system in the body frame.

$\vec{M}^{\frac{sys}{ccm}}$ - Sum of external moments on system, about composite center of mass of the system.

$\vec{M}^{\frac{E}{G}}$ - Sum of external moments on engine, about gimbal.

$\vec{F}^{sn}$ - Sum of external forces on n-th slosh mass.

$\vec{\tau}_{\beta}$ - Torque applied by gimbal motor.

ω_{sn} - Equivalent frequency of n-th slosh mass.

ζ_{sn} - Equivalent damping ratio of n-th slosh mass.

2.2.2 Nonlinear Equations of Motion

The nonlinear equations of motion for the six degree of freedom system are given in [11]. They describe the motion of the vehicle in terms of six states: the translation of the vehicle in the body frame, the rotation of the vehicle in the body frame, and the displacements of the four slosh masses from their origin in the body frame. The equations of motion developed for the Saturn V rocket from [12], although simplified offer a good sanity check of the overall equations of motion for a gimbaled engine rocket. When the equations describing each degree of freedom of the vehicle are combined they fully describe the motion of the vehicle. In order to make them functional for purposes of design and analysis, the linear form of each equation is needed.

2.2.3 Derivation of Linear Equations

The derivations of the linear equations of motion for the vehicle are shown in the sections below. The linearization is performed using simplifying assumptions and linear algebra [13].

2.2.3.1 Linearization of Translational Acceleration of Body Equation

The linearization process will begin with the first equation which describes the translational acceleration of the body. The equation is given by [11] as

$$\begin{aligned} & m^t\ {}^i\vec{a}^G + \left(m^a\left(-\vec{r}^{\,Acm}_{\ G}\right)^x + m^e\left(-\vec{r}^{\,Ecm}_{\ G}\right)^x + \sum_1^n m^{sn}\left(-\vec{r}^{\,Sn}_{\ G}\right)^x\right)\ {}^i\vec{\alpha}^b + \\ & m^e\left(\vec{r}^{\,G}_{Ecm}\right)^x\ {}^b\vec{\alpha}^e + \sum_1^n m^{Sn}\ddot{\vec{d}}_{sn} = \vec{F}^{sys} - m^a\left(\ {}^i\vec{\omega}^b \times \left(\ {}^i\vec{\omega}^b \times \vec{r}^{\,Acm}_{\ G}\right)\right) - \\ & m^e\left(\left(\ {}^i\vec{\omega}^b \times\ {}^b\vec{\omega}^e\right) \times \vec{r}^{\,Ecm}_{\ G} +\ {}^i\vec{\omega}^e \times \left(\ {}^i\vec{\omega}^e \times \vec{r}^{\,Ecm}_{\ G}\right)\right) - \\ & \sum_1^n\left[m^{sn}\left(\ {}^i\vec{\omega}^b\left(2\dot{\vec{d}}_{sn} +\ {}^i\vec{\omega}^b \times \vec{r}^{\,Sn}_{\ G}\right)\right)\right], \end{aligned} \tag{2.2}$$

where:

$$\vec{F}^{sys} = {}^b\vec{F}_{thrust} + m^t\vec{g}_{body}. \tag{2.3}$$

As discussed previously, the most obvious nonlinear terms are higher order and bilinear terms where states are being multiplied with themselves or other states respectively. These terms are largely the $\omega \times \omega$ terms in the above equation. The bilinear and higher order terms can be seen as the underlined terms

$$\begin{aligned} & m^t\ {}^i\vec{a}^G + \left(m^a\left(-\vec{r}^{\,Acm}_{\ G}\right)^x + m^e\left(-\vec{r}^{\,Ecm}_{\ G}\right)^x + \sum_1^n m^{sn}\left(-\vec{r}^{\,Sn}_{\ G}\right)^x\right)\ {}^i\vec{\alpha}^b + \\ & m^e\left(\vec{r}^{\,G}_{Ecm}\right)^x\ {}^b\vec{\alpha}^e + \sum_1^n m^{Sn}\ddot{\vec{d}}_{sn} = \vec{F}^{sys} - m^a\underline{\left(\ {}^i\vec{\omega}^b \times \left(\ {}^i\vec{\omega}^b \times \vec{r}^{\,Acm}_{\ G}\right)\right)} - \end{aligned} \tag{2.4}$$

$$m^e\left(\underline{\left({}^i\vec{\omega}^b \times {}^b\vec{\omega}^e\right)} \times \vec{r}^{\,\frac{Ecm}{G}} + \underline{{}^i\vec{\omega}^e \times \left({}^i\vec{\omega}^e \times \vec{r}^{\,\frac{Ecm}{G}}\right)}\right) -$$

$$\Sigma_1^n\left[m^{sn}\left(\underline{{}^i\vec{\omega}^b \times \left(2\dot{\vec{d}}_{sn} + {}^i\vec{\omega}^b \times \vec{r}^{\,\frac{Sn}{G}}\right)}\right)\right].$$

Removing these terms under the linear approximation leaves the equation

$$m^t\ {}^i\vec{a}^G + \left(m^a\left(-\vec{r}^{\,\frac{Acm}{G}}\right)^{\times} + m^e\left(-\vec{r}^{\,\frac{Ecm}{G}}\right)^{\times} + \Sigma_1^n m^{sn}\left(-\vec{r}^{\,\frac{Sn}{G}}\right)^{\times}\right)\ {}^i\vec{a}^b + \tag{2.5}$$

$$m^e\left(\vec{r}^{\,\frac{G}{Ecm}}\right)^{\times}\ {}^b\vec{\alpha}^e + \Sigma_1^n m^{Sn}\ddot{\vec{d}}_{sn} = \vec{F}^{sys}\ .$$

Since there are no other obvious terms that can be removed, the next step is to expand the forcing term $\vec{F}^{sys}$. The translational forces on the system are given by the equation

$$\vec{F}^{sys} = {}^b\vec{F}_{thrust} + m^t\vec{g}_{body}. \tag{2.6}$$

The thrust force in the body frame is found by rotating the thrust in the engine frame into the body frame using a linearized body ZY rotation matrix. The full rotation matrix for the engine gimbal rotating about the z and y axes by their respective β gimbal angles is given by [14] as

$$Body\ ZY\ Rotation = \begin{bmatrix} \cos\beta_z\cos\beta_y & -\sin\beta_z & \sin\beta_y\cos\beta_z \\ \sin\beta_z\cos\beta_y & \cos\beta_z & \sin\beta_z\sin\beta_y \\ -\sin\beta_y & 0 & \cos\beta_y \end{bmatrix}. \tag{2.7}$$

Assuming the gimbal angles β_y and β_z are sufficiently small, the small angle approximation can be applied resulting in

$$Body\ ZY\ Rotation = \begin{bmatrix} 1*1 & -\beta_z & \beta_y*1 \\ \beta_z*1 & 1 & \beta_z*\beta_y \\ -\beta_y & 0 & 1 \end{bmatrix} = \begin{bmatrix} 1 & -\beta_z & \beta_y \\ \beta_z & 1 & 0 \\ -\beta_y & 0 & 1 \end{bmatrix}. \tag{2.8}$$

The linearized rotation of the engine frame into the body frame can then be used to find the thrust force in the body frame which is given as

$$ {}^{b}\vec{F}_{thrust} = \begin{bmatrix} 1 & -\beta_z & \beta_y \\ \beta_z & 1 & 0 \\ -\beta_y & 0 & 1 \end{bmatrix} \begin{bmatrix} F \\ 0 \\ 0 \end{bmatrix} = \begin{bmatrix} F \\ F\beta_z \\ -F\beta_y \end{bmatrix}. \tag{2.9} $$

The acceleration of gravity acting on the vehicle in the body frame is found by rotating the inertial gravity into the body frame. This can be done by making a linear approximation for the rotation of the body relative to the inertial frame. Let the angles describing the angular rotation of the vehicle be

$$ \begin{bmatrix} Roll\ Angle \\ Pitch\ Angle \\ Yaw\ Angle \end{bmatrix} = \begin{bmatrix} \emptyset_x \\ \emptyset_y \\ \emptyset_z \end{bmatrix}. \tag{2.10} $$

The next step is to define the gravitational constant, g, and to apply a linearized body zyx rotation. The full body zyx rotation matrix is given by [14] as

$$ \begin{bmatrix} \cos\emptyset_z \cos\emptyset_y & -\sin\emptyset_z \cos\emptyset_x + \sin\emptyset_y \sin\emptyset_x \cos\emptyset_z & \sin\emptyset_z \sin\emptyset_x + \sin\emptyset_y \cos\emptyset_z \cos\emptyset_x \\ \sin\emptyset_z \cos\emptyset_y & \cos\emptyset_z \cos\emptyset_x + \sin\emptyset_z \sin\emptyset_y \sin\emptyset_x & -\sin\emptyset_x \cos\emptyset_z + \sin\emptyset_z \sin\emptyset_y \cos\emptyset_x \\ -\sin\emptyset_y & \sin\emptyset_x \cos\emptyset_y & \cos\emptyset_y \cos\emptyset_x \end{bmatrix}. \tag{2.11} $$

Assuming that the rotation angles of the body are sufficiently small that the small angle approximation is valid, the rotation matrix becomes

$$ \begin{bmatrix} 1*1 & -\emptyset_z*1+\emptyset_y*\emptyset_x*1 & \emptyset_z*\emptyset_x+\emptyset_y*1*1 \\ \emptyset_z*1 & 1*1+\emptyset_z*\emptyset_y*\emptyset_x & -\emptyset_x*1+\emptyset_z*\emptyset_y*1 \\ -\emptyset_y & \emptyset_x*1 & 1*1 \end{bmatrix} = \begin{bmatrix} 1 & -\emptyset_z & \emptyset_y \\ \emptyset_z & 1 & -\emptyset_x \\ -\emptyset_y & \emptyset_x & 1 \end{bmatrix}. \tag{2.12} $$

This rotation matrix can then be applied to rotate the force of gravity from the inertial frame into the body frame,

$$ \vec{g}_{body} = \begin{bmatrix} 1 & -\emptyset_z & \emptyset_y \\ \emptyset_z & 1 & -\emptyset_x \\ -\emptyset_y & \emptyset_x & 1 \end{bmatrix} \begin{bmatrix} -g \\ 0 \\ 0 \end{bmatrix} = \begin{bmatrix} -g \\ -g\emptyset_z \\ g\emptyset_y \end{bmatrix}. \tag{2.13} $$

Combining equations (2.9) and (2.13) the linearized translational forces on the system become

$$\vec{F}^{sys} = \begin{bmatrix} F \\ F\beta_z \\ -F\beta_y \end{bmatrix} + m^t \begin{bmatrix} -g \\ -g\emptyset_z \\ g\emptyset_y \end{bmatrix} \tag{2.14}$$

Since the forces on the system are now in their fully linear form the next step is to expand the left side of equation (2.5) to ensure there are no other nonlinear terms that can be removed,

$$m^t {}^i\vec{a}^G + \left(m^a \left(-\vec{r}^{\frac{Acm}{G}} \right)^{\times} + m^e \left(-\vec{r}^{\frac{Ecm}{G}} \right)^{\times} + \sum_1^n m^{sn} \left(-\vec{r}^{\frac{Sn}{G}} \right)^{\times} \right) {}^i\vec{\alpha}^b + m^e \left(\vec{r}^{\frac{G}{Ecm}} \right)^{\times} {}^b\vec{\alpha}^e + \sum_1^n m^{Sn} \ddot{\vec{d}}_{sn}. \tag{2.15}$$

Although the vector from the gimbal to the engine center of mass in the body frame $\vec{r}^{\frac{Ecm}{G}}$ appears to be constant, it is actually varying with time. This is logical since as the engine gimbals the vector describing the location of its center of mass will change. However, with respect to the engine's own reference frame the vector to the engine's center of mass appears fixed. Therefore, the vector describing the location of the engine's center of mass can be found by first describing the location of the center of mass in the engine frame which is a constant value and then rotating it into the body frame. Assuming the gimbal rotation is significantly small and the engine center of mass is along the centerline of the engine, then the linearized rotation describing the location of the engine center of mass in the body frame is given by the equation

$$\vec{r}^{\frac{Ecm}{G}} = \begin{bmatrix} 1 & -\beta_z & \beta_y \\ \beta_z & 1 & 0 \\ -\beta_y & 0 & 1 \end{bmatrix} \begin{bmatrix} l_x{}^{\frac{Ecm}{G}} \\ 0 \\ 0 \end{bmatrix} = \begin{bmatrix} l_x{}^{\frac{Ecm}{G}} \\ l_x{}^{\frac{Ecm}{G}}\beta_z \\ -l_x{}^{\frac{Ecm}{G}}\beta_y \end{bmatrix}. \tag{2.16}$$

Since the equations of motion for the respective slosh masses describe their motion relative to their un-displaced locations the vector describing the position of the

slosh mass relative to the gimbal $\vec{r}^{\frac{Sn}{G}}$ is the combination of the fixed vector from the gimbal to the un-displaced slosh location and the displacement of the slosh,

$$\sum_n \vec{r}^{\frac{Sn}{G}} = \sum_n \begin{bmatrix} l_x^{\frac{Sn}{G}} \\ l_y^{\frac{Sn}{G}} \\ l_z^{\frac{Sn}{G}} \end{bmatrix} + \begin{bmatrix} 0 \\ d_{Sn_y} \\ d_{Sn_z} \end{bmatrix}. \tag{2.17}$$

The remaining vectors in the equation of motion are constant and therefore cannot be further expanded. Since all of the vectors have been properly defined it is now possible to define the cross product matrices for each vector. These cross product matrices are beneficial because they allow the cross product operation to be viewed as a simple matrix multiplication making it easier to visualize and if necessary cancel terms. The cross product matrix describing the constant varying vector to the airframe center of mass from the gimbal point is

$$\vec{r}^{\frac{Acm}{G}\times} = \begin{bmatrix} 0 & -r_z^{\frac{Acm}{G}} & r_y^{\frac{Acm}{G}} \\ r_z^{\frac{Acm}{G}} & 0 & -r_x^{\frac{Acm}{G}} \\ -r_y^{\frac{Acm}{G}} & r_x^{\frac{Acm}{G}} & 0 \end{bmatrix}. \tag{2.18}$$

The cross product matrix describing the time-varying varying vector to the engine center of mass from the gimbal point is given as

$$\vec{r}^{\frac{Ecm}{G}\times} = \begin{bmatrix} 0 & l_x^{\frac{Ecm}{G}}\beta_y & l_x^{\frac{Ecm}{G}}\beta_z \\ -l_x^{\frac{Ecm}{G}}\beta_y & 0 & -l_x^{\frac{Ecm}{G}} \\ -l_x^{\frac{Ecm}{G}}\beta_z & l_x^{\frac{Ecm}{G}} & 0 \end{bmatrix}. \tag{2.19}$$

The cross product matrix describing the time-varying vector to an individual sloshing propellant center of mass from the gimbal point is given as

$$\vec{r}_{G}^{Sn\times} = \begin{bmatrix} 0 & -l_z^{Sn}_{G} & l_y^{Sn}_{G} \\ l_z^{Sn}_{G} & 0 & -l_x^{Sn}_{G} \\ -l_y^{Sn}_{G} & l_x^{Sn}_{G} & 0 \end{bmatrix} + \begin{bmatrix} 0 & -d_{Sn_z} & d_{Sn_y} \\ d_{Sn_z} & 0 & 0 \\ -d_{Sn_y} & 0 & 0 \end{bmatrix}. \tag{2.20}$$

The cross product matrix describing the time-varying vector from the engine center of mass to the gimbal point is given as

$$\vec{r}_{Ecm}^{G\times} = \begin{bmatrix} 0 & -l_x^{Ecm}_{G}\beta_y & -l_x^{Ecm}_{G}\beta_z \\ l_x^{Ecm}_{G}\beta_y & 0 & l_x^{Ecm}_{G} \\ l_x^{Ecm}_{G}\beta_z & -l_x^{Ecm}_{G} & 0 \end{bmatrix}. \tag{2.21}$$

To accurately cancel all nonlinear terms these cross product matrices can now be substituted into equation (2.15) giving the expanded form of the left hand side of the equation describing the vehicles translation

$$\begin{bmatrix} m^t & 0 & 0 \\ 0 & m^t & 0 \\ 0 & 0 & m^t \end{bmatrix} {}^i\vec{a}^G - \left(m^a \begin{bmatrix} 0 & -r_z^{Acm}_{G} & r_y^{Acm}_{G} \\ r_z^{Acm}_{G} & 0 & -r_x^{Acm}_{G} \\ -r_y^{Acm}_{G} & r_x^{Acm}_{G} & 0 \end{bmatrix} + m^e \begin{bmatrix} 0 & l_x^{Ecm}_{G}\beta_y & l_x^{Ecm}_{G}\beta_z \\ -l_x^{Ecm}_{G}\beta_y & 0 & -l_x^{Ecm}_{G} \\ -l_x^{Ecm}_{G}\beta_z & l_x^{Ecm}_{G} & 0 \end{bmatrix} \right) {}^i\vec{\alpha}^b +$$

$$\left(+ \sum_1^n m^{sn} \begin{bmatrix} 0 & -l_z^{Sn}_{G} & l_y^{Sn}_{G} \\ l_z^{Sn}_{G} & 0 & -l_x^{Sn}_{G} \\ -l_y^{Sn}_{G} & l_x^{Sn}_{G} & 0 \end{bmatrix} + \begin{bmatrix} 0 & -d_{Sn_z} & d_{Sn_y} \\ d_{Sn_z} & 0 & 0 \\ -d_{Sn_y} & 0 & 0 \end{bmatrix} \right) \tag{2.22}$$

$$m^e \begin{bmatrix} 0 & -l_x^{Ecm}_{G}\beta_y & -l_x^{Ecm}_{G}\beta_z \\ l_x^{Ecm}_{G}\beta_y & 0 & l_x^{Ecm}_{G} \\ l_x^{Ecm}_{G}\beta_z & -l_x^{Ecm}_{G} & 0 \end{bmatrix} {}^b\vec{\alpha}^e + \sum_1^n \begin{bmatrix} m^{Sn} & 0 & 0 \\ 0 & m^{Sn} & 0 \\ 0 & 0 & m^{Sn} \end{bmatrix} \ddot{\vec{d}}_{sn}.$$

This fully expanded form shows that there are several additional bilinear terms that need to be removed. These terms are created by the time varying components of the cross product matrices such as β and d_{Sn} being multiplied by states such as ${}^i\vec{\alpha}^b$ and ${}^b\vec{\alpha}^e$.

Removing the bilinear terms and combining the left side of the equation with the linear right hand side given in equation (2.14) gives the complete linearized equation of motion for the translation of the vehicle in expanded form

$$\begin{bmatrix} m^t & 0 & 0 \\ 0 & m^t & 0 \\ 0 & 0 & m^t \end{bmatrix} {}^i\vec{a}^G - \left(m^a \begin{bmatrix} 0 & -r_z^{\frac{Acm}{G}} & r_y^{\frac{Acm}{G}} \\ r_z^{\frac{Acm}{G}} & 0 & -r_x^{\frac{Acm}{G}} \\ -r_y^{\frac{Acm}{G}} & r_x^{\frac{Acm}{G}} & 0 \end{bmatrix} + m^e \begin{bmatrix} 0 & 0 & 0 \\ 0 & 0 & -l_x^{\frac{Ecm}{G}} \\ 0 & l_x^{\frac{Ecm}{G}} & 0 \end{bmatrix} \right) {}^i\vec{a}^b + \left(+ \sum_1^n m^{sn} \begin{bmatrix} 0 & -l_z^{\frac{Sn}{G}} & l_y^{\frac{Sn}{G}} \\ l_z^{\frac{Sn}{G}} & 0 & -l_x^{\frac{Sn}{G}} \\ -l_y^{\frac{Sn}{G}} & l_x^{\frac{Sn}{G}} & 0 \end{bmatrix} \right)$$

$$m^e \begin{bmatrix} 0 & 0 & 0 \\ 0 & 0 & l_x^{\frac{Ecm}{G}} \\ 0 & -l_x^{\frac{Ecm}{G}} & 0 \end{bmatrix} {}^b\vec{a}^e + \sum_1^n \begin{bmatrix} m^{Sn} & 0 & 0 \\ 0 & m^{Sn} & 0 \\ 0 & 0 & m^{Sn} \end{bmatrix} \ddot{\vec{d}}_{sn} = \begin{bmatrix} F \\ F\beta_z \\ -F\beta_y \end{bmatrix} + m^t \begin{bmatrix} -g \\ -g\emptyset_z \\ g\emptyset_y \end{bmatrix}. \tag{2.23}$$

Converting equation (2.23) back to vector form yields

$$\begin{aligned} & m^t {}^i\vec{a}^G - \left(m^a r^{\frac{Acm}{G}\times} + m^e l^{\frac{Ecm}{G}\times} + \sum_1^n m^{sn} l^{\frac{Sn}{G}\times} \right) {}^i\vec{\alpha}^b \\ & + m^e r^{\frac{G}{Ecm}\times} {}^b\vec{\alpha}^e + \sum_1^n m^{Sn} \ddot{\vec{d}}_{sn} = \begin{bmatrix} F \\ F\beta_z \\ -F\beta_y \end{bmatrix} + m^t \begin{bmatrix} -g \\ -g\emptyset_z \\ g\emptyset_y \end{bmatrix}. \end{aligned} \tag{2.24}$$

where all matrices denoted by a $\times$ superscript are the standard cross product matrix except for $\vec{l}^{\frac{Ecm}{G}\times}$ which is equivalent to

$$\vec{l}^{\frac{Ecm}{G}\times} = \begin{bmatrix} 0 & 0 & 0 \\ 0 & 0 & -l_x^{\frac{Ecm}{G}} \\ 0 & l_x^{\frac{Ecm}{G}} & 0 \end{bmatrix}. \tag{2.25}$$

2.2.3.2 Linearization of the Angular Acceleration of the Body Equation

The next equation to be linearized is the equation describing the angular motion of the entire vehicle body about the composite center of mass in the body reference frame. The equation of motion is given by [11] as

$$\begin{aligned}
&\left(\underline{I}^{\overrightarrow{A}}_{\overrightarrow{Acm}} + \underline{I}^{\overrightarrow{E}}_{\overrightarrow{Ecm}} + m^a \vec{r}^{\overrightarrow{Acm}^x}_{\overrightarrow{Ccm}} \vec{r}^{\overrightarrow{G}^x}_{\overrightarrow{Acm}} + m^e \vec{r}^{\overrightarrow{Ecm}^x}_{\overrightarrow{Ccm}} \vec{r}^{\overrightarrow{G}^x}_{\overrightarrow{Ecm}} + \sum_n m^{Sn} \vec{r}^{\overrightarrow{Sn}^x}_{\overrightarrow{Ccm}} \vec{r}^{\overrightarrow{G}^x}_{\overrightarrow{Sn}}\right) {}^i\vec{\alpha}^b \\
&+ \left(\underline{I}^{\overrightarrow{E}}_{\overrightarrow{Ecm}} + m^e \vec{r}^{\overrightarrow{Ecm}^x}_{\overrightarrow{Ccm}} \vec{r}^{\overrightarrow{G}^x}_{\overrightarrow{Ecm}}\right) {}^b\vec{\alpha}^e + \sum_n \left(m^{Sn} \vec{r}^{\overrightarrow{Sn}^x}_{\overrightarrow{Ccm}}\right) \ddot{\vec{d}}_{Sn} \\
&= \vec{M}^{\overrightarrow{sys}}_{\overrightarrow{Ccm}} - {}^i\vec{\omega}^b \times \left(\underline{I}^{\overrightarrow{A}}_{\overrightarrow{Acm}} \cdot {}^i\vec{\omega}^b\right) + \left(\underline{I}^{\overrightarrow{E}}_{\overrightarrow{Ecm}} \cdot {}^i\vec{\omega}^b \times {}^b\vec{\omega}^e\right) - {}^i\vec{\omega}^e \\
&\times \left(\underline{I}^{\overrightarrow{E}}_{\overrightarrow{Ecm}} \cdot {}^i\vec{\omega}^e\right) \\
&- \vec{r}^{\overrightarrow{Ecm}}_{\overrightarrow{Ccm}} \times m^e \left({}^i\vec{\omega}^e \times \left({}^i\vec{\omega}^e \times \vec{r}^{\overrightarrow{Ecm}}_{\overrightarrow{G}}\right)\right) \\
&- \sum_1^n \left[\vec{r}^{\overrightarrow{Sn}}_{\overrightarrow{Ccm}} \times m^{Sn} \left({}^i\vec{\omega}^b \times \left(2\dot{\vec{d}}_{Sn} + {}^i\vec{\omega}^b \times \vec{r}^{\overrightarrow{Sn}}_{\overrightarrow{G}}\right)\right)\right] - \vec{r}^{\overrightarrow{Acm}}_{\overrightarrow{Ccm}} \\
&\times m^a \left({}^i\vec{\omega}^b \times \left({}^i\vec{\omega}^b \times \vec{r}^{\overrightarrow{Acm}}_{\overrightarrow{G}}\right)\right) \\
&- m^e \vec{r}^{\overrightarrow{Ecm}}_{\overrightarrow{Ccm}} \times \left(\left({}^i\vec{\omega}^b \times {}^b\vec{\omega}^e\right) \times \vec{r}^{\overrightarrow{Ecm}}_{\overrightarrow{G}}\right),
\end{aligned} \tag{2.26}$$

where

$$\vec{M}^{\overrightarrow{sys}}_{\overrightarrow{Ccm}} = -\left(\vec{r}^{\overrightarrow{Ccm}}_{\overrightarrow{G}}\right) \times \vec{F}_{thrust}. \tag{2.27}$$

The first step in linearizing this equation is to remove the obvious nonlinear terms. The easiest terms to remove as nonlinear are any higher order terms or bilinear terms where two states are multiplied together. For the purposes of this equation, these terms are largely the $\omega \times \omega$ terms. These nonlinear terms can be seen underlined in the equation

$$\left(\underline{I}^{\underline{A}}_{\underline{Acm}} + \underline{I}^{\underline{E}}_{\underline{Ecm}} + m^a \vec{r}^{Acm\,x}_{Ccm}\,\vec{r}^{\,G\,x}_{Acm} + m^e \vec{r}^{Ecm\,x}_{Ccm}\,\vec{r}^{\,G\,x}_{Ecm} + \sum_n m^{Sn} \vec{r}^{Sn\,x}_{Ccm}\,\vec{r}^{\,G\,x}_{Sn}\right) {}^i\vec{\alpha}^b +$$

$$\left(\underline{I}^{\underline{E}}_{\underline{Ecm}} + m^e \vec{r}^{Ecm\,x}_{Ccm}\,\vec{r}^{\,G\,x}_{Ecm}\right) {}^b\vec{\alpha}^e + \sum_n \left(m^{Sn} \vec{r}^{Sn\,x}_{Ccm}\right) \ddot{\vec{d}}_{Sn} =$$

$$\vec{M}^{sys}_{Ccm} - \underline{{}^i\vec{\omega}^b \times \left(\underline{I}^{\underline{A}}_{\underline{Acm}} \cdot {}^i\vec{\omega}^b\right)} + \left(\underline{I}^{\underline{E}}_{\underline{Ecm}} \cdot \underline{{}^i\vec{\omega}^b \times {}^b\vec{\omega}^e}\right) - \underline{{}^i\vec{\omega}^e} \times \underline{\left(\underline{I}^{\underline{E}}_{\underline{Ecm}} \cdot {}^i\vec{\omega}^e\right)} -$$

$$\vec{r}^{Ecm}_{Ccm} \times m^e \underline{\left({}^i\vec{\omega}^e \times \left({}^i\vec{\omega}^e \times \vec{r}^{\,Ecm}_{G}\right)\right)} - \tag{2.28}$$

$$\sum_1^n \left[\vec{r}^{Sn}_{Ccm} \times m^{Sn} \underline{\left({}^i\vec{\omega}^b \times \left(2\dot{\vec{d}}_{Sn} + {}^i\vec{\omega}^b \times \vec{r}^{\,Sn}_{G}\right)\right)}\right] - \vec{r}^{Acm}_{Ccm} \times$$

$$m^a \underline{\left({}^i\vec{\omega}^b \times \left({}^i\vec{\omega}^b \times \vec{r}^{\,Acm}_{G}\right)\right)} - m^e \vec{r}^{Ecm}_{Ccm} \times \left(\underline{\left({}^i\vec{\omega}^b \times {}^b\vec{\omega}^e\right)} \times \vec{r}^{\,Ecm}_{G}\right).$$

Removing these nonlinear terms gives the simplified equation as

$$\left(\underline{I}^{\underline{A}}_{\underline{Acm}} + \underline{I}^{\underline{E}}_{\underline{Ecm}} + m^a \vec{r}^{Acm\,x}_{Ccm}\,\vec{r}^{\,G\,x}_{Acm} + m^e \vec{r}^{Ecm\,x}_{Ccm}\,\vec{r}^{\,G\,x}_{Ecm} + \sum_n m^{Sn} \vec{r}^{Sn\,x}_{Ccm}\,\vec{r}^{\,G\,x}_{Sn}\right) {}^i\vec{\alpha}^b +$$

$$\left(\underline{I}^{\underline{E}}_{\underline{Ecm}} + m^e \vec{r}^{Ecm\,x}_{Ccm}\,\vec{r}^{\,G\,x}_{Ecm}\right) {}^b\vec{\alpha}^e + \sum_n \left(m^{Sn} \vec{r}^{Sn\,x}_{Ccm}\right) \ddot{\vec{d}}_{Sn} = \vec{M}^{sys}_{Ccm}. \tag{2.29}$$

The forcing term on the rotation of the body is given as a total moment on the system $\vec{M}^{sys}_{Ccm}$. The only external linear moment that remains on the system is the moment created by the thrust of the engine when it is gimbaled. This moment is essentially modeling the rotation of the vehicle as the engine thrust changes direction. In order to accurately model this behavior in the linear form this equation must be expanded before terms are removed. The vector from the gimbal to the composite center of mass can be written by the definition of center of mass as

$$\vec{r}^{\,Ccm}_{G} = \frac{1}{m^t}\left[m^a \vec{r}^{\,Acm}_{G} + m^e \vec{r}^{\,Ecm}_{G} + \sum_n m^{Sn} \vec{r}^{\,Sn}_{G}\right], \tag{2.30}$$

Where,

$$\vec{r}^{\,\frac{Acm}{G}} = \begin{bmatrix} r_x^{\frac{Acm}{G}} \\ r_y^{\frac{Acm}{G}} \\ r_z^{\frac{Acm}{G}} \end{bmatrix}. \tag{2.31}$$

The vector describing the position of the engine center of mass relative to the gimbal point $\vec{r}^{\,\frac{Ecm}{G}}$ is varying with time and dependent on the gimbal angle β. In order to fully describe this vector it must be described in terms of known quantities. Since the vector describing the position of the engine center of mass relative to the gimbal point is constant in the engine frame, this constant vector can be rotated into the body frame by using a linearized ZY rotation matrix. Assuming the gimbal angles are significantly small enough to use the small angle approximation, the vector from the gimbal to the engine center of mass in the body frame becomes

$$\vec{r}^{\,\frac{Ecm}{G}} = \begin{bmatrix} 1 & -\beta_z & \beta_y \\ \beta_z & 1 & 0 \\ -\beta_y & 0 & 1 \end{bmatrix} \begin{bmatrix} l_x^{\frac{Ecm}{G}} \\ 0 \\ 0 \end{bmatrix} = \begin{bmatrix} l_x^{\frac{Ecm}{G}} \\ l_x^{\frac{Ecm}{G}} \beta_z \\ -l_x^{\frac{Ecm}{G}} \beta_y \end{bmatrix}. \tag{2.32}$$

The vector describing the position of the individual sloshing propellant masses relative to the gimbal point is also varying with time. This vector can be expanded and written as the combination of the fixed vector from the gimbal point to the un-displaced slosh mass and the displacement, d_{Sn} of the slosh mass from its un-displaced location,

$$\Sigma_n \vec{r}^{\,\frac{Sn}{G}} = \Sigma_n \begin{bmatrix} l_x^{\frac{Sn}{G}} \\ l_y^{\frac{Sn}{G}} \\ l_z^{\frac{Sn}{G}} \end{bmatrix} + \begin{bmatrix} 0 \\ d_{Sn_y} \\ d_{Sn_z} \end{bmatrix}. \tag{2.33}$$

Since all the vectors found in the external forcing moment have now been described, the next step is to accurately describe the thrust of the vehicle in the body frame. Since the thrust of the vehicle is assumed to be directly along the centerline of the engine and the engine center of mass is assumed on the centerline as well then the direction of the thrust

is constant with respect to the engine frame. Therefore, since the thrust is assumed to act through the gimbal the thrust on the vehicle can be written as a ZY rotation from the engine frame to the body frame. Assuming the gimbal angles are significantly small so that the small angle approximation is valid, the thrust in the body frame can be written as a function of gimbal angle as

$$ {}^{b}\vec{F}_{thrust} = \begin{bmatrix} 1 & -\beta_z & \beta_y \\ \beta_z & 1 & 0 \\ -\beta_y & 0 & 1 \end{bmatrix} \begin{bmatrix} F \\ 0 \\ 0 \end{bmatrix} = \begin{bmatrix} F \\ F\beta_z \\ -F\beta_y \end{bmatrix}. \tag{2.34} $$

It is now possible to substitute these expanded terms into the external moment equation. Expanding the original form of the moment equation in equation (2.27) gives

$$ \vec{M}^{\frac{sys}{Ccm}} = -\frac{1}{m^t}\left[m^a\vec{r}^{\frac{Acm}{G}} + m^e\vec{r}^{\frac{Ecm}{G}} + \sum_n m^{Sn}\vec{r}^{\frac{Sn}{G}}\right] \times {}^{b}\vec{F}_{thrust}. \tag{2.35} $$

Distributing the cross product of the terms with the force of thrust in the body frame ${}^{b}\vec{F}_{thrust}$ gives

$$ \begin{aligned} \vec{M}^{\frac{sys}{Ccm}} = -\frac{1}{m^t}\Bigg[& m^a\vec{r}^{\frac{Acm}{G}} \times {}^{b}\vec{F}_{thrust} + m^e\vec{r}^{\frac{Ecm}{G}} \times {}^{b}\vec{F}_{thrust} \\ & + \sum_n m^{Sn}\vec{r}^{\frac{Sn}{G}} \times {}^{b}\vec{F}_{thrust}\Bigg]. \end{aligned} \tag{2.36} $$

In order to properly linearize this equation the terms must now be fully expanded. In order to avoid complexity these terms will be expanded individually. The cross product of the vector describing the airframe center of mass location relative to the gimbal with the vehicle thrust in the body frame can be written as

$$ \begin{aligned} \vec{r}^{\frac{Acm}{G}} \times {}^{b}\vec{F}_{thrust} = & \begin{bmatrix} 0 & -r_z^{\frac{Acm}{G}} & r_y^{\frac{Acm}{G}} \\ r_z^{\frac{Acm}{G}} & 0 & -r_x^{\frac{Acm}{G}} \\ -r_y^{\frac{Acm}{G}} & r_x^{\frac{Acm}{G}} & 0 \end{bmatrix} \begin{bmatrix} F \\ F\beta_z \\ -F\beta_y \end{bmatrix} = \\ & \begin{bmatrix} -r_z^{\frac{Acm}{G}}F\beta_z - r_y^{\frac{Acm}{G}}F\beta_y \\ r_z^{\frac{Acm}{G}}F + r_x^{\frac{Acm}{G}}F\beta_y \\ -r_y^{\frac{Acm}{G}}F + r_x^{\frac{Acm}{G}}F\beta_z \end{bmatrix}. \end{aligned} \tag{2.37} $$

Since the airframe center of mass location is assumed constant relative to the gimbal there are no terms that directly cancel due to nonlinearity. The next term to be examined is the engine term. The cross product of the vector describing the engine center of mass location relative to the gimbal with the vehicle thrust in the body frame can be written as

$$\vec{r}^{\,\frac{Ecm}{G}} \times {}^{b}\vec{F}_{thrust} = \begin{bmatrix} 0 & l_x^{\frac{Ecm}{G}}\beta_y & l_x^{\frac{Ecm}{G}}\beta_z \\ -l_x^{\frac{Ecm}{G}}\beta_y & 0 & -l_x^{\frac{Ecm}{G}} \\ -l_x^{\frac{Ecm}{G}}\beta_z & l_x^{\frac{Ecm}{G}} & 0 \end{bmatrix} \begin{bmatrix} F \\ F\beta_z \\ -F\beta_y \end{bmatrix} = \begin{bmatrix} l_x^{\frac{Ecm}{G}}F\beta_z\beta_y - l_x^{\frac{Ecm}{G}}F\beta_z\beta_y \\ -l_x^{\frac{Ecm}{G}}F\beta_y + l_x^{\frac{Ecm}{G}}F\beta_y \\ -l_x^{\frac{Ecm}{G}}F\beta_z + l_x^{\frac{Ecm}{G}}F\beta_z \end{bmatrix}. \tag{2.38}$$

It can be seen from inspection that this term becomes the zero vector, therefore

$$\vec{r}^{\,\frac{Ecm}{G}} \times {}^{b}\vec{F}_{thrust} = \begin{bmatrix} l_x^{\frac{Ecm}{G}}F\beta_z\beta_y - l_x^{\frac{Ecm}{G}}F\beta_z\beta_y \\ -l_x^{\frac{Ecm}{G}}F\beta_y + l_x^{\frac{Ecm}{G}}F\beta_y \\ -l_x^{\frac{Ecm}{G}}F\beta_z + l_x^{\frac{Ecm}{G}}F\beta_z \end{bmatrix} = \begin{bmatrix} 0 \\ 0 \\ 0 \end{bmatrix}. \tag{2.39}$$

The engine term can therefore be cancelled from equation (2.36). The last terms to examine are the slosh mass terms. The cross product of the vector describing an individual propellant center of mass location relative to the gimbal with the vehicle thrust in the body frame can be written as

$$
\begin{aligned}
&\vec{r}^{\frac{Sn}{G}} \times {}^{b}\vec{F}_{thrust} \\
&= \begin{bmatrix} 0 & -l_z\frac{Sn}{G} & l_y\frac{Sn}{G} \\ l_z\frac{Sn}{G} & 0 & -l_x\frac{Sn}{G} \\ -l_y\frac{Sn}{G} & l_x\frac{Sn}{G} & 0 \end{bmatrix}\begin{bmatrix} F \\ F\beta_z \\ -F\beta_y \end{bmatrix} \\
&+ \begin{bmatrix} 0 & -d_{Sn_z} & d_{Sn_y} \\ d_{Sn_z} & 0 & 0 \\ -d_{Sn_y} & 0 & 0 \end{bmatrix}\begin{bmatrix} F \\ F\beta_z \\ -F\beta_y \end{bmatrix} \\
&= \begin{bmatrix} -l_z\frac{Sn}{G}F\beta_z - l_y\frac{Sn}{G}F\beta_y \\ l_z\frac{Sn}{G}F + l_x\frac{Sn}{G}F\beta_y \\ -l_y\frac{Sn}{G}F + l_x\frac{Sn}{G}F\beta_z \end{bmatrix} + \begin{bmatrix} -d_{Sn_z}F\beta_z - d_{Sn_y}F\beta_y \\ d_{Sn_z}F \\ -d_{Sn_y}F \end{bmatrix}.
\end{aligned}
\tag{2.40}
$$

Since the engine term was shown to cancel in equation (2.39), the external moment on the system can now be written in fully expanded form as

$$
\begin{aligned}
\vec{M}^{\frac{sys}{Ccm}} = -\frac{1}{m^t}\Bigg[& m^a\begin{bmatrix} -r_z\frac{Acm}{G}F\beta_z - r_y\frac{Acm}{G}F\beta_y \\ r_z\frac{Acm}{G}F + r_x\frac{Acm}{G}F\beta_y \\ -r_y\frac{Acm}{G}F + r_x\frac{Acm}{G}F\beta_z \end{bmatrix} \\
& + \sum_n m^{Sn}\begin{bmatrix} -l_z\frac{Sn}{G}F\beta_z - l_y\frac{Sn}{G}F\beta_y \\ l_z\frac{Sn}{G}F + l_x\frac{Sn}{G}F\beta_y \\ -l_y\frac{Sn}{G}F + l_x\frac{Sn}{G}F\beta_z \end{bmatrix} \\
& + \begin{bmatrix} -d_{Sn_z}F\beta_z - d_{Sn_y}F\beta_y \\ d_{Sn_z}F \\ -d_{Sn_y}F \end{bmatrix}\Bigg].
\end{aligned}
\tag{2.41}
$$

Since there are still some bilinear terms which exist in the slosh term, this equation can be further reduced by eliminating the bilinear terms to the equation

$$\vec{M}^{\frac{sys}{Ccm}} = -\frac{1}{m^t}\left[m^a \begin{bmatrix} -r_z \frac{Acm}{G} F\beta_z - r_y \frac{Acm}{G} F\beta_y \\ r_z \frac{Acm}{G} F + r_x \frac{Acm}{G} F\beta_y \\ -r_y \frac{Acm}{G} F + r_x \frac{Acm}{G} F\beta_z \end{bmatrix} + \sum_n m^{Sn} \begin{bmatrix} -l_z \frac{Sn}{G} F\beta_z - l_y \frac{Sn}{G} F\beta_y \\ l_z \frac{Sn}{G} F + l_x \frac{Sn}{G} F\beta_y \\ -l_y \frac{Sn}{G} F + l_x \frac{Sn}{G} F\beta_z \end{bmatrix} + \begin{bmatrix} 0 \\ d_{Sn_z} F \\ -d_{Sn_y} F \end{bmatrix} \right]. \tag{2.42}$$

Since the magnitude of the force of thrust on the vehicle is assumed to be constant at a specified time, and the equation of motion is being linearized about a particular point constant terms can be ignored in order to create a linear state space model of the system. Removing all constant terms not multiplied by a state reduces the external moment on the system to

$$\vec{M}^{\frac{sys}{Ccm}} = -\frac{1}{m^t}\left[m^a \begin{bmatrix} -r_z \frac{Acm}{G} F\beta_z - r_y \frac{Acm}{G} F\beta_y \\ r_x \frac{Acm}{G} F\beta_y \\ r_x \frac{Acm}{G} F\beta_z \end{bmatrix} + \sum_n m^{Sn} \begin{bmatrix} -l_z \frac{Sn}{G} F\beta_z - l_y \frac{Sn}{G} F\beta_y \\ l_x \frac{Sn}{G} F\beta_y \\ l_x \frac{Sn}{G} F\beta_z \end{bmatrix} + \begin{bmatrix} 0 \\ d_{Sn_z} F \\ -d_{Sn_y} F \end{bmatrix} \right]. \tag{2.43}$$

Since the forcing terms of the equation of motion describing the rotation of the vehicle in the body frame have now been fully linearized the next step is to expand the left hand side of the equation of motion in order to eliminate necessary terms. The left hand side of the equation of motion is written as

$$\left(\underline{\underline{I}}^{\overrightarrow{Acm}}_{A} + \underline{\underline{I}}^{\overrightarrow{Ecm}}_{E} + m^{a}\vec{r}^{\overrightarrow{Acm}\times}_{\overrightarrow{Ccm}}\vec{r}^{\overrightarrow{G}\times}_{\overrightarrow{Acm}} + m^{e}\vec{r}^{\overrightarrow{Ecm}\times}_{\overrightarrow{Ccm}}\vec{r}^{\overrightarrow{G}\times}_{\overrightarrow{Ecm}} + \sum_{n} m^{Sn}\vec{r}^{\overrightarrow{Sn}\times}_{\overrightarrow{Ccm}}\vec{r}^{\overrightarrow{G}\times}_{\overrightarrow{Sn}}\right){}^{i}\vec{\alpha}^{b} + \left(\underline{\underline{I}}^{\overrightarrow{Ecm}}_{E} + m^{e}\vec{r}^{\overrightarrow{Ecm}\times}_{\overrightarrow{Ccm}}\vec{r}^{\overrightarrow{G}\times}_{\overrightarrow{Ecm}}\right){}^{b}\vec{\alpha}^{e} + \sum_{n}\left(m^{Sn}\vec{r}^{\overrightarrow{Sn}\times}_{\overrightarrow{Ccm}}\right)\ddot{\vec{d}}_{Sn}. \tag{2.44}$$

Since this equation describes the rotation of the vehicle about the composite center of mass which is changing and not about the fixed gimbal, the vectors describing the location of the airframe, engine, and individual propellant center of masses are not explicitly known. These vectors need to therefore be rewritten in terms of known vectors. The vectors can be rewritten as the summation of the vector from the composite center of mass to the gimbal and the vector from the gimbal to the respective center of mass,

$$\begin{aligned}\vec{r}^{\overrightarrow{Acm}}_{\overrightarrow{Ccm}} &= -\vec{r}^{\overrightarrow{Ccm}}_{\overrightarrow{G}} + \vec{r}^{\overrightarrow{Acm}}_{\overrightarrow{G}}\\ \vec{r}^{\overrightarrow{Ecm}}_{\overrightarrow{Ccm}} &= -\vec{r}^{\overrightarrow{Ccm}}_{\overrightarrow{G}} + \vec{r}^{\overrightarrow{Ecm}}_{\overrightarrow{G}}\\ \vec{r}^{\overrightarrow{Sn}}_{\overrightarrow{Ccm}} &= -\vec{r}^{\overrightarrow{Ccm}}_{\overrightarrow{G}} + \vec{r}^{\overrightarrow{Sn}}_{\overrightarrow{G}}.\end{aligned} \tag{2.45}$$

The vector from the gimbal to the composite center of mass can be written from known vectors using the definition of a center of mass,

$$\vec{r}^{\overrightarrow{Ccm}}_{\overrightarrow{G}} = \frac{1}{m^{t}}\left[m^{a}\vec{r}^{\overrightarrow{Acm}}_{\overrightarrow{G}} + m^{e}\vec{r}^{\overrightarrow{Ecm}}_{\overrightarrow{G}} + \textstyle\sum_{n} m^{Sn}\vec{r}^{\overrightarrow{Sn}}_{\overrightarrow{G}}\right]. \tag{2.46}$$

Although these relationships now allow the equation to be written entirely in terms of known quantities, these quantities are not all constant and therefore further expansion is necessary. Since the position of the airframe center of mass is assumed constant relative to the gimbal point $\vec{r}^{\overrightarrow{Acm}}_{\overrightarrow{G}}$ is therefore assumed constant. As discussed in equation (2.32) the vector from the gimbal to the engine center of mass $\vec{r}^{\overrightarrow{Ecm}}_{\overrightarrow{G}}$ can be written as the fixed engine length in the engine frame rotated into the body frame by the gimbal angle β. Therefore

$$\vec{r}^{\frac{Ecm}{G}} = \begin{bmatrix} l_x^{\frac{Ecm}{G}} \\ l_x^{\frac{Ecm}{G}}\beta_z \\ -l_x^{\frac{Ecm}{G}}\beta_y \end{bmatrix}. \tag{2.47}$$

Similarly, the vector describing the position of an individual slosh mass relative to the gimbal point is the summation of the fixed vector to its un-displaced location and its displacement from equilibrium

$$\sum_n \vec{r}^{\frac{Sn}{G}} = \sum_n \begin{bmatrix} l_x^{\frac{Sn}{G}} \\ l_y^{\frac{Sn}{G}} \\ l_z^{\frac{Sn}{G}} \end{bmatrix} + \begin{bmatrix} 0 \\ d_{Sn_y} \\ d_{Sn_z} \end{bmatrix}. \tag{2.48}$$

These terms can now be substituted into equation (2.45). The expanded form of the vector from the composite center of mass to the airframe center of mass is then written in known quantities as

$$\vec{r}^{\frac{Acm}{Ccm}} = -\frac{1}{m^t}\left[m^a \begin{bmatrix} r_x^{\frac{Acm}{G}} \\ r_y^{\frac{Acm}{G}} \\ r_z^{\frac{Acm}{G}} \end{bmatrix} + m^e \begin{bmatrix} l_x^{\frac{Ecm}{G}} \\ l_x^{\frac{Ecm}{G}}\beta_z \\ -l_x^{\frac{Ecm}{G}}\beta_y \end{bmatrix} + \sum_n m^{Sn} \begin{bmatrix} l_x^{\frac{Sn}{G}} \\ l_y^{\frac{Sn}{G}} \\ l_z^{\frac{Sn}{G}} \end{bmatrix} + \begin{bmatrix} 0 \\ d_{Sn_y} \\ d_{Sn_z} \end{bmatrix} \right] + \begin{bmatrix} r_x^{\frac{Acm}{G}} \\ r^{\frac{Acm}{G}} \\ r^{\frac{Acm}{G}} \end{bmatrix}. \tag{2.49}$$

The expanded form of the vector from the composite center of mass to the engine center of mass is then written in known quantities as

$$\vec{r}^{\frac{Ecm}{Ccm}} = -\frac{1}{m^t}\left[m^a \begin{bmatrix} r_x^{\frac{Acm}{G}} \\ r_y^{\frac{Acm}{G}} \\ r_z^{\frac{Acm}{G}} \end{bmatrix} + m^e \begin{bmatrix} l_x^{\frac{Ecm}{G}} \\ l_x^{\frac{Ecm}{G}}\beta_z \\ -l_x^{\frac{Ecm}{G}}\beta_y \end{bmatrix} + \sum_n m^{Sn} \begin{bmatrix} l_x^{\frac{Sn}{G}} \\ l_y^{\frac{Sn}{G}} \\ l_z^{\frac{Sn}{G}} \end{bmatrix} + \begin{bmatrix} 0 \\ d_{Sn_y} \\ d_{Sn_z} \end{bmatrix} \right] + \begin{bmatrix} l_x^{\frac{Ecm}{G}} \\ l_x^{\frac{Ecm}{G}}\beta_z \\ -l_x^{\frac{Ecm}{G}}\beta_y \end{bmatrix}. \tag{2.50}$$

The expanded form of the vector from the composite center of mass to an individual sloshing propellant center of mass is then written in known quantities as

$$\vec{r}^{\,\frac{Sn}{Ccm}} = -\frac{1}{m^t}\left[m^a\begin{bmatrix} r_x^{\frac{Acm}{G}} \\ r_y^{\frac{Acm}{G}} \\ r_z^{\frac{Acm}{G}} \end{bmatrix} + m^e\begin{bmatrix} l_x^{\frac{Ecm}{G}} \\ l_x^{\frac{Ecm}{G}}\beta_z \\ -l_x^{\frac{Ecm}{G}}\beta_y \end{bmatrix} + \Sigma_n m^{Sn}\begin{bmatrix} l_x^{\frac{Sn}{G}} \\ l_y^{\frac{Sn}{G}} \\ l_z^{\frac{Sn}{G}} \end{bmatrix} + \begin{bmatrix} 0 \\ d_{Sn_y} \\ d_{Sn_z} \end{bmatrix}\right] + \Sigma_n \begin{bmatrix} l_x^{\frac{Sn}{G}} \\ l_y^{\frac{Sn}{G}} \\ l_z^{\frac{Sn}{G}} \end{bmatrix} + \begin{bmatrix} 0 \\ d_{Sn_y} \\ d_{Sn_z} \end{bmatrix}. \tag{2.51}$$

Since all of these vectors are multiplied by states such as ${}^i\vec{\alpha}^b$, any non constant term in the above equations will result in a bilinear term and therefore be cancelled from the equation. In order to avoid complexity these terms can be cancelled now rather than be carried throughout the full expansion of the equation. Cancelling these terms results in the equations

$$\vec{r}^{\,\frac{Acm}{Ccm}} = -\frac{1}{m^t}\left[m^a\begin{bmatrix} r_x^{\frac{Acm}{G}} \\ r_y^{\frac{Acm}{G}} \\ r_z^{\frac{Acm}{G}} \end{bmatrix} + m^e\begin{bmatrix} l_x^{\frac{Ecm}{G}} \\ 0 \\ 0 \end{bmatrix} + \Sigma_n m^{Sn}\begin{bmatrix} l_x^{\frac{Sn}{G}} \\ l_y^{\frac{Sn}{G}} \\ l_z^{\frac{Sn}{G}} \end{bmatrix} + \begin{bmatrix} 0 \\ 0 \\ 0 \end{bmatrix}\right] + \begin{bmatrix} r_x^{\frac{Acm}{G}} \\ r_y^{\frac{Acm}{G}} \\ r_z^{\frac{Acm}{G}} \end{bmatrix}, \tag{2.52}$$

$$\vec{r}^{\,\frac{Ecm}{Ccm}} = -\frac{1}{m^t}\left[m^a\begin{bmatrix} r_x^{\frac{Acm}{G}} \\ r_y^{\frac{Acm}{G}} \\ r_z^{\frac{Acm}{G}} \end{bmatrix} + m^e\begin{bmatrix} l_x^{\frac{Ecm}{G}} \\ 0 \\ 0 \end{bmatrix} + \Sigma_n m^{Sn}\begin{bmatrix} l_x^{\frac{Sn}{G}} \\ l_y^{\frac{Sn}{G}} \\ l_z^{\frac{Sn}{G}} \end{bmatrix} + \begin{bmatrix} 0 \\ 0 \\ 0 \end{bmatrix}\right] + \begin{bmatrix} l_x^{\frac{Ecm}{G}} \\ 0 \\ 0 \end{bmatrix}, \tag{2.53}$$

$$\vec{r}^{\,\frac{Sn}{Ccm}} = -\frac{1}{m^t}\left[m^a\begin{bmatrix} r_x^{\frac{Acm}{G}} \\ r_y^{\frac{Acm}{G}} \\ r_z^{\frac{Acm}{G}} \end{bmatrix} + m^e\begin{bmatrix} l_x^{\frac{Ecm}{G}} \\ 0 \\ 0 \end{bmatrix} + \sum_n m^{Sn}\begin{bmatrix} l_x^{\frac{Sn}{G}} \\ l_y^{\frac{Sn}{G}} \\ l_z^{\frac{Sn}{G}} \end{bmatrix} + \begin{bmatrix} 0 \\ 0 \\ 0 \end{bmatrix}\right] + \sum_n \begin{bmatrix} l_x^{\frac{Sn}{G}} \\ l_y^{\frac{Sn}{G}} \\ l_z^{\frac{Sn}{G}} \end{bmatrix} + \begin{bmatrix} 0 \\ 0 \\ 0 \end{bmatrix}. \tag{2.54}$$

The next step is to define the vectors in their appropriate cross product matrix forms to since all bilinear terms have now been cancelled. The respective cross product matrices for the constant vector parameters are found as

$$\vec{r}^{\,\frac{Acm}{G}^{\times}} = \begin{bmatrix} 0 & -r_z^{\frac{Acm}{G}} & r_y^{\frac{Acm}{G}} \\ r_z^{\frac{Acm}{G}} & 0 & -r_x^{\frac{Acm}{G}} \\ -r_y^{\frac{Acm}{G}} & r_x^{\frac{Acm}{G}} & 0 \end{bmatrix}, \tag{2.55}$$

$$\vec{r}^{\,\frac{G}{Acm}^{\times}} = \begin{bmatrix} 0 & r_z^{\frac{Acm}{G}} & -r_y^{\frac{Acm}{G}} \\ -r_z^{\frac{Acm}{G}} & 0 & r_x^{\frac{Acm}{G}} \\ r_y^{\frac{Acm}{G}} & -r_x^{\frac{Acm}{G}} & 0 \end{bmatrix}, \tag{2.56}$$

$$\vec{l}_x^{\,\frac{Ecm}{G}^{\times}} = \begin{bmatrix} 0 & 0 & 0 \\ 0 & 0 & -l_x^{\frac{Ecm}{G}} \\ 0 & l_x^{\frac{Ecm}{G}} & 0 \end{bmatrix}, \tag{2.57}$$

$$\vec{l}_x^{\,\frac{G}{Ecm}^{\times}} = \begin{bmatrix} 0 & 0 & 0 \\ 0 & 0 & l_x^{\frac{Ecm}{G}} \\ 0 & -l_x^{\frac{Ecm}{G}} & 0 \end{bmatrix}, \tag{2.58}$$

$$\vec{l}^{\,\frac{Sn}{G}\times} = \begin{bmatrix} 0 & -l_z^{\frac{Sn}{G}} & l_y^{\frac{Sn}{G}} \\ l_z^{\frac{Sn}{G}} & 0 & -l_x^{\frac{Sn}{G}} \\ -l_y^{\frac{Sn}{G}} & l_x^{\frac{Sn}{G}} & 0 \end{bmatrix}, \tag{2.59}$$

$$\vec{l}^{\,\frac{G}{Sn}\times} = \begin{bmatrix} 0 & l_z^{\frac{Sn}{G}} & -l_y^{\frac{Sn}{G}} \\ -l_z^{\frac{Sn}{G}} & 0 & l_x^{\frac{Sn}{G}} \\ l_y^{\frac{Sn}{G}} & -l_x^{\frac{Sn}{G}} & 0 \end{bmatrix}. \tag{2.60}$$

The respective cross product matrices for the vectors relative to the composite center of mass are given as

$$\vec{r}^{\,\frac{Acm}{Ccm}\times} = -\frac{1}{m^t}\left[m^a\vec{r}^{\,\frac{Acm}{G}\times} + m^e\vec{l}_x^{\,\frac{Ecm}{G}\times} + \sum_n m^{Sn}\vec{l}^{\,\frac{Sn}{G}\times}\right] + \vec{r}^{\,\frac{Acm}{G}\times}, \tag{2.61}$$

$$\vec{r}^{\,\frac{Ecm}{Ccm}\times} = -\frac{1}{m^t}\left[m^a\vec{r}^{\,\frac{Acm}{G}\times} + m^e\vec{l}_x^{\,\frac{Ecm}{G}\times} + \sum_n m^{Sn}\vec{l}^{\,\frac{Sn}{G}\times}\right] + \vec{l}_x^{\,\frac{Ecm}{G}\times}, \tag{2.62}$$

$$\vec{r}^{\,\frac{Sn}{Ccm}\times} = -\frac{1}{m^t}\left[m^a\vec{r}^{\,\frac{Acm}{G}\times} + m^e\vec{l}_x^{\,\frac{Ecm}{G}\times} + \sum_n m^{Sn}\vec{l}^{\,\frac{Sn}{G}\times}\right] + \sum_n \vec{l}^{\,\frac{Sn}{G}\times}. \tag{2.63}$$

Therefore the left hand side of the equation now becomes.

$$\begin{aligned}\Bigg(\underline{I}^{\frac{A}{Acm}} + \underline{I}^{\frac{E}{Ecm}} + m^a\vec{r}^{\,\frac{Acm}{Ccm}\times}\vec{r}^{\,\frac{G}{Acm}\times} + m^e\vec{r}^{\,\frac{Ecm}{Ccm}\times}\vec{l}_x^{\,\frac{G}{Ecm}\times} \\ + \sum_n m^{Sn}\vec{r}^{\,\frac{Sn}{Ccm}\times}\vec{l}^{\,\frac{G}{Sn}\times}\Bigg)\,{}^i\vec{\alpha}^b \\ + \left(\underline{I}^{\frac{E}{Ecm}} + m^e\vec{r}^{\,\frac{Ecm}{Ccm}\times}\vec{l}_x^{\,\frac{G}{Ecm}\times}\right){}^b\vec{\alpha}^e + \sum_n\left(m^{Sn}\vec{r}^{\,\frac{Sn}{Ccm}\times}\right)\ddot{\vec{d}}_{Sn}.\end{aligned} \tag{2.64}$$

The final equation of motion for the rotation of the vehicle about the composite center of mass in the body frame is then written in simplified form as

$$\left(\underline{\underline{I}}^{\underline{\underline{A}}}_{\overline{Acm}} + \underline{\underline{I}}^{\underline{\underline{E}}}_{\overline{Ecm}} + m^a \vec{r}^{\overline{Acm}^{\times}}_{\overline{Ccm}} \vec{r}^{\overline{G}^{\times}}_{\overline{Acm}} + m^e \vec{r}^{\overline{Ecm}^{\times}}_{\overline{Ccm}} \vec{l}_x^{\overline{G}^{\times}}_{\overline{Ecm}} + \sum_n m^{Sn} \vec{r}^{\overline{Sn}^{\times}}_{\overline{Ccm}} \vec{l}^{\overline{G}^{\times}}_{\overline{Sn}}\right) {}^i\vec{\alpha}^b + \left(\underline{\underline{I}}^{\underline{\underline{E}}}_{\overline{Ecm}} + m^e \vec{r}^{\overline{Ecm}^{\times}}_{\overline{Ccm}} \vec{l}_x^{\overline{G}^{\times}}_{\overline{Ecm}}\right) {}^b\vec{\alpha}^e + \sum_n \left(m^{Sn} \vec{r}^{\overline{Sn}^{\times}}_{\overline{Ccm}}\right) \ddot{\vec{d}}_{Sn}$$
$$= -\frac{1}{M^T}\left[m^a \begin{bmatrix} -r_z \overline{{}^{Acm}_{G}} F\beta_z - r_y \overline{{}^{Acm}_{G}} F\beta_y \\ r_x \overline{{}^{Acm}_{G}} F\beta_y \\ r_x \overline{{}^{Acm}_{G}} F\beta_z \end{bmatrix} + \sum_n m^{Sn} \begin{bmatrix} -l_z \overline{{}^{Sn}_{G}} F\beta_z - l_y \overline{{}^{Sn}_{G}} F\beta_y \\ l_x \overline{{}^{Sn}_{G}} F\beta_y \\ l_x \overline{{}^{Sn}_{G}} F\beta_z \end{bmatrix} + \begin{bmatrix} 0 \\ d_{Sn_z} F \\ -d_{Sn_y} F \end{bmatrix}\right], \tag{2.65}$$

where the respective cross product matrices have been previously defined and

$\underline{\underline{I}}^{\underline{\underline{A}}}_{\overline{Acm}}$ – Inertia of the airframe with respect to the airframe center of mass

$\underline{\underline{I}}^{\underline{\underline{E}}}_{\overline{Ecm}}$ – Inertia of the engine with respect to the engine center of mass.

2.2.3.3 Linearization of Slosh Mass Acceleration Equation of Motion

The complete nonlinear equation of motion describing the displacement of a specified slosh mass relative to its un-displaced equilibrium position is given as [11]

$$m^{Sn} {}^i\vec{a}^G + m^{Sn}\left(\vec{r}^{\overline{G}}_{\overline{Sn}}\right)^{\times} {}^i\vec{\alpha}^b + m^{Sn}\ddot{\vec{d}}_{Sn} = \vec{F}^{Sn} - m^{Sn}\left({}^i\vec{\omega}^b \times \left(2\dot{\vec{d}}_{Sn} + {}^i\vec{\omega}^b \times \vec{r}^{\overline{Sn}}_{\overline{G}}\right)\right), \tag{2.66}$$

where

$$\vec{F}^{Sn} = m^{Sn}\left(-\omega_{Sn}{}^2 \vec{d}_{Sn} - 2\zeta_{Sn}\omega_{Sn}\dot{\vec{d}}_{Sn} + \vec{g}_{body}\right). \tag{2.67}$$

The first step in the linearization is to remove the obvious nonlinear terms. These nonlinear terms are higher order terms and bilinear terms. Removing the higher order $\omega \times \omega$ terms and any obvious bilinear terms leaves the equation

$$m^{S_n}{}^i\vec{a}^G + m^{S_n}\left(\vec{r}^{\overrightarrow{G}}_{\overrightarrow{Sn}}\right)^{\times}\ {}^i\vec{\alpha}^b + m^{S_n}\ddot{\overrightarrow{ds}}_n = \vec{F}^{S_n}. \tag{2.68}$$

The next step is to expand the forcing term $\vec{F}^{sys}$. The translational forces on the system are given by the equation

$$\vec{F}^{S_n} = m^{S_n}\left(-\omega_{Sn}{}^2\overrightarrow{ds}_n - 2\zeta_{Sn}\omega_{Sn}\dot{\overrightarrow{ds}}_n + \vec{g}_{body}\right). \tag{2.69}$$

The acceleration of gravity acting on the vehicle in the body frame is found by rotating the inertial gravity into the body frame. This can be done by making a linear approximation for the rotation of the body relative to the inertial frame. Let the angles describing the angular rotation of the vehicle be

$$\begin{bmatrix} Roll\ Angle \\ Pitch\ Angle \\ Yaw\ Angle \end{bmatrix} = \begin{bmatrix} \emptyset_x \\ \emptyset_y \\ \emptyset_z \end{bmatrix}. \tag{2.70}$$

The next step is to define the gravitational constant, g, and to apply a linearized body zyx rotation. Assuming that the rotation angles of the body are sufficiently small that the small angle approximation is valid, the force of gravity in the body frame is given as

$$\vec{g}_{body} = \begin{bmatrix} 1 & -\emptyset_z & \emptyset_y \\ \emptyset_z & 1 & -\emptyset_x \\ -\emptyset_y & \emptyset_x & 1 \end{bmatrix}\begin{bmatrix} -g \\ 0 \\ 0 \end{bmatrix} = \begin{bmatrix} -g \\ -g\emptyset_z \\ g\emptyset_y \end{bmatrix}. \tag{2.71}$$

Therefore the linearized forces on the individual propellant slosh mass are

$$\vec{F}^{S_n} = m^{S_n}\left(-\omega_{Sn}{}^2\overrightarrow{ds}_n - 2\zeta_{Sn}\omega_{Sn}\dot{\overrightarrow{ds}}_n + \begin{bmatrix} -g \\ -g\emptyset_z \\ g\emptyset_y \end{bmatrix}\right). \tag{2.72}$$

Since the forcing term on the slosh mass has been properly linearized it is now appropriate to analyze the left hand side of the equation describing the motion of an individual sloshing propellant mass given as

$$m^{S_n}{}^i\vec{a}^G + m^{S_n}\left(\vec{r}^{\overrightarrow{G}}_{\overrightarrow{Sn}}\right)^{\times}\ {}^i\vec{\alpha}^b + m^{S_n}\ddot{\overrightarrow{ds}}_n. \tag{2.73}$$

In the linearization of the body translation and body rotation equations it was previously shown the vector from the gimbal to the slosh mass can be written as the summation of the fixed vector to the un-displaced slosh mass and the actual displacement vector of the slosh mass. The same is true for the vector from the slosh mass to the gimbal $\vec{r}^{\frac{G}{Sn}}$ although since the vector has switched directions, so do the signs on both components

$$\sum_n \vec{r}^{\frac{G}{Sn}} = \sum_n \begin{bmatrix} -l_x^{\frac{Sn}{G}} \\ -l_y^{\frac{Sn}{G}} \\ -l_z^{\frac{Sn}{G}} \end{bmatrix} + \begin{bmatrix} 0 \\ -d_{Sn_y} \\ -\vec{d}_{Sn_z} \end{bmatrix}. \tag{2.74}$$

Since this vector is now fully expanded it can be written in the form of a cross product matrix in order to further expand individual terms

$$\vec{r}^{\frac{G}{Sn}\times} = \begin{bmatrix} 0 & l_z^{\frac{Sn}{G}} & -l_y^{\frac{Sn}{G}} \\ -l_z^{\frac{Sn}{G}} & 0 & l_x^{\frac{Sn}{G}} \\ l_y^{\frac{Sn}{G}} & -l_x^{\frac{Sn}{G}} & 0 \end{bmatrix} + \begin{bmatrix} 0 & d_{Sn_z} & -d_{Sn_y} \\ -d_{Sn_z} & 0 & 0 \\ d_{Sn_y} & 0 & 0 \end{bmatrix}. \tag{2.75}$$

Now that all vectors have been properly defined and fully expanded in the appropriate forms they can be substituted into equation (2.73). After this substitution, the left side of the equation of motion for an individual slosh mass is given as

$$\begin{bmatrix} m^{Sn} & 0 & 0 \\ 0 & m^{Sn} & 0 \\ 0 & 0 & m^{Sn} \end{bmatrix} {}^i\vec{a}^G + m^{Sn}\left(\begin{bmatrix} 0 & l_z^{\frac{Sn}{G}} & -l_y^{\frac{Sn}{G}} \\ -l_z^{\frac{Sn}{G}} & 0 & l_x^{\frac{Sn}{G}} \\ l_y^{\frac{Sn}{G}} & -l_x^{\frac{Sn}{G}} & 0 \end{bmatrix} + \begin{bmatrix} 0 & d_{Sn_z} & -d_{Sn_y} \\ -d_{Sn_z} & 0 & 0 \\ d_{Sn_y} & 0 & 0 \end{bmatrix} \right) {}^i\vec{a}^b + \begin{bmatrix} m^{Sn} & 0 & 0 \\ 0 & m^{Sn} & 0 \\ 0 & 0 & m^{Sn} \end{bmatrix} \ddot{\vec{d}}_{Sn}. \tag{2.76}$$

This form shows that there are bilinear terms that exist where the slosh displacement d_{Sn} is multiplied by the rotational state ${}^i\vec{a}^b$. Eliminating these terms and combining this

equation with the linearized forcing terms in equation (2.72) gives the final linearized equation of motion for the displacement of a sloshing propellant mass in expanded form,

$$\begin{aligned}
&\begin{bmatrix} m^{Sn} & 0 & 0 \\ 0 & m^{Sn} & 0 \\ 0 & 0 & m^{Sn} \end{bmatrix} {}^{i}\vec{a}^{G} + m^{S_n} \begin{bmatrix} 0 & l_z^{\frac{Sn}{G}} & -l_y^{\frac{Sn}{G}} \\ -l_z^{\frac{Sn}{G}} & 0 & l_x^{\frac{Sn}{G}} \\ l_y^{\frac{Sn}{G}} & -l_x^{\frac{Sn}{G}} & 0 \end{bmatrix} {}^{i}\vec{\alpha}^{b} \\
&\quad + \begin{bmatrix} m^{Sn} & 0 & 0 \\ 0 & m^{Sn} & 0 \\ 0 & 0 & m^{Sn} \end{bmatrix} \ddot{\vec{ds}}_n \\
&\quad = m^{S_n} \left(\begin{bmatrix} -\omega_{Sn}{}^2 & 0 & 0 \\ 0 & -\omega_{Sn}{}^2 & 0 \\ 0 & 0 & -\omega_{Sn}{}^2 \end{bmatrix} \vec{ds}_n \right. \\
&\quad \left. + \begin{bmatrix} -2\zeta_{Sn}\omega_{Sn} & 0 & 0 \\ 0 & -2\zeta_{Sn}\omega_{Sn} & 0 \\ 0 & 0 & -2\zeta_{Sn}\omega_{Sn} \end{bmatrix} \dot{\vec{ds}}_n + \begin{bmatrix} -g \\ -g\emptyset_z \\ g\emptyset_y \end{bmatrix} \right).
\end{aligned} \tag{2.77}$$

In a simplified vector form the linearized equation of motion for the displacement of a sloshing propellant mass is written as

$$\begin{aligned}
&m^{S_n} {}^{i}\vec{a}^{G} + m^{S_n} \vec{l}_{Sn}^{\,G\times} {}^{i}\vec{\alpha}^{b} + m^{S_n} \ddot{\vec{ds}}_n \\
&\quad = m^{S_n} \left(-\omega_{Sn}{}^2 \vec{ds}_n - 2\zeta_{Sn}\omega_{Sn} \dot{\vec{ds}}_n + \begin{bmatrix} -g \\ -g\emptyset_z \\ g\emptyset_y \end{bmatrix} \right).
\end{aligned} \tag{2.78}$$

Where all matrices denoted by an × superscript are the standard cross product matrix. Since all of the equations of motion have been properly linearized the next step is to convert these equations into accurate linear models.

2.2.3.4 Prescribed Engine Motion Linear Dynamics

In simulation it is often advantageous to prescribe the motion of the engine directly from the controller gimbal command rather than determine it from an equation of motion. This is accurate since the actuation of the engine is in actuality determined by the controller. Transfer functions can then be added to simulate the dynamics of the engine as necessary. However, since the engine has mass and inertia and is still connected to the

vehicle body, engine motion still has effects on the vehicle motion. These effects can be modeled by adding forcing terms into the equations of motion described above. For the equation describing the translational acceleration of the body, the forcing term of the engine on the translational equation of motion is given as [11]

$$\tilde{f}_{engine} = -m^e \vec{r}^{\,G}_{Ecm} \times {}^b\vec{\alpha}^e = -m^e \vec{r}^{\,G\,\times}_{Ecm}\, {}^b\vec{\alpha}^e. \tag{2.79}$$

It has been previously shown in this thesis that

$$\vec{r}^{\,G\,\times}_{Ecm} = \begin{bmatrix} 0 & -l_x^{\frac{Ecm}{G}}\beta_y & -l_x^{\frac{Ecm}{G}}\beta_z \\ l_x^{\frac{Ecm}{G}}\beta_y & 0 & l_x^{\frac{Ecm}{G}} \\ l_x^{\frac{Ecm}{G}}\beta_z & -l_x^{\frac{Ecm}{G}} & 0 \end{bmatrix}. \tag{2.80}$$

Substituting this into equation (2.79) yields

$$\tilde{f}_{engine} = -m^e \begin{bmatrix} 0 & -l_x^{\frac{Ecm}{G}}\beta_y & -l_x^{\frac{Ecm}{G}}\beta_z \\ l_x^{\frac{Ecm}{G}}\beta_y & 0 & l_x^{\frac{Ecm}{G}} \\ l_x^{\frac{Ecm}{G}}\beta_z & -l_x^{\frac{Ecm}{G}} & 0 \end{bmatrix} {}^b\vec{\alpha}^e. \tag{2.81}$$

Removing bilinear terms gives the linear forcing term created by the gimbal motion on the vehicle's translation

$$\tilde{f}_{engine} = -m^e \begin{bmatrix} 0 & 0 & 0 \\ 0 & 0 & l_x^{\frac{Ecm}{G}} \\ 0 & -l_x^{\frac{Ecm}{G}} & 0 \end{bmatrix} {}^b\vec{\alpha}^e. \tag{2.82}$$

For the equation describing the rotational acceleration of the body about the composite center of mass the forcing term is given as [11]

$$\widetilde{m}_{engine} = -\underline{I}^{\frac{E}{Ccm}b}\vec{\alpha}^{e}. \tag{2.83}$$

This relationship is already linear and therefore no further reduction is necessary. For the equation describing the motion of a single slosh mass there is no additional term for engine motion. This is because engine motion is decoupled from slosh in the sense that swiveling the engine has a negligible effect on the lateral motion of the propellant. These terms can be added to the linear equations of motion previously derived if prescribed engine motion is being modeled.

2.2.4 Linearized State Space Model of Gimbaled Lander

The linearized equations of motion are converted to a state space model in order to design and analyze the system response. Allowing x to be a vector containing the states of the system, $\dot{x}$ to be the time derivative of the state vector x, and u to be a vector describing the control inputs on the system, the state space model of the system can be represented in the form [15][16]

$$\begin{aligned} E\dot{x} &= Ax + Bu \\ y &= Cx + Du, \end{aligned} \tag{2.84}$$

where:

A- $n\,x\,n$ matrix

B- $n\,x\,m$ matrix

C- $r\,x\,n$ matrix

D- $r\,x\,m$ matrix

E- $n\,x\,n$ matrix.

n- Number of states

m- Number of control inputs

r- Number of outputs

y- Output vector

In state space models it is important that none of the states be zero states. That is to say that no state that is equivalent to zero should be carried in the model. Since the equations of motion were linearized in their full form, some zero states do exist in the actual implementation of the model. An example of one of these zero states is the restriction of slosh masses to only move in the lateral direction. Therefore the first component of a slosh mass is a zero state which cannot be carried through the control analysis. Additionally, since the engine can only gimbal in two directions which restricts control on the roll of the vehicle, the first state of the vehicle rotation (roll) is ignored in order to prevent carrying this zero state. Additionally, for the particular case where the gimbal controller is being analyzed the first component, which corresponds to the vertical component of the translation state, becomes a zero state as well and is therefore neglected. This means that for the gimbal control model all of the states were reduced from having three components to only two and the removed element is always the first component in that state. Removing the states also requires that the matrices in the respective equations of motion be reduced from 3 x 3 matrices to 2 x 2 matrices. It is absolutely critical that all multiplication be performed before cancelling rows and columns to avoid neglecting terms and to obtain an accurate model. An example of how the states can be removed from the equations is shown below for the arbitrary multiplication of two cross product matrices

$$\vec{r}^{\frac{Acm}{G}\times}\,\vec{r}_{Acm}^{\frac{G}{}\times} = \begin{bmatrix} 0 & -r_z^{\frac{Acm}{G}} & r_y^{\frac{Acm}{G}} \\ r_z^{\frac{Acm}{G}} & 0 & -r_x^{\frac{Acm}{G}} \\ -r_y^{\frac{Acm}{G}} & r_x^{\frac{Acm}{G}} & 0 \end{bmatrix}\begin{bmatrix} 0 & r_z^{\frac{Acm}{G}} & -r_y^{\frac{Acm}{G}} \\ -r_z^{\frac{Acm}{G}} & 0 & r_x^{\frac{Acm}{G}} \\ r_y^{\frac{Acm}{G}} & -r_x^{\frac{Acm}{G}} & 0 \end{bmatrix} \tag{2.85}$$

$$= \begin{bmatrix} 0 + r_z^{\frac{Acm}{G}} r_z^{\frac{Acm}{G}} + r_y^{\frac{Acm}{G}} r_y^{\frac{Acm}{G}} & 0 + 0 - r_y^{\frac{Acm}{G}} r_x^{\frac{Acm}{G}} & 0 - r_z^{\frac{Acm}{G}} r_x^{\frac{Acm}{G}} + 0 \\ 0 + 0 - r_x^{\frac{Acm}{G}} r_y^{\frac{Acm}{G}} & r_z^{\frac{Acm}{G}} r_z^{\frac{Acm}{G}} + 0 + r_x^{\frac{Acm}{G}} r_x^{\frac{Acm}{G}} & -r_z^{\frac{Acm}{G}} r_y^{\frac{Acm}{G}} + 0 + 0 \\ 0 - r_x^{\frac{Acm}{G}} r_z^{\frac{Acm}{G}} + 0 & -r_y^{\frac{Acm}{G}} r_z^{\frac{Acm}{G}} + 0 + 0 & r_y^{\frac{Acm}{G}} r_y^{\frac{Acm}{G}} + r_x^{\frac{Acm}{G}} r_x^{\frac{Acm}{G}} + 0 \end{bmatrix}.$$

Since the multiplication is complete it is only now appropriate to cancel the 1st row and column of the matrix yielding

$$\begin{bmatrix} 0 + r_z^{\frac{Acm}{G}} r_z^{\frac{Acm}{G}} + r_y^{\frac{Acm}{G}} r_y^{\frac{Acm}{G}} & 0 + 0 - r_y^{\frac{Acm}{G}} r_x^{\frac{Acm}{G}} & 0 - r_z^{\frac{Acm}{G}} r_x^{\frac{Acm}{G}} + 0 \\ 0 + 0 - r_x^{\frac{Acm}{G}} r_y^{\frac{Acm}{G}} & r_z^{\frac{Acm}{G}} r_z^{\frac{Acm}{G}} + 0 + r_x^{\frac{Acm}{G}} r_x^{\frac{Acm}{G}} & -r_z^{\frac{Acm}{G}} r_y^{\frac{Acm}{G}} + 0 + 0 \\ 0 - r_x^{\frac{Acm}{G}} r_z^{\frac{Acm}{G}} + 0 & -r_y^{\frac{Acm}{G}} r_z^{\frac{Acm}{G}} + 0 + 0 & r_y^{\frac{Acm}{G}} r_y^{\frac{Acm}{G}} + r_x^{\frac{Acm}{G}} r_x^{\frac{Acm}{G}} + 0 \end{bmatrix} \rightarrow \tag{2.86}$$

$$\begin{bmatrix} r_z^{\frac{Acm}{G}} r_z^{\frac{Acm}{G}} + 0 + r_x^{\frac{Acm}{G}} r_x^{\frac{Acm}{G}} & -r_z^{\frac{Acm}{G}} r_y^{\frac{Acm}{G}} + 0 + 0 \\ -r_y^{\frac{Acm}{G}} r_z^{\frac{Acm}{G}} + 0 + 0 & r_y^{\frac{Acm}{G}} r_y^{\frac{Acm}{G}} + r_x^{\frac{Acm}{G}} r_x^{\frac{Acm}{G}} + 0 \end{bmatrix}.$$

This process is repeated for all multiplied matrices until they are reduced to 2 x 2 forms.

Applying this concept to the gimbal control, the state space model becomes

$$\begin{bmatrix} \underline{I}_{12x12} & \underline{0}_{12x12} \\ \underline{0}_{12x12} & \underline{M} \end{bmatrix}\begin{bmatrix} \dot{z}_1 \\ z_2 \end{bmatrix} = \begin{bmatrix} \underline{0}_{12x12} & \underline{I}_{12x12} \\ \underline{F}_{x1} & \underline{F}_{X2} \end{bmatrix}\begin{bmatrix} z_1 \\ z_2 \end{bmatrix} + \underline{B}\begin{bmatrix} \beta_y & \beta_z & \ddot{\beta}_y & \ddot{\beta}_z \end{bmatrix}. \tag{2.87}$$

Where the states z_1 and z_2 are defined as

$$z_1 = \begin{bmatrix} \mathrm{p} \\ \theta \\ \vec{d}_{s1} \\ \vec{d}_{s2} \\ \vec{d}_{s3} \\ \vec{d}_{s4} \end{bmatrix} \qquad z_2 = \begin{bmatrix} \dot{\mathrm{p}} \\ \dot{\theta} \\ \dot{\vec{d}}_{s1} \\ \dot{\vec{d}}_{s2} \\ \dot{\vec{d}}_{s3} \\ \dot{\vec{d}}_{s4} \end{bmatrix} \tag{2.88}$$

$$\mathrm{p} = \begin{bmatrix} Translation\ in\ the\ y\ direction \\ Translation\ in\ the\ z\ direction \end{bmatrix} \qquad \dot{\mathrm{p}} = \begin{bmatrix} Velocity\ in\ the\ y\ direction \\ Velocity\ in\ the\ z\ direction \end{bmatrix}$$

$$\theta = \begin{bmatrix} Rotation\ about\ the\ y\ axis \\ Rotation\ about\ the\ z\ axis \end{bmatrix} \qquad \dot{\theta} = \begin{bmatrix} Angular\ velocity\ about\ the\ y\ axis \\ Angular\ velocity\ about\ the\ z\ axis \end{bmatrix}$$

$$\vec{d}_{s1} = \begin{bmatrix} Slosh\ mass\ 1\ y\ displacement \\ Slosh\ mass\ 1\ z\ displacement \end{bmatrix} \qquad \dot{\vec{d}}_{s1} = \begin{bmatrix} Slosh\ mass\ 1\ y\ velocity \\ Slosh\ mass\ 1\ z\ velocity \end{bmatrix}$$

$$\vec{d}_{s2} = \begin{bmatrix} Slosh\ mass\ 2\ y\ displacement \\ Slosh\ mass\ 2\ z\ displacement \end{bmatrix} \quad \dot{\vec{d}}_{s2} = \begin{bmatrix} Slosh\ mass\ 2\ y\ velocity \\ Slosh\ mass\ 2\ z\ velocity \end{bmatrix}$$

$$\vec{d}_{s3} = \begin{bmatrix} Slosh\ mass\ 3\ y\ displacement \\ Slosh\ mass\ 3\ z\ displacement \end{bmatrix} \quad \dot{\vec{d}}_{s3} = \begin{bmatrix} Slosh\ mass\ 3\ y\ velocity \\ Slosh\ mass\ 3\ z\ velocity \end{bmatrix}$$

$$\vec{d}_{s4} = \begin{bmatrix} Slosh\ mass\ 4\ y\ displacement \\ Slosh\ mass\ 4\ z\ displacement \end{bmatrix} \quad \dot{\vec{d}}_{s4} = \begin{bmatrix} Slosh\ mass\ 4\ y\ velocity \\ Slosh\ mass\ 4\ z\ velocity \end{bmatrix}.$$

The mass matrix $\underline{M}$ is defined as

$$\underline{M} = \begin{bmatrix} m^t \underline{I}_{2x2} & -\underline{S}_G^t & m^{S_1}\underline{I}_{2x2} & \cdots & m^{S_n}\underline{I}_{2x2} \\ \underline{0}_{2x2} & \underline{I}^{\frac{t}{Ccm}} & m^{S_1}\left(\vec{r}^{\frac{Ccm}{S1}}\right)^x & \cdots & m^{S_n}\left(\vec{r}^{\frac{Ccm}{Sn}}\right)^x \\ m^{S_1}\underline{I}_{2x2} & m^{S_1}\left(\vec{r}^{\frac{G}{S1}}\right)^x & m^{S_1}\underline{I}_{2x2} & \cdots & \underline{0}_{2x2} \\ \vdots & \vdots & \vdots & \ddots & \vdots \\ m^{S_n}\underline{I}_{2x2} & m^{S_n}\left(\vec{r}^{\frac{G}{Sn}}\right)^x & \underline{0}_{2x2} & \cdots & m^{S_n}\underline{I}_{2x2} \end{bmatrix}, \tag{2.89}$$

where:

$$\underline{S}_G^t = \left(m^a r^{\frac{Acm}{G}\times} + m^e l^{\frac{Ecm}{G}\times} + \sum_1^n m^{sn} l^{\frac{Sn}{G}\times} \right) \tag{2.90}$$

and

$$\underline{I}^{\frac{t}{Ccm}} = \left(\underline{I}^{\frac{A}{Acm}} + \underline{I}^{\frac{E}{Ecm}} + m^a \vec{r}^{\frac{Acm}{Ccm}\times} \vec{r}^{\frac{G}{Acm}\times} + m^e \vec{r}^{\frac{Ecm}{Ccm}\times} \vec{l}_x^{\frac{G}{Ecm}\times} + \sum_n m^{Sn} \vec{r}^{\frac{Sn}{Ccm}\times} \vec{l}^{\frac{G}{Sn}\times} \right). \tag{2.91}$$

The forcing matrices $\underline{F}_{x1}$ and $\underline{F}_{x2}$ are defined as

$$\underline{F}_{x1} = \begin{bmatrix} \underline{0}_{2x2} & m^t G_b & \underline{0}_{2x2} & \cdots & \underline{0}_{2x2} \\ \underline{0}_{2x2} & \underline{0}_{2x2} & -\frac{m^{S1}}{m^t} F_b & \cdots & -\frac{m^{Sn}}{m^t} F_b \\ \underline{0}_{2x2} & m^{S_1} G_b & -m^{S_1} \omega_{S1}{}^2 \underline{\mathrm{I}}_{2x2} & \cdots & \underline{0}_{2x2} \\ \vdots & \vdots & \vdots & \ddots & \vdots \\ \underline{0}_{2x2} & m^{S_n} G_b & \underline{0}_{2x2} & \cdots & -m^{S_n} \omega_{Sn}{}^2 \underline{\mathrm{I}}_{2x2} \end{bmatrix}$$

$$\underline{F}_{X2} = \begin{bmatrix} \underline{0}_{2x2} & \underline{0}_{2x2} & \underline{0}_{2x2} & \cdots & \underline{0}_{2x2} \\ \underline{0}_{2x2} & \underline{0}_{2x2} & \underline{0}_{2x2} & \cdots & \underline{0}_{2x2} \\ \underline{0}_{2x2} & \underline{0}_{2x2} & -m^{S_1} 2\zeta_{S1} \omega_{S1} \underline{\mathrm{I}}_{2x2} & \cdots & \underline{0}_{2x2} \\ \vdots & \vdots & \vdots & \ddots & \vdots \\ \underline{0}_{2x2} & \underline{0}_{2x2} & \underline{0}_{2x2} & \cdots & -m^{S_n} 2\zeta_{Sn} \omega_{Sn} \underline{\mathrm{I}}_{2x2} \end{bmatrix} \tag{2.92}$$

and the control matrix $\underline{B}$ is defined as

$$\underline{B} = \begin{bmatrix} F_b & -m^e \vec{l}_x{}^{\times}_{\overline{Ecm}}{}^{G} \\ -\vec{M}^{F_b}_{\overline{Ccm}} & -\underline{I}^{E}_{\overline{Ccm}} \\ \underline{0}_{2x2} & \underline{0}_{2x2} \\ \underline{0}_{2x2} & \underline{0}_{2x2} \\ \underline{0}_{2x2} & \underline{0}_{2x2} \\ \underline{0}_{2x2} & \underline{0}_{2x2} \end{bmatrix}, \tag{2.93}$$

where

$$\vec{M}^{F_b}_{\overline{Ccm}} = \frac{1}{m^t} \left[m^a r_x{}^{Acm}_{\overline{G}} F \underline{\mathrm{I}}_{2x2} + \sum_n m^{Sn} l_x{}^{Sn}_{\overline{G}} F \underline{\mathrm{I}}_{2x2} \right], \tag{2.94}$$

$$\underline{I}^{E}_{\overline{Ccm}} = \left(\underline{I}^{E}_{\overline{Ecm}} + m^e \vec{r}^{Ecm\times}_{\overline{Ccm}} \vec{l}_x{}^{G}_{\overline{Ecm}}{}^{\times} \right), \tag{2.95}$$

and

$$F_b = \begin{bmatrix} 0 & F \\ -F & 0 \end{bmatrix} \quad G_b = \begin{bmatrix} 0 & -g \\ g & 0 \end{bmatrix} \tag{2.96}$$

$\underline{\mathrm{I}}$ - Identity matrix

$\underline{0}$ - Zero matrix.

The output matrix "C" depends upon the control setup. The different control methods will be discussed in Chapter 3 and the coupling "D" matrix in the state space model can be set to a zero matrix.

3 Design of Controller and Vehicle

Using the state space model derived in Chapter 2 it is now possible to develop control designs for the vehicle. The state space model can be used to analyze the stability and response of the vehicle to various control designs as well as the stability of the vehicle as mass properties and vehicle geometry are modified. This chapter will also use the state space model to determine the optimal location of the vehicle propellant tanks to increase stability and performance.

3.1 Steering

Commands prescribed by the guidance block are given in the form of a commanded acceleration vector to follow the desired trajectory. The acceleration vector changes in both magnitude and direction over time. In order to properly reference the commands from the guidance block with the current state of the vehicle, the guidance commands need to first be converted into a desired vehicle state. In traditional control applications, this desired vehicle state describes the desired orientation of the vehicle in terms of the body quaternion and desired body rate. However, in more complex control applications the desired position and velocity of the vehicle may also need to be prescribed. The guidance acceleration commands are converted into the desired vehicle state using a steering block.

The first step in converting the normalized acceleration command into the desired vehicle state is to find the current normalized acceleration command $\vec{\lambda}$ in the inertial reference frame by updating the commanded acceleration from guidance for the current time using the simple linear approximation

$$\vec{\lambda} = \vec{\lambda}_c + (t - t_c)\dot{\vec{\lambda}}_c \tag{3.1}$$

where $\vec{\lambda}_c$ is the normalized acceleration command in the inertial reference frame given at time t_c, $\dot{\vec{\lambda}}_c$ is the rate of change of $\vec{\lambda}_c$, and t is the current time. The next step is to define the axis about which the body must rotate to reach the desired state. This axis will be defined as $\hat{e}_c$ and is given by the equation

$$\hat{e}_c = \vec{r}_i \times \vec{\lambda} \tag{3.2}$$

where $\vec{r}_i$ is the position of the origin of the vehicle's body frame relative to the origin of the inertial reference frame. The angle of rotation $\hat{\theta}_e$ about $\hat{e}_c$ can then be found using the relationship

$$\theta_e = \cos^{-1}(\vec{\lambda} \cdot \vec{r}_i). \tag{3.3}$$

The commanded body quaternion q_c is then given by [17]

$$q_c = \begin{bmatrix} \cos\left(\frac{\theta_e}{2}\right) \\ \sin\left(\frac{\theta_e}{2}\right)\hat{e}_{c1} \\ \sin\left(\frac{\theta_e}{2}\right)\hat{e}_{c2} \\ \sin\left(\frac{\theta_e}{2}\right)\hat{e}_{c3} \end{bmatrix}. \tag{3.4}$$

Applying the small angle approximation the inertial frame can be assumed to be aligned with the body axis and therefore from equation (3.2)

$$\hat{e}_c = \vec{r}_i \times \lambda \approx \begin{bmatrix} 1 \\ 0 \\ 0 \end{bmatrix} \times \begin{bmatrix} \lambda_x \\ \lambda_y \\ \lambda_z \end{bmatrix} \approx \begin{bmatrix} 0 & 0 & 0 \\ 0 & 0 & -1 \\ 0 & 1 & 0 \end{bmatrix} \begin{bmatrix} \lambda_x \\ \lambda_y \\ \lambda_z \end{bmatrix}. \tag{3.5}$$

Since the steering block is only used for gimbal control in the Y and Z directions the linearized steering equation becomes

$$\hat{e}_c \approx S_{linear} \begin{bmatrix} \lambda_y \\ \lambda_z \end{bmatrix} \tag{3.6}$$

where S_{linear} is the linear steering block used for linear stability analysis which translates the given pointing command into the desired rotational angles given as

$$S_{linear} = \begin{bmatrix} 0 & -1 \\ 1 & 0 \end{bmatrix}. \tag{3.7}$$

The commanded body rate ω_c can be found from the cross product of the normalized acceleration vector with its rate of change

$$\omega_c = \vec{\lambda}_c \times \dot{\vec{\lambda}}_c. \tag{3.8}$$

Using these relationships, the guidance commands are now able to be translated into a desired body state which can then be sent to the controller.

3.2 PD Control

There are several control options for the control design of a gimbaled engine vehicle. Proportional-plus-derivative or PD control theory is based on the concept of applying a control directly proportional to the state error and the derivative of the state's error. PD control affords the advantages of improving the transient response of the plant while still offering enough simplicity to appropriately adjust the controller to create the desired response. A diagram of PD control can be seen below in Figure 3-1.

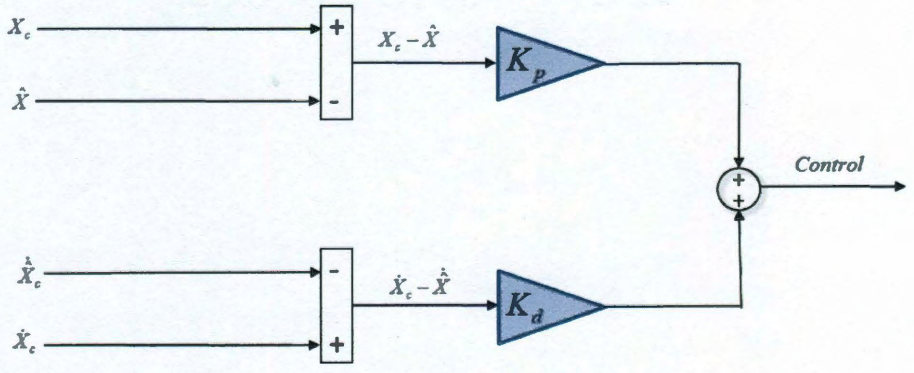

Figure 3-1: Diagram of PD Control

X_c and $\dot{X}_c$ are the commanded state and commanded rate respectively and $\hat{X}$ represents the estimated current state. The error in the state is found by differencing the commanded state X_c and the actual state estimate $\hat{X}$. The state derivative can be found by differentiating the current state estimate is shown in Figure 3-1 or it can be passed directly in to the controller. An example of the latter option would be a plant that calculates both position and velocity passing both position and it's time derivative, velocity, into the controller. The error in the state derivative is calculated by differencing the commanded state derivative and the current state derivative estimate either from differentiating the state estimate or directly from the plant. The state error and state derivative error are then multiplied by their proportional gains K_p and K_d respectively. Both signals are then combined to provide the control signal to the system. The selection of the K_p and K_d gains are critical to the response and stability of the system. The gains must be selected to properly compensate the open-loop system such that the closed-closed loops system satisfies the desired response. There are countless methods used to design gains however the selection of these gains will be discussed in greater detail in later sections.

3.3 Controller Designs

There are several metrics that are very important to any controller design for a gimbaled engine lander. The controller must be fast enough to accurately follow updates in commands and handle perturbations from the environment. The controller also must be robust enough to remain stable throughout any flight trajectory and provide adequate margin to allow for uncertainty. The stability and performance of the vehicle depends

overwhelmingly on the geometry and design of the actual vehicle and the specific design of the controller.

3.3.1 Control Design 1

The first control design is the legacy approach which is similar to the control design that was used during the Apollo program. The guidance block provides position, velocity, and acceleration commands. The position and velocity commands are referenced with the position and velocity estimate of the vehicle. The error in position is scaled by the gain K_r and the error in velocity is scaled by the gain K_v in order to correct for errors in the position and velocity. Typical guidance trajectories are broken into several stages. The guidance correction gains are scaled by the time until the end of a guidance stage t_{go}. Therefore, the gains vary with time. The equation describing the value of the gains is given by the equation [6]

$$K_r = \frac{12}{t_{go}^2} \qquad K_v = \frac{6}{t_{go}} \tag{3.9}$$

where

K_r- Guidance correction position gain

K_v- Guidance correction velocity gain

t_{go}- Time until end of stage.

The gains are kept from becoming unbounded by forcing a minimum value for t_{go}. It is challenging to select the appropriate minimum however since two large of a minimum will result in large positional errors while too low of a minimum t_{go} will result in instability as the gains become too large.

The scaled error is then used to correct the pointing command λ_c which is a unit vector describing the desired acceleration direction. The acceleration command a_c is identical in direction to the pointing command but contains the desired acceleration magnitude as well. The acceleration and pointing commands are then fed into the steering block which converts the pointing command to a quaternion and body rate command. The controller references the commanded body quaternion and body rate from the steering block with the actual body quaternion and body rate of the current state. The thrust is fed forward and is directly specified by the magnitude of the acceleration command from the guidance block.

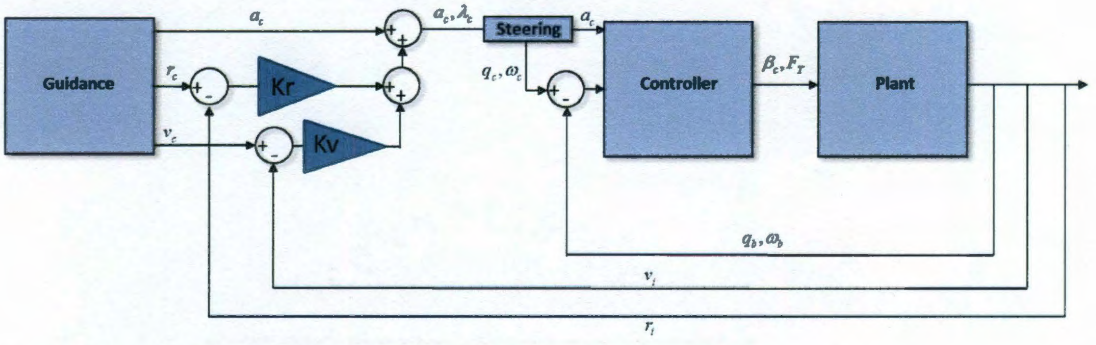

Figure 3-2: Overview of Controller Design 1

In control design 1 the thrust is determined directly from the acceleration command given by the guidance block. This is technique is known as feed-forward thrust control. The magnitude of this command is then calculated and scaled by the current mass estimate of the vehicle to determine the appropriate thrust control. The thrust control of design 1 is shown in Figure 3-3.

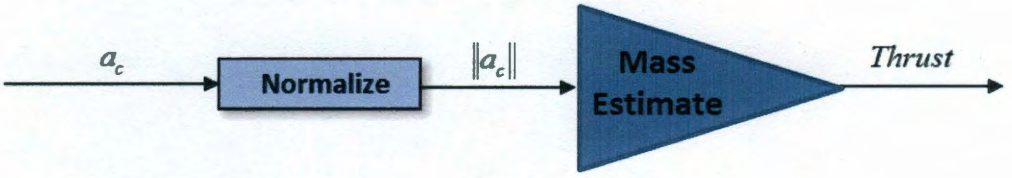

Figure 3-3: Overview of Controller Design 1 Thrust Control

3.3.2 Control Design 2

The second control design is controls the gimbal and throttle based on the inertial state of the vehicle. This differs from the previous design where control was based off a desired attitude to follow a specific guidance command. By controlling the vehicle thrust and gimbal through error in the inertial state the guidance block is separated from direct throttle control. Additionally, the controller is afforded greater robustness in the ability to apply control based directly on the state. The guidance block now provides a desired position and velocity trajectory directly to the controller. This position and velocity is used as a reference command and a control is applied based on the current inertial position and velocity of the vehicle. This is combined with the control based on the body state quaternion and rate errors to determine the appropriate gimbal control. The translational and rotational corrections are weighted equally in the summation. The translational correction is different than that of control design 1 because it is done directly by the controller and not indirectly through a correction to the pointing command. The correction gains on position and velocity error in control design 2 are fixed and can therefore be determined optimally.

As stated previously, the throttle control is now detached from the guidance acceleration command. The thrust of the vehicle is determined through PD control on the error between the altitude of the vehicle and the reference altitude for the prescribed

trajectory. This control design offers several advantages, the greatest of which being the ability to now simply prescribe a position and velocity without the need to prescribe a priori the throttle command needed to fly the desired trajectory. This adds additional robustness to the design in allowing for greater perturbations and delays to the system as well as an additional control to compensate for state error. The architecture of the second design is shown in Figure 3-4.

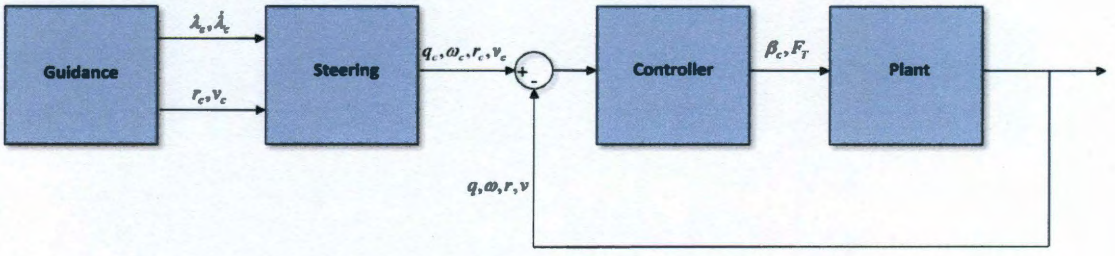

Figure 3-4: Overview of Controller Design 2

The gimbal control can be seen as a parallel combination below in Figure 3-5.

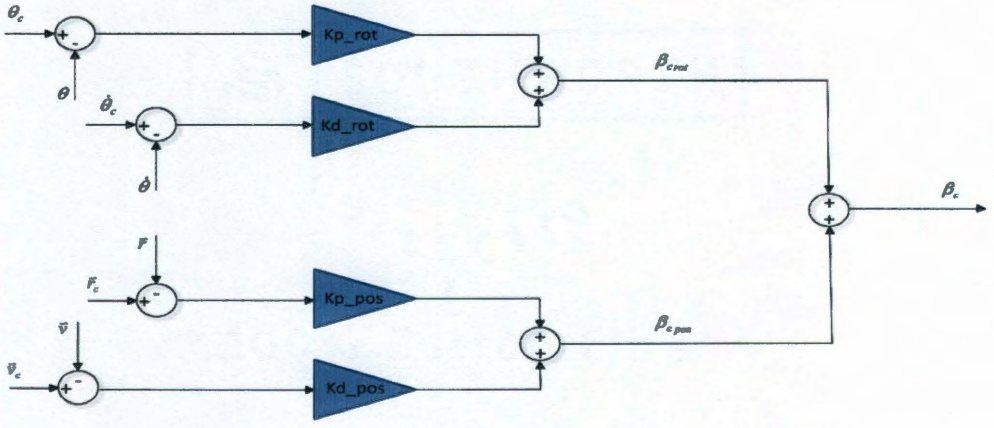

Figure 3-5: Gimbal Control Diagram Using Parallel Rotational and Position Control

In control design 2 the thrust control is determined by using PD control on the error in the vehicle's altitude. This is accomplished by referencing the inertial position and velocity error in the vertical direction and then scaling the error by the appropriate proportional

and derivative gains. The scaled error signal is then biased by adding the magnitude of the acceleration of gravity. The control signal is then scaled by the vehicle mass estimate to give the respective thrust control on the vehicle as shown in Figure 3-6.

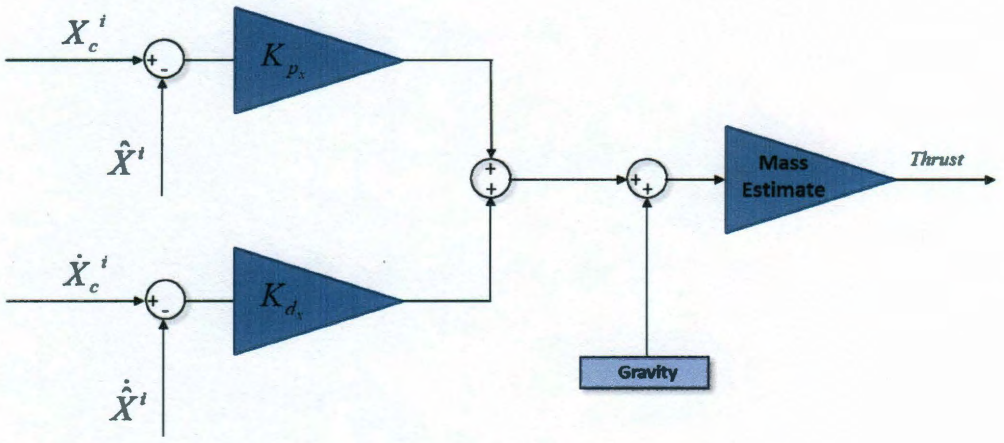

Figure 3-6: Control Design 2 Thrust Control

3.4 Determining State Error

3.4.1 Determining Rotational Error Using Quaternions

Given an arbitrary quaternion q then the conjugate quaternion q^* is given by the relationship [18]

$$q = \begin{bmatrix} q_0 \\ q_1 \\ q_2 \\ q_3 \end{bmatrix} \qquad q^* = \begin{bmatrix} q_0 \\ -q_1 \\ -q_2 \\ -q_3 \end{bmatrix}. \tag{3.10}$$

In order to find the error in the rotational state the quaternion command needs to be multiplied by the conjugate body quaternion. Selecting an arbitrary quaternion command q_c and the conjugate of the body quaternion estimate $\hat{q}_b{}^*$ written respectively as

$$q_c = \begin{bmatrix} q_{c_0} \\ q_{c_1} \\ q_{c_2} \\ q_{c_3} \end{bmatrix} \qquad \hat{q}_b{}^* = \begin{bmatrix} \hat{q}_{b_0} \\ -\hat{q}_{b_1} \\ -\hat{q}_{b_2} \\ -\hat{q}_{b_3} \end{bmatrix}. \tag{3.11}$$

Then the error quaternion q_e is written as [18]

$$\begin{bmatrix} q_{e_0} \\ q_{e_1} \\ q_{e_2} \\ q_{e_3} \end{bmatrix} = \begin{bmatrix} q_{c_0} & -q_{c_1} & -q_{c_2} & -q_{c_3} \\ q_{c_1} & q_{c_0} & -q_{c_3} & q_{c_2} \\ q_{c_2} & q_{c_3} & q_{c_0} & -q_{c_1} \\ q_{c_3} & -q_{c_2} & q_{c_1} & q_{c_0} \end{bmatrix} \begin{bmatrix} \hat{q}_{b_0} \\ -\hat{q}_{b_1} \\ -\hat{q}_{b_2} \\ -\hat{q}_{b_3} \end{bmatrix}. \tag{3.12}$$

The quaternion error can then used to estimate the vehicle's rotational error state which will arbitrarily be referred to as θ_e, through the relationship

$$\theta_e = \begin{bmatrix} \theta_{e_x} \\ \theta_{e_y} \\ \theta_{e_z} \end{bmatrix} \approx \begin{bmatrix} q_{e_1} \\ q_{e_2} \\ q_{e_3} \end{bmatrix}. \tag{3.13}$$

The error in the rotational velocity of the vehicle ω_e can be found using simple subtraction as

$$\omega_e = \begin{bmatrix} \omega_{e_x} \\ \omega_{e_y} \\ \omega_{e_z} \end{bmatrix} = \begin{bmatrix} \omega_{c_x} \\ \omega_{c_y} \\ \omega_{c_z} \end{bmatrix} - \begin{bmatrix} \omega_{b_x} \\ \omega_{b_y} \\ \omega_{b_z} \end{bmatrix}. \tag{3.14}$$

These errors can then be multiplied by the appropriate gains to determine the proportional and derivative controls on the gimbal,

$$\beta_{c_{rot}} = K_{p_{rot}} \begin{bmatrix} \theta_{e_y} \\ \theta_{e_z} \end{bmatrix} + K_{d_{rot}} \begin{bmatrix} \omega_{e_y} \\ \omega_{e_z} \end{bmatrix}. \tag{3.15}$$

3.4.2 Position and Velocity Error

The position error of the vehicle r_e can be found by subtracting the vehicle's actual position estimate from the commanded position given by the guidance block,

$$r_e = \begin{bmatrix} r_{e_x} \\ r_{e_y} \\ r_{e_z} \end{bmatrix} = \begin{bmatrix} r_{c_x} \\ r_{c_y} \\ r_{c_z} \end{bmatrix} - \begin{bmatrix} r_{b_x} \\ r_{b_y} \\ r_{b_z} \end{bmatrix}. \tag{3.16}$$

The velocity error v_e can be found in a similar matter by subtracting the vehicle's actual velocity estimate from the commanded velocity,

$$v_e = \begin{bmatrix} v_{e_x} \\ v_{e_y} \\ v_{e_z} \end{bmatrix} = \begin{bmatrix} v_{c_x} \\ v_{c_y} \\ v_{c_z} \end{bmatrix} - \begin{bmatrix} v_{b_x} \\ v_{b_y} \\ v_{b_z} \end{bmatrix}. \tag{3.17}$$

Because of the rotational properties of the vehicle the commanded gimbal angle for the translational error $\beta_{c_{trans}}$ is not a direct scaling of the state error as it was with the rotational state. This is because gimbaling the engine in a positive direction about the Z axus causes the vehicle to rotate in a negative direction about the Z axis which causes it to translate in the negative Y-direction. Similarly, a positive gimbal rotation about the Y axis causes the vehicle to rotate in a negative direction about the Y axis which in turn causes the vehicle to translate in the positive Z direction. Therefore a positive position or velocity error in the Y direction will result in a negative gimbal angle control about the Z axis and a positive position or velocity error in the Z direction will create a positive gimbal angle control about the Y axis. The gimbal command caused by the translational error of the vehicle $\beta_{c_{trans}}$ is then found using the relationship

$$\beta_{c_{trans}} = K_{p_{trans}} \begin{bmatrix} 0 & 0 & 0 \\ 0 & 0 & -1 \\ 0 & 1 & 0 \end{bmatrix} \begin{bmatrix} r_{e_x} \\ r_{e_y} \\ r_{e_z} \end{bmatrix} + K_{d_{trans}} \begin{bmatrix} 0 & 0 & 0 \\ 0 & 0 & -1 \\ 0 & 1 & 0 \end{bmatrix} \begin{bmatrix} v_{e_x} \\ v_{e_y} \\ v_{e_z} \end{bmatrix}. \tag{3.18}$$

3.5 Stability Analysis

An essential aspect of any controller design is that it is designed to be robustly stable. Not only should the designs be stable under ideal conditions but the designs

should also have adequate margin to be stable under perturbed conditions. This allows for robustness and compensates for errors in assumptions and approximations as well as delays and other perturbations to controlling the vehicle. The three most significant stability margins are gain margin, phase margin, and delay margin. In order to calculate these margins a frequency analysis of the system must be done. A Bode plot is used to show the magnitude of the systems response as well as the phase shift of the system response with respect to frequency.

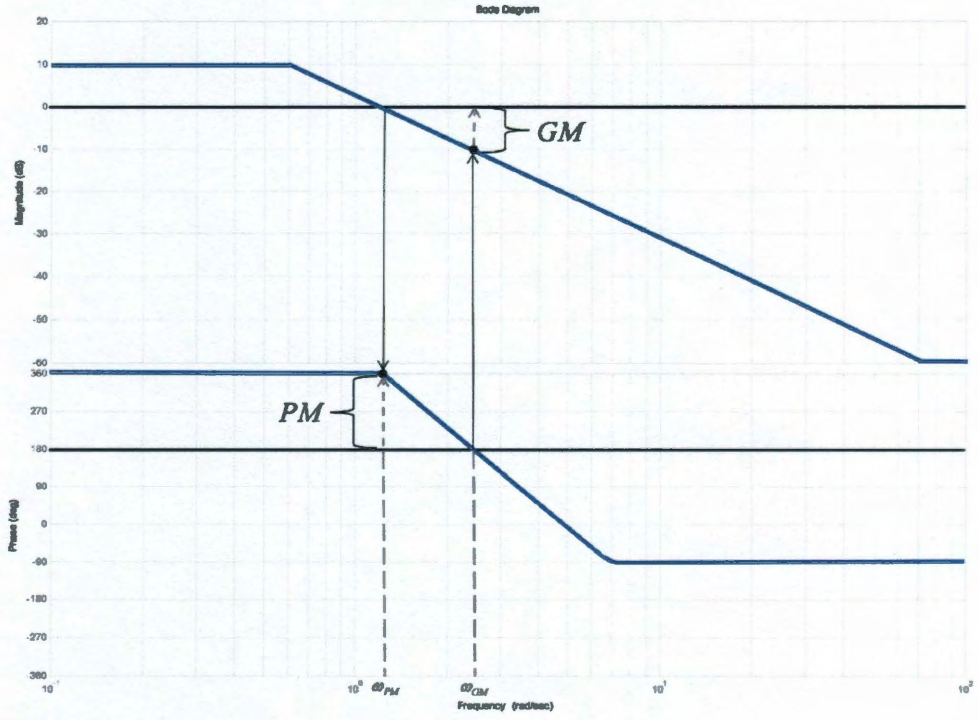

Figure 3-7: Visualization of Gain and Phase Margins on a Bode Diagram

Figure 3-7 shows how the gain and phase margin can be easily calculated from a Bode plot. The gain margin is determined by first finding the frequency ω_{GM} at which the phase angle of the system is 180 degrees. The gain margin is then calculated by finding the gain required to bring the magnitude of the response to 0 dB at ω_{GM}. The gain margin

represents the margin of gain for which the system will still remain stable. In Figure 3-7 the gain margin would be around positive 10 dB since a positive gain of approximately 10 dB is required to bring the magnitude to 0 dB at ω_{GM}. The phase margin can be found in a similar matter. The frequency ω_{PM} at which the magnitude response crosses 0 dB is found first. The phase margin of the system is then found by subtracting 180 degrees from the phase of the system at ω_{PM}. The phase margin represents the amount of phase that the system can be shifted by and the system still remains stable. In Figure 3-7 this value is approximately positive 180 degrees since the phase of the system is approximately 360 degrees at ω_{PM}[19] .The delay margin is directly linked to the phase margin. Therefore the delay margin can be estimated as a percentage of the period based on the phase margin using the relationship

$$DelayMargin = \frac{PhaseMargin}{360°}(Period). \tag{3.19}$$

The delay margin represents the amount of delay that can be applied to the system before instability is reached. These stability parameters can be used to analyze and design a stable controller and be used to select and tune control gains. In a flight control system a desirable Bode plot will have a high gain at low frequencies to allow for accurate control and rapid following of commands. The midrange frequencies should be designed to provide a stable cross-over region which will give the control design good gain and phase margins. The high frequency range of the Bode plot for a flight control system should have very low magnitude which allows the control system to naturally reduce noise and uncertainty in the system [20].

3.6 Optimal Gain Selection

In order to fly the desired trajectory and also remain stable controller gains must be selected that not only provide stability but also meet performance requirements. It is best to design these gains to optimally balance stability and performance. Non-optimal gains could result in inadequate margins and can also result in inefficient control that could waste fuel and endanger the vehicle. There are several methods that can be employed to ensure designed gains are optimal for the vehicle and particular trajectory.

3.6.1 Scripted Optimization Algorithm for Gain Selection

In this thesis an optimization-based approach is used to design control gains to meet the performance and stability specifications. The best way to implement this is through a custom controller design algorithm that can be modified to best suit the given trajectory, vehicle, and application. To do this a script is written to minimize a cost function weighted by several stability and performance criteria. The hierarchal layout of the overall control gain design process can be seen below in Figure 3-8.

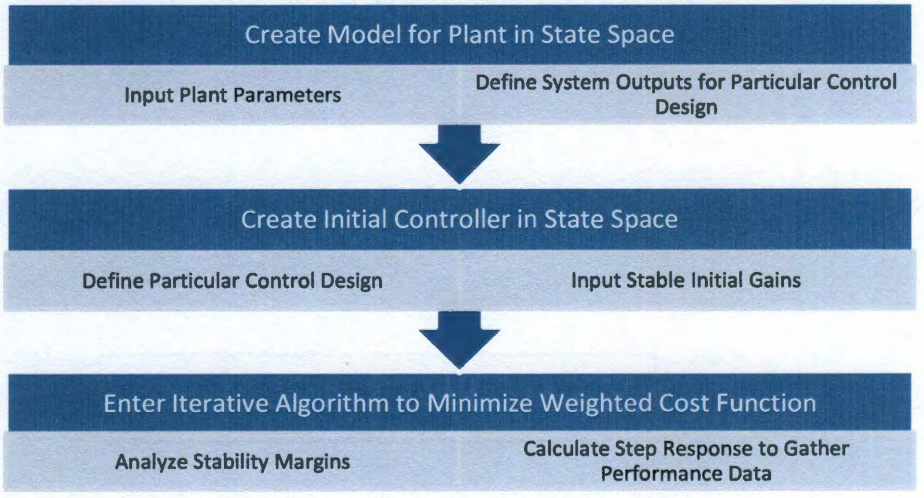

Figure 3-8: Optimal Control Design Process

The first step in script is to set the parameters which correspond to the current mass parameters and trajectory of the vehicle at the point which the gains are to be designed. This includes setting such properties as the propellant tank levels and vehicle mass properties as well as the gimbal angle and throttle setting. These properties can then be converted into the parameters necessary to define the full linear state space model derived in chapter 2. A controller with arbitrary gains is then created using the three designs described previously in this chapter. Although not always possible, the selected arbitrary gains should always to be stable or else further optimization of the gains may not result in convergence. This control design is used as an initial guess and the gains and the plant are sent into a cost function file which is weighted with specific performance and stability criteria. This cost function is then minimized until it reaches an optimal balance between stability and performance.

The variations in the design of the cost function directly create variations in the controller that the script file determines to be optimal. Therefore the proper setup is necessary in order to ensure that the controller that is optimal to the specific cost function is also optimal to the vehicle parameters and flight trajectory. The most important aspect of the controller is that it is stable. Therefore, stability requirements should have the largest weight in the cost function. In order to analyze the stability of the current design within *fminsearch* the current gain estimates are placed into a state space model and combined with the plant which remains constant throughout the entire optimization process. Feedback is then applied closing the loop between the plant and the controller. Due to nonlinear coupling it is important to note that stability analysis for the gimbal

controller has to be done separate from the thrust controller in the second control design. The linear model used for the first control designs is shown below.

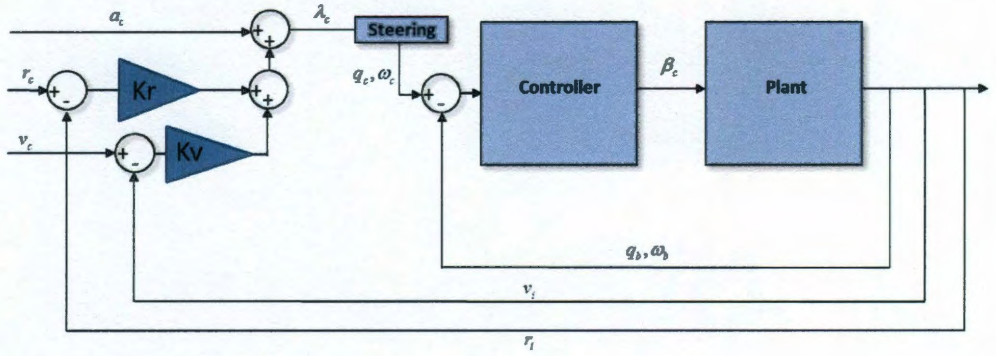

Figure 3-9: Representation of Control Design Model for Control Design 1

Control design 2 is setup for analysis in a similar manner. The difference is now the controller inputs the body quaternion and rate as well as the inertial position and velocity of the vehicle. The controller output remains the same and is simply the desired gimbal angles. The thrust control is designed separately from the gimbal controller. The linear model used for the second control design is show below.

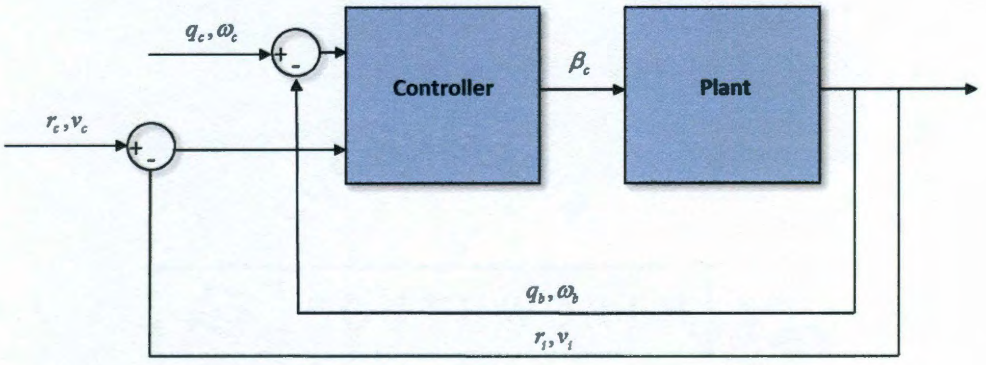

Figure 3-10: Representation of Control Design Model for Control Design 2

In order to evaluate the stability margins the closed loop system must be "broken" at a point where the margins are to be calculated. The stability margins are desired between the controller and the plant therefore the loop will be broken in between the controller and plant as shown below.

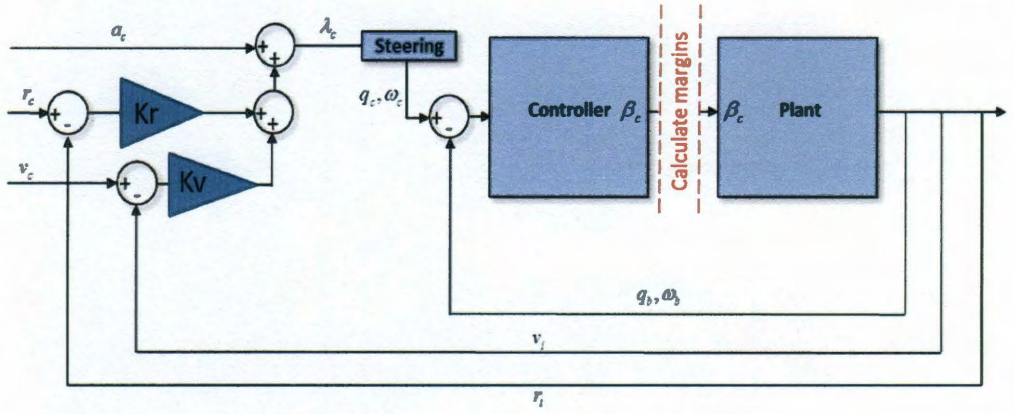

Figure 3-11: Control Loop Stability Margin Location for Control Design 1

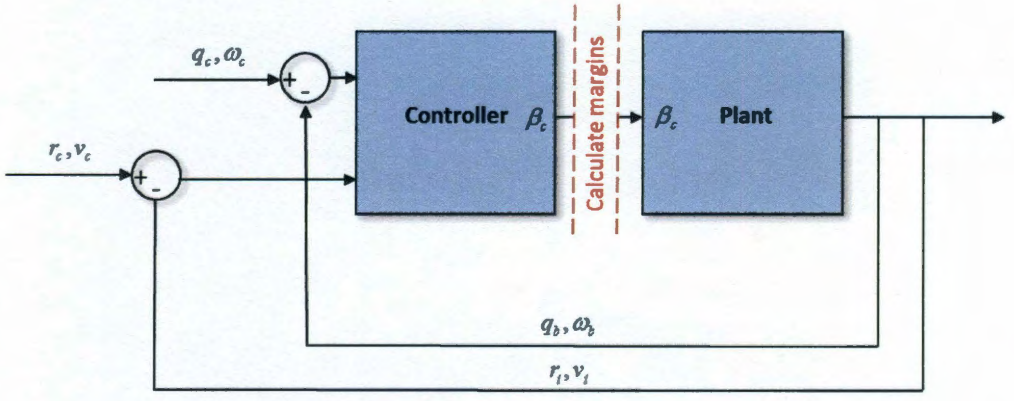

Figure 3-12: Control Loop Stability Margin Location for Control Design 2

The gain, phase, and delay margins are calculated. If the gain margin is below 6 dB a penalty is added in order to bring the gain margin up to 6 dB. In addition if the phase margin is below 30 degrees then a penalty is also added to increase gain margin. Each

margin can be weighted to have varying effects on the optimal solution. The overall cost function is given as

$$Cost = Cost + w_{gain}\left(\left(\frac{GM_{yy}}{6} - 1\right)^2 + \left(\frac{GM_{zz}}{6} - 1\right)^2\right) + w_{phase}\left(\left(\frac{PM_{yy}}{30} - 1\right)^2 + \left(\frac{PM_{zz}}{30} - 1\right)^2\right) + w_{rise}\left(t_{rise_{yy}} + t_{rise_{zz}}\right) + w_{settle}\left(t_{sett_{yy}} + t_{sett_{zz}}\right), \quad (3.20)$$

where

GM_{yy}- Gain margin about Y axis

GM_{zz}- Gain margin about Z axis

PM_{yy}- Phase margin about Y axis

PM_{zz}- Phase margin about Z axis

$t_{rise_{yy}}$ - Rise time about Y axis

$t_{rise_{zz}}$ - Rise time about Z axis

$t_{sett_{yy}}$- Settling time about Y axis

$t_{sett_{zz}}$- Settling time about Z axis

and the various w values are the respective weights of each component of the cost function.

Additionally, a similar penalty could be used to increase delay margin as large as possible. A test is also done to determine if the closed loop system is unstable. If this is the case the algorithm will continue to iterate, not allowing an unstable configuration to be used as the solution. The algorithm will continue to drive the gains to make the vehicle as stable as possible. Also, several performance metrics were added. The performance metrics approximate the system as second order and calculate the system's rise time, settling time, and percent overshoot. Weights are added to each of these performance metrics to help drive gains which are both stable and satisfy the performance criterion.

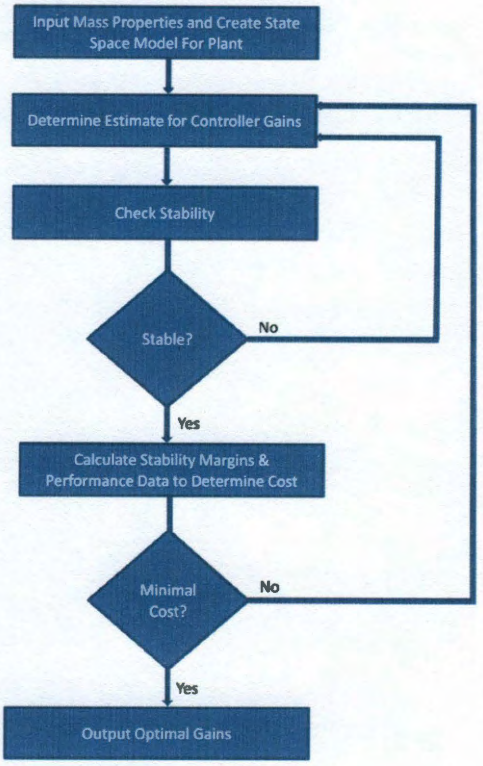

Figure 3-13: Algorithm to Determine Optimal Gains

3.7 Filter Design

Although a stable control design that meets desired vehicle performance has been discussed, a controller alone is not sufficient. This is because the control design has many assumptions, particularly that the attitude knowledge and error signals are ideal. In actual application these signals are not. The signals coming from sensors and processes to determine the state of the vehicle are inherently noisy. This noise and chatter can cause the controller to over react to the error signal as the controller tries to constantly make up for small changes in error, stability is lost in following the actual desired signal. Slosh motion can also have significant effects on the stability of the system. In order to smooth out the error signal and reduce high frequency noise a 4^{th} order filter is used.

3.7.1 Fourth Order Lowpass Filter

The 4th order filter is simply two second order filters multiplied together. Having two second order filters multiplied together offers more flexibility in the design of the system to help better attenuate the undesired frequencies. Each individual second order filter is modeled as its own second order transfer function. The second order transfer functions are assigned coefficients using the model of a simple spring mass damper. This gives the filter coefficients physical meaning and helps in selecting initial values. The respective second order transfer functions are multiplied by a coefficient in order to normalize the transfer function. This is important because by normalizing the filter there is no additional gain on the signal caused by the filter therefore this gain does not need to be considered in the control gain calculations. The basic transfer function of the filter is given as

$$F_{sys} = \left[\left(\frac{\omega_{fp1}}{\omega_{fz1}}\right)^2 \left(\frac{n_1 s^2 + 2\zeta_{fz1}\omega_{fz1} s + \omega_{fz1}^2}{d_1 s^2 + 2\zeta_{fp1}\omega_{fp1} s + \omega_{fp1}^2}\right)\right]\left[\left(\frac{\omega_{fp2}}{\omega_{fz2}}\right)^2 \left(\frac{n_2 s^2 + 2\zeta_{fz2}\omega_{fz2} s + \omega_{fz2}^2}{d_2 s^2 + 2\zeta_{fp2}\omega_{fp2} s + \omega_{fp2}^2}\right)\right]. \quad (3.21)$$

In order to properly attenuate the correct frequencies and smooth out the output of the signal, the correct filter coefficients must be chosen.

3.7.2 Scripted Optimization Algorithm for Filter Design

In order to select the proper coefficients an algorithm was developed similar to that developed in section 3.5.1 for finding the optimal control gains. The first part of the process is to create a plant and controller for which the filter is being developed. The algorithm for developing the optimal filter should be used after an optimal control design has been developed. This is because the filter is designed to improve an existing control

design. After the plant and controller designs have been found the next step is to determine an initial guess for the filter coefficients. This effort is aided by choosing the second order transfer function design for the filter since now only four frequencies and four damping ratios need to be determined. These can be chosen to be physically realistic to that of a spring-mass-damper model. It is important that the selected coefficients not result in a filter that causes the closed loop system to go unstable. Therefore, the next step is to check the stability of the system. This is done in an identical matter as with the controller. The only difference is that the closed loop system now includes the filter in addition to the controller and plant. Diagrams for the margin analysis of the respective control designs are shown below.

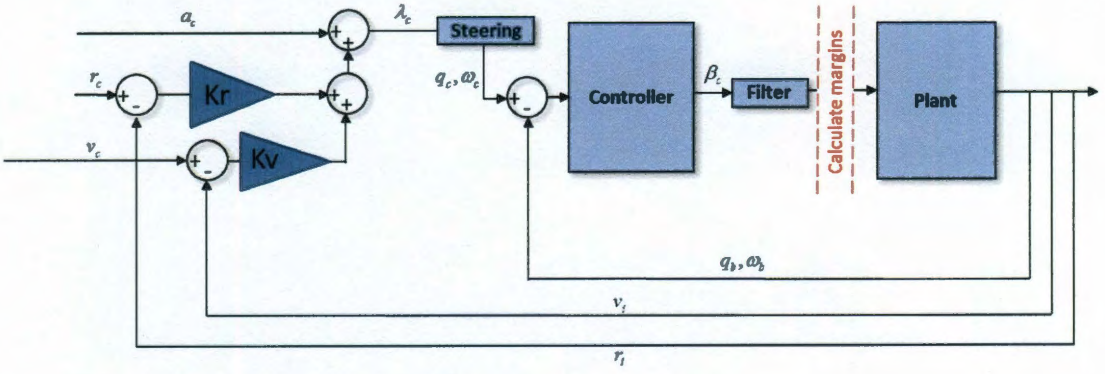

Figure 3-14: Filtered Control Loop Stability Margin Location for Control Design 1

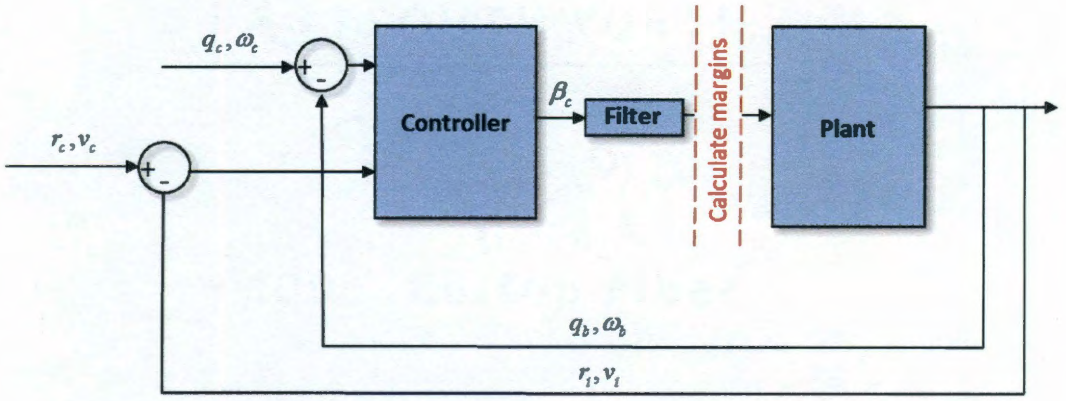

Figure 3-15: Filtered Control Loop Stability Margin Location for Control Design 2

Once initial coefficients have been selected the script can enter an optimization algorithm to determine the optimal filter coefficients. This optimization algorithm is similar to that of the control gain optimization algorithm shown previously. The largest improvements the filter will make to the system are increasing delay margin and increasing stability. Therefore these two components of the cost function should have the greatest weight. The cost function for optimal filter design is

$$cost = cost + w_{gain}\left(\left(\frac{GM_{yy}}{6} - 1\right)^2 + \left(\frac{GM_{zz}}{6} - 1\right)^2\right) + w_{phase}\left(\left(\frac{PM_{yy}}{30} - 1\right)^2 + \left(\frac{PM_{zz}}{30} - 1\right)^2\right) + w_{rise}\left(t_{rise_{yy}} + t_{rise_{zz}}\right) + w_{settle}\left(t_{sett_{yy}} + t_{sett_{zz}}\right) + w_{delay}\left((1 - DM_{yy}) + (1 - DM_{zz})\right), \quad (3.22)$$

where:

GM_{yy}- Gain margin about Y axis

GM_{zz}- Gain margin about Z axis

PM_{yy}- Phase margin about Y axis

PM_{zz}- Phase margin about Z axis

$t_{rise_{yy}}$ - Rise time about Y axis

$t_{rise_{zz}}$ - Rise time about Z axis

$t_{sett_{yy}}$- Settling time about Y axis

$t_{sett_{zz}}$- Settling time about Z axis

DM_{yy}- Gain margin about Y axis

DM_{zz}- Gain margin about Z axis

and the various w values are the respective weights of each component of the cost function.

The optimization code is used find the filter coefficients which minimize the respective cost function. An overview of this algorithm is shown below in Figure 3-16.

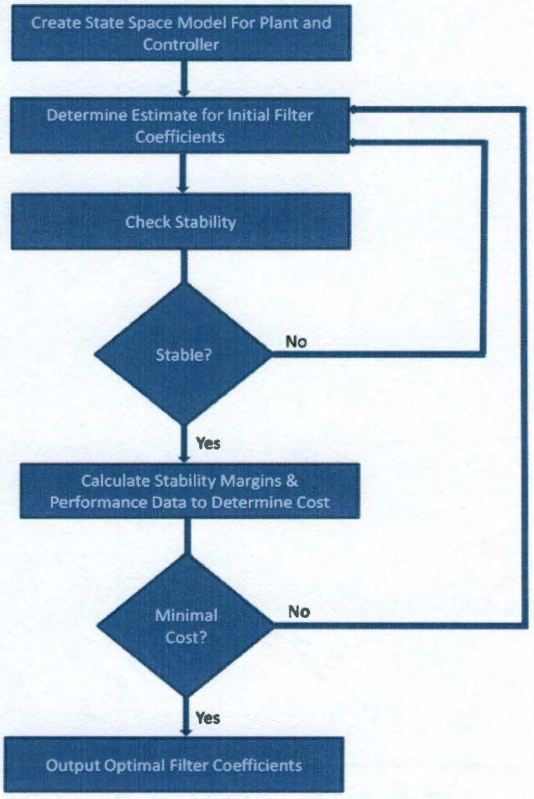

Figure 3-16: Algorithm for Optimal Filter Coefficient Determination

This algorithm can continue to iterate with the algorithm for optimal gain determination in order to further optimize the entire control system.

3.8 Vehicle Geometry Optimization

Previous discussion has focused on modifying the controller and filter to increase the stability of the system. These approaches have assumed that the plant is of a constant configuration with the ability to change the mass parameters in terms of fuel levels. The next approach to improving stability focuses on optimizing the vehicle's geometric properties. Since the structure of the airframe and integration of the gimbaled engine for a lander is fairly complex, optimization will focus on the position of the propellant tanks. The propellant tanks are an extremely significant factor in the stability of the vehicle. The main reasons for this are that the propellant makes up a majority of the vehicle mass and also that the large mass of the propellant has significant slosh effects. These factors make the position of the propellant tanks relative to the airframe center of mass important. Due to the large effect of slosh, analysis will be done on two tank shapes which use separate slosh models. The first analysis will discuss the optimal design of a vehicle with spherical propellant tanks and the second will discuss the optimal design of a vehicle with cylindrical propellant tanks.

3.8.1 Spherical Tank Analysis

Spherical tanks are extremely beneficial in terms of efficiency. This is because spherical tanks are capable of holding the largest volume of propellant for the smallest amount of tank surface area. This means that there are significant efficiency benefits due to the weight reduction of using less material to carry a specified amount of propellant [21]. The disadvantage of using a spherical tank is that due to its geometry the propellant in the tank has greater freedom to move. This means that the vehicle will be much more susceptible to the effects of slosh than other designs. This is largely due to the fact that as

the vehicle and the tanks move all of the propellant in a spherical tank is free to move as well [22]. The movement of the propellant in a spherical tank can be visualized below in Figure 3-17.

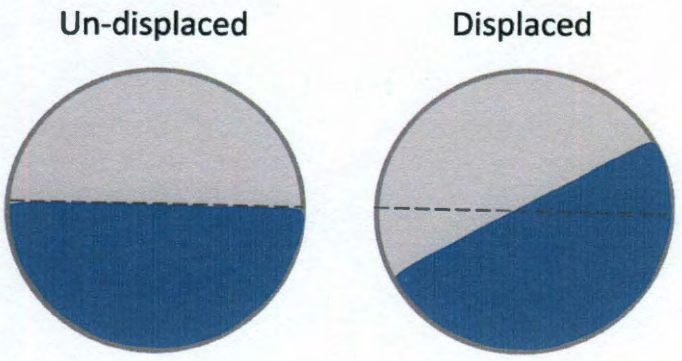

Figure 3-17: Visualization of Propellant Movement in a Spherical Tank

Since the effects of sloshing propellant will be quite significant in a spherical tank, the placement of these tanks on the vehicle becomes even more critical to the vehicle's stability. In order to analyze the stability and determine the optimal tank location the linear model created for control design is used. A script file is then used to change the location of the tanks and their respective propellant masses with respect to the airframe center of mass. In this script file an arbitrary vehicle design is chosen consisting of four propellant tanks, a rigid airframe, and a gimbaled engine that is assumed fixed in its neutral position. The height of all four tanks and their position relative to the centerline of the airframe are assumed to be equal to each other. This assumption is necessary because symmetry needs to be maintained in order to maximize stability. An arbitrary initial tank position is chosen at some point well below the airframe center of mass and relative to the airframe centerline. A nested loop is then used to sweep through horizontal tank

positions relative to the airframe centerline and vertical tank position relative to the initial tank height as shown in Figure 3-18.

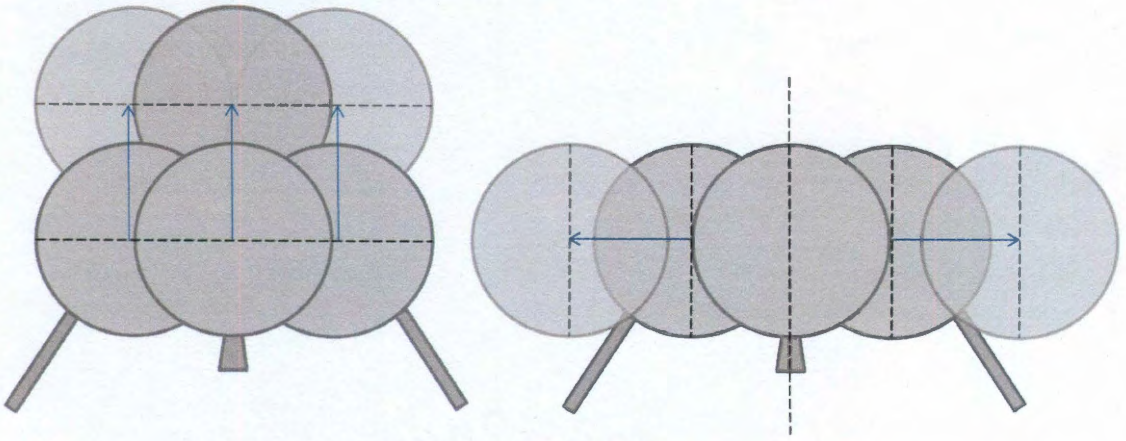

Figure 3-18: Sweep Analysis of Spherical Tanks to Determine Optimal Configuration

Stability margins are then calculated and stored for each tank configuration within the nested loop. From this data the optimal spherical tank position is able to be computed.

3.8.2 Cylindrical Tank Analysis

Cylindrical tanks are advantageous because their shape affords greater practicality in implementation on a launch vehicle. The large round shape of spherical tanks often results in sizing issues with a particular launch vehicle [21]. In the particular application of a planetary lander this may not be as significant because the lander itself is small relative to the launch vehicle. However, cylindrical tanks cause far less slosh effects than spherical tanks and for this reason it is worth analyzing a cylindrical tank design in an effort to further reduce slosh and increase stability. In a spherical tank all of the propellant mass which is typically very significant relative to the vehicle mass, is the slosh mass. In a cylindrical tank the majority of the propellant remains static and only a

fraction of the propellant mass is assumed dynamic. A visualization of why this assumption is made can be seen below in Figure 3-19.

Figure 3-19: Visualization of Propellant Movement in a Cylindrical Tank

As the vehicle moves, the propellant attempts to respond to the vehicle's behavior however unlike in a spherical tank where all of the propellant was free to "slide" up the wall of the tank, in a cylindrical tank the walls restrict the motion of the fluid. This means that a portion of the propellant is static and the portion that is unconstrained remains fluid. This concept is shown in Figure 3-20.

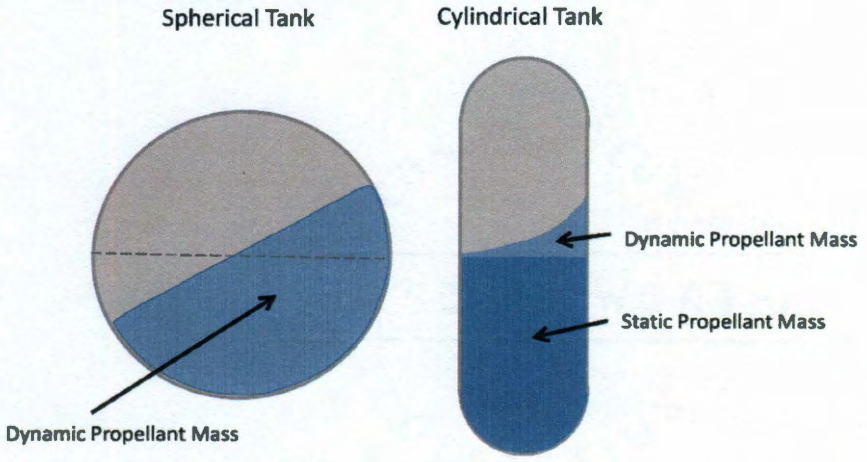

Figure 3-20: Comparison of Propellant Movement in Spherical and Cylindrical Tanks

The mass of the sloshing fuel m_{slosh} can be found by using the equation [22]

$$m_{slosh} = \left(\frac{d_{cyl} \tanh\left(\frac{2\zeta_s h_{liq}}{d_{cyl}}\right)}{\zeta_s(\zeta_s^2 - 1)h_{liq}} \right) m_{prop}. \tag{3.23}$$

Where d_{cyl} is the diameter of the cylindrical tank, ζ_s is the effective slosh model damping ratio of the liquid, m_{prop} is the total mass of the propellant in the tank and h_{liq} is the height of the liquid in the tank which can be found using the equation [22]

$$h_{liq} = \frac{4m_{prop}}{\pi \rho_{liq} d_{cyl}^2}. \tag{3.24}$$

Where ρ_{liq} is the density of the liquid inside the tank [22]. Since part of the propellant is now assumed static the plant used for the spherical tank and control design analysis will no longer suffice. In the previous linear model the assumption was made that the propellant had no rotational inertia contribution to the overall inertia of the airframe and could therefore be treated as a point mass. It is now necessary to include the mass of the

static portion of the propellant in the airframe composite inertia. This can easily be done using the calculations in Equation (3.24) to calculate the slosh mass. The slosh mass can then be subtracted from the propellant mass to find the static mass. The mass of the static portion of the propellant can then be added to the vehicle's inertia using the parallel-axis-theorem [9][23]. The remaining dynamic mass is then treated as the sloshing mass in the linear set of equations described in Chapter 2. Once the plant is formed using an arbitrary propellant load, the optimal tank location can be found by sweeping the tank positions in the same fashion used for the spherical tank geometry as shown in Figure 3-21.

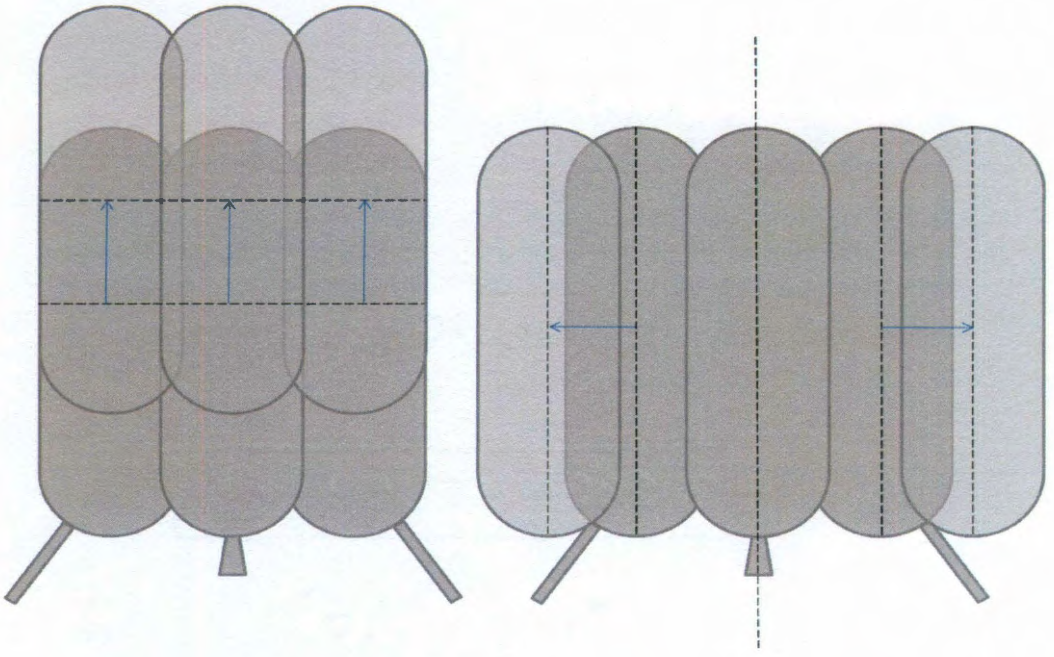

Figure 3-21: Sweep Analysis of Cylindrical Tanks to Determine Optimal Configuration

After the sweep is complete a smaller step size can be used to sweep through configurations close to the current optimal configuration in order to increase the accuracy of the optimal tank locations.

4 Results

In order to properly compare the various control designs it is necessary to both analyze the stability of the systems in the frequency domain as well as analyze the performance of the designs in the time domain. To accomplish this task a frequency domain and a time domain simulation are needed. A six degree of freedom time domain simulation is created using the non-linear equations of motion described in [11]. A tool for frequency domain analysis is also created using the linearized equations of motion described in Chapter 2.

The time domain simulation is organized into four main blocks. The guidance block provides the appropriate acceleration, position, and velocity commands in the inertial reference frame. The steering block converts the acceleration command into an appropriate quaternion and body rate command. The control block provides the appropriate gimbal angle and thrust to the dynamics block by referencing the error between the command and the actual vehicle state. The control block is set up to provide the appropriate thrust and gimbal controls based off each of the respective control designs. The dynamics block simulates the behavior of the system using the non-linear six degree of freedom equations of motion. Since the non-linear equations describe motion in the body frame, the dynamics block rotates the appropriate position and velocity states into the inertial frame so that control can be accomplished. The simulation

can be easily modified for any vehicle, set of mass properties, initial state or environment. The overall setup of the simulation can be seen in Figure 4-1.

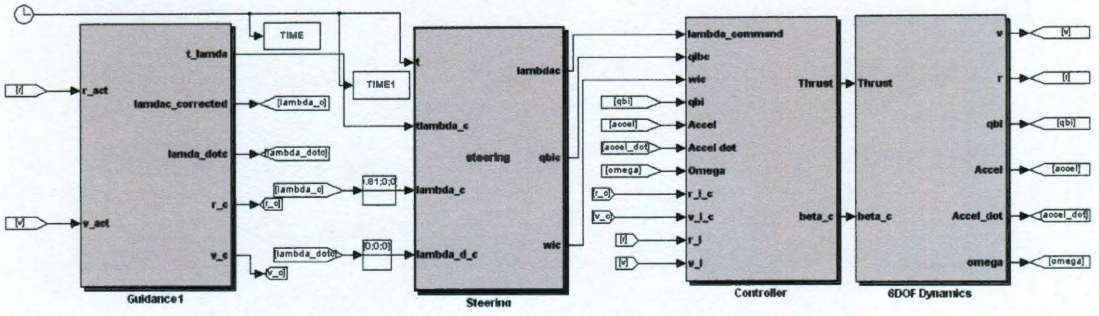

Figure 4-1: Top Level Time Domain Simulation Layout

Stability analysis is performed in a separate simulation using the linear state space model developed in Chapter 2. The frequency domain simulation is capable of analyzing stability margins for a particular vehicle configuration as well as developing optimally stable controllers for a specified flight profile. A distinct advantage in the linear model being developed directly from the equations of motion in the time domain simulation is that time domain simulation flight data such as the thrust profile and vehicle mass properties over time can be directly input into the frequency domain simulation. This allows accurate stability analysis of the control designs throughout the entire profile. In order to properly test and verify the control designs in the simulation, various trajectories are developed for the controller to fly. These trajectories are the jump trajectory, a high fidelity trajectory, and a lunar descent trajectory.

4.1 Jump Trajectory

The first trajectory that the control designs are analyzed with is the jump trajectory. This trajectory is designed to be the simplest of the three trajectories in order to test the

basic capabilities of the control designs. The jump trajectory simulates a realistic application of a gimbaled engine vehicle where the vehicle would be stationary on the ground, lift off to a prescribed altitude and then translate over to a new location, descend, and land. This trajectory is assumed to be on Earth. To add complexity to this relatively simple trajectory the translation of the vehicle is done in both the inertial Y and Z directions requiring the engine to gimbal in a more complex manner than if the translation were purely planar. A visualization of the jump trajectory is shown below in Figure 4-2.

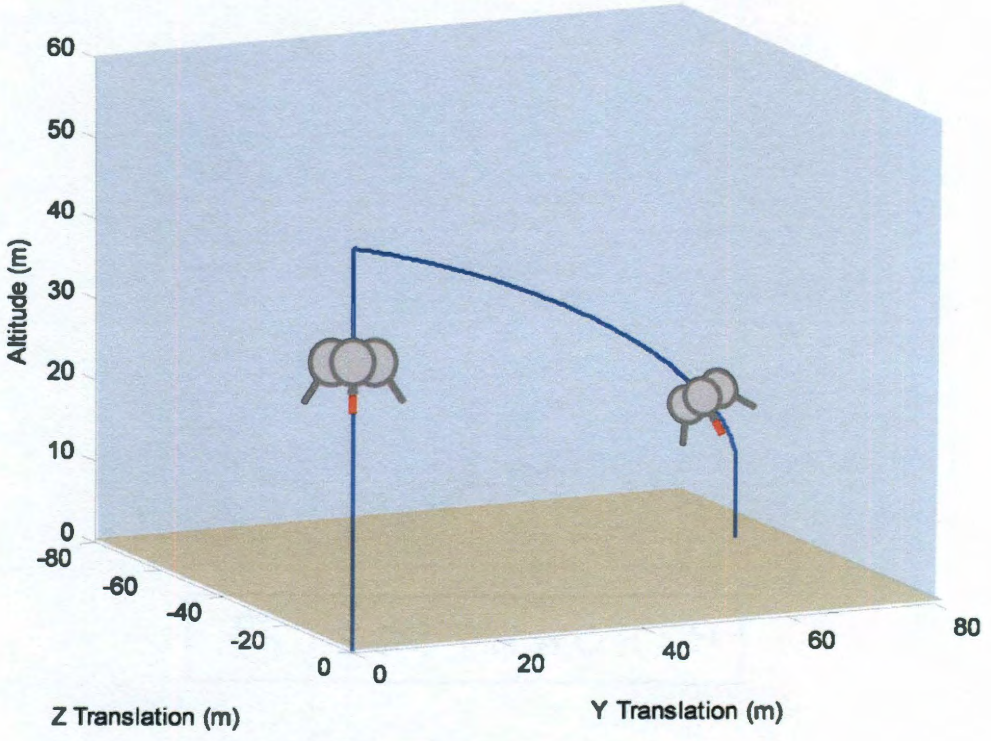

Figure 4-2: Visualization of Jump Trajectory

In this trajectory the vehicle ascends 50 meters from the origin point then begins to translate to a point 75 meters in the inertial Y direction and -50 meters in the inertial Z

direction as it descends to an altitude of 10 meters. The vehicle then descends vertically and lands.

4.1.1 Control Gain Selection

Optimal control designs were developed for this particular trajectory. This was done using the methods described in Chapter 3. The stability analysis is done only with respect to the gimbal of the vehicle. Since the control gains are fixed with time the controller was designed to provide optimal stability and performance at a point just over halfway through the translation phase. This is desirable because although on first thought it might appear best to develop the controller based off the average stability of the entire trajectory, doing so will result in a less optimal controller during the translation phase because the design will adjust to include a phase of flight where no translation occurs and therefore no gimbal motion occurs. Designing to a point midway through the translation affords the benefit of ensuring maximum stability and performance during the most critical phase of the flight. The optimal gains for the jump trajectory are shown below in Table 4-1.

Table 4-1: Optimal Control Gains for Jump Trajectory

	ω_{rot} (Hz)	ζ_{rot}	ω_{trans} (Hz)	ζ_{trans}	ω_{Thrust} (Hz)	ζ_{Thrust}
Control Design 1	0.5360	0.7400	N/A	N/A	N/A	N/A
Control Design 2	0.4624	0.7848	0.0945	0.7645	0.5000	1.0000

The following relationship is then used to determine the un-scaled proportional and derivative gains of the system, K_p and K_d respectively

$$K_p = \omega^2$$
$$K_d = 2\zeta\omega. \tag{4.1}$$

In order to ensure that the gains remain valid throughout the entire flight profile the gains are then scaled by the appropriate vehicle mass properties. The scaling terms for the respective gains are

$$Rotation\ Gain\ Scaling\ Factor = \left(\frac{\underline{I}^{\overline{Ccm}}}{F\left(r_x^{\overline{G}}\right)}\right),$$
$$Translation\ Gain\ Scaling\ Factor = \left(\frac{m^t}{F}\right), \tag{4.2}$$
$$Thrust\ Gain\ Scaling\ Factor = m^t,$$

where

$\underline{I}^{\overline{Ccm}}$ – Total inertia about the composite center of mass

F - Magnitude of the force of thrust

$r_x^{\overline{G}}$ – Body frame x component of the vector from the gimbal to the composite center of mass

m^t - Total vehicle mass.

The optimally developed control designs were then implemented in the time domain simulation with the appropriate gain scaling.

4.1.2 Jump Trajectory Performance Results

The simulation is run for a constant time of 68.5 seconds. The controller is run at 25 Hz and guidance is run at 2 Hz. The resulting position without any disturbances is plotted in reference to the commanded trajectory. This result gives an understanding of how aptly the control design is able to follow the commanded trajectory in the simplest,

most ideal case. The resulting position trajectories for control designs 1 and 2 are shown in Figure 4-3 and Figure 4-4.

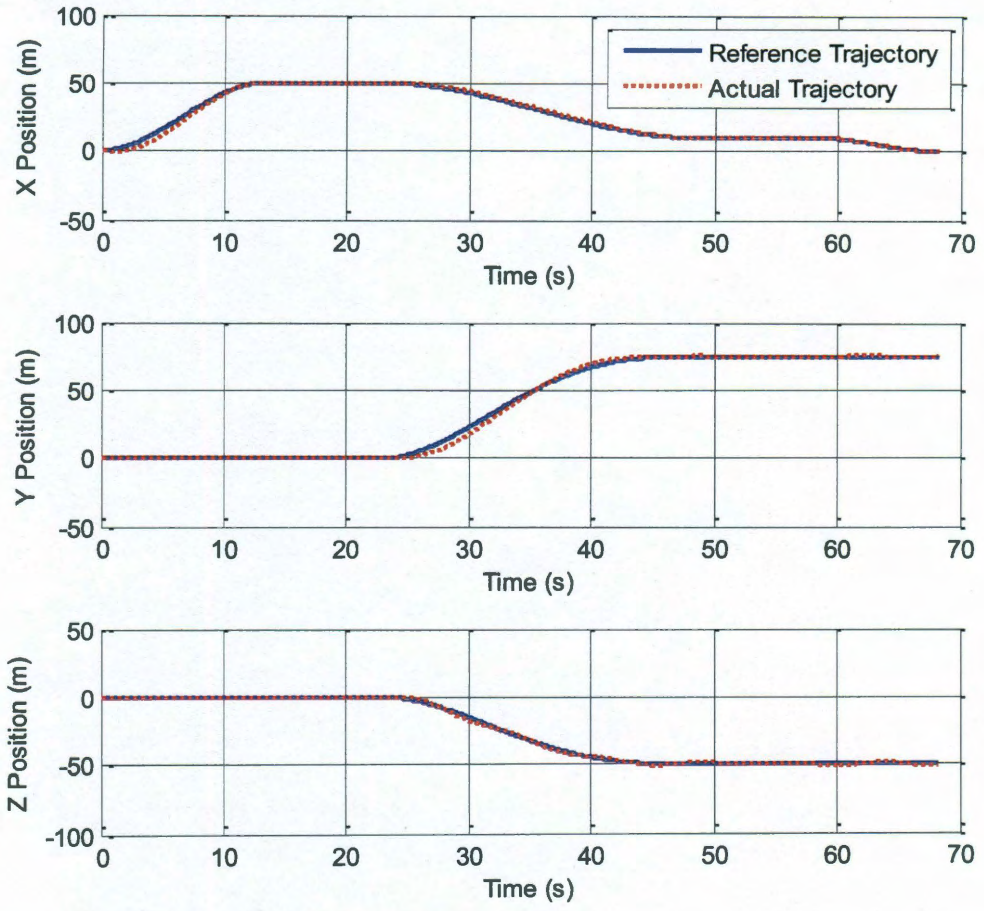

Figure 4-3: Control Design 1 Position Compared with Reference Jump Trajectory

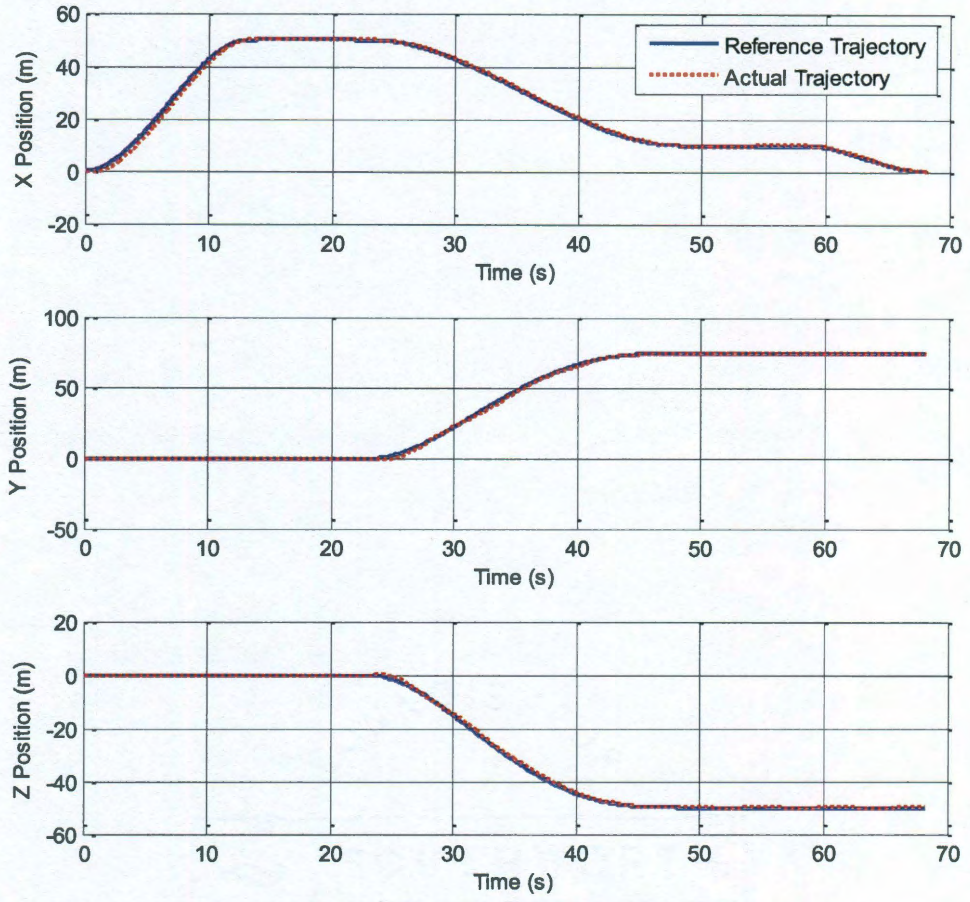

Figure 4-4: Control Design 2 Position Compared with Reference Jump Trajectory

These plots show that in the most ideal, undisturbed case control design 2 appears to follow the commanded trajectory better than control design 1. A more accurate representation of the ability of each of the control designs to follow the prescribed trajectory is a plot of the position error of the vehicle from the commanded reference position over time. Error plots of control designs 1 and 2 are shown in Figure 4-5.

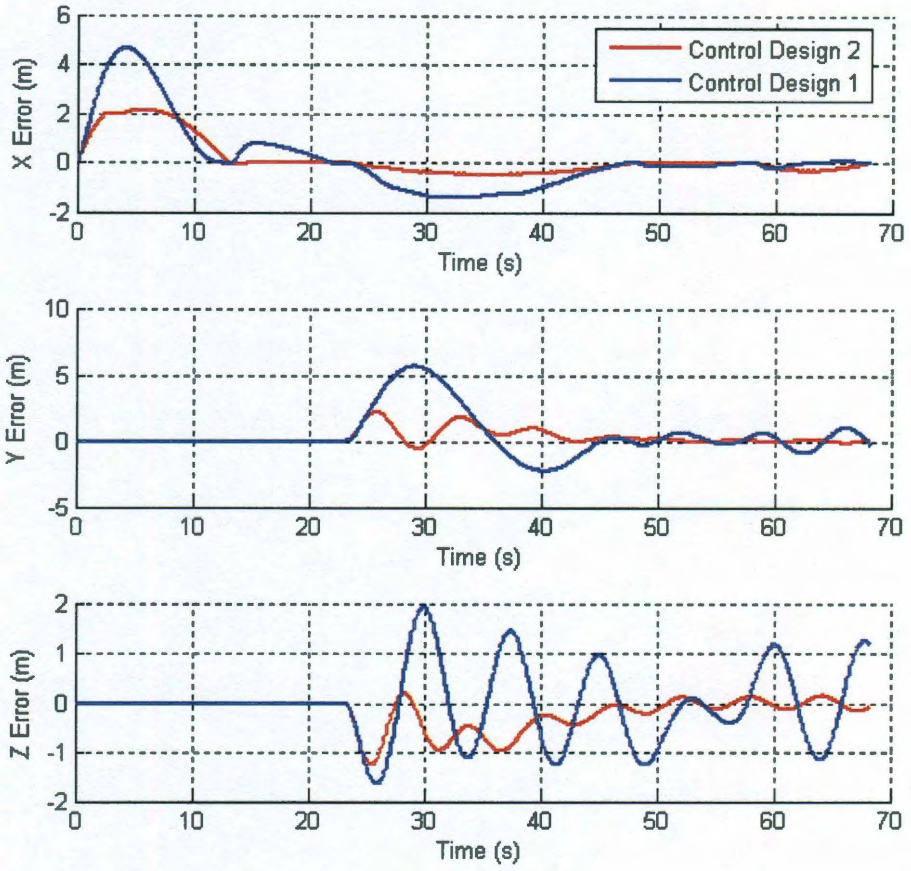

Figure 4-5: Jump Trajectory Position Error

The plots of position error show a generally greater error in all three positions for control design 1. Additionally, the terminal error at the end of the simulation appears significantly larger in control design 1 than in control design 2, particularly with respect to the Y direction.

To understand how the vehicle is behaving throughout the trajectory it is important to analyze the rotation of the vehicle in addition to its translation. The rotation of the vehicle for the jump trajectory for control designs 1 and 2 can be seen in Figure 4-6.

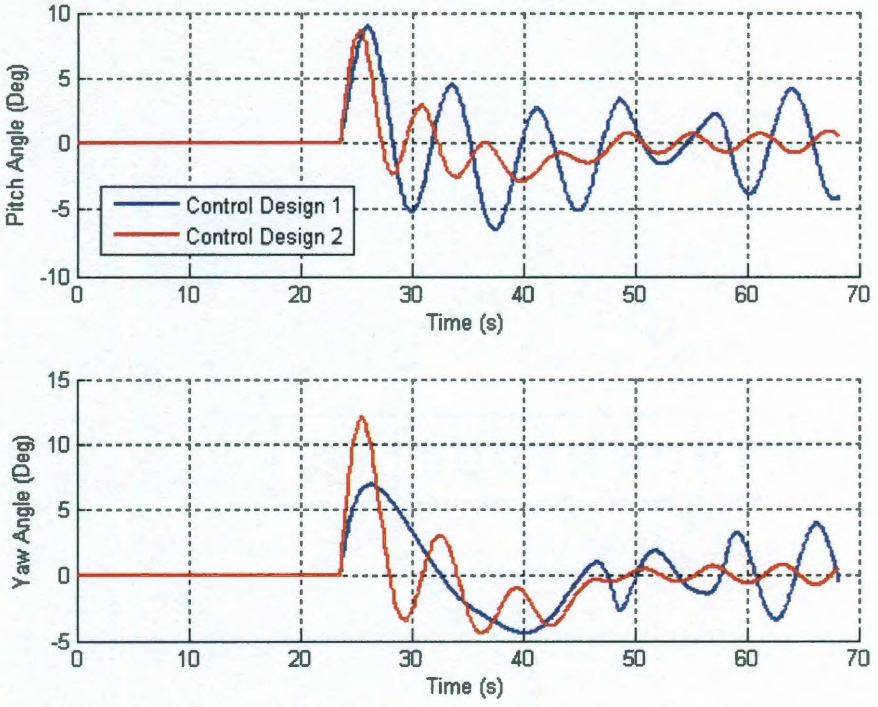

Figure 4-6: Jump Trajectory Rotation Angle Performance

Control designs 1 and 2 both show rotation on a similar scale and both designs allow the vehicle to roll significantly. Since there is no control on roll assumed for this analysis both designs have no ability to correct for the roll error created though coupled gimbaling of the engine about both axes. Control design 1 responds significantly less smoothly to the commanded trajectory than control design 2 as well. The increased response is because the control gains become extremely large as the vehicle approaches the end of a stage and this causes the vehicle to approach instability.

A general summary of the jump trajectory performance results for the control designs is shown below in Table 4-2

Table 4-2: Summary of Jump Trajectory Performance Results

	Maximum Vertical Position Error (m)	Average Vertical Position Error (m)	Maximum Horizontal Position Error (m)	Average Horizontal Position Error (m)	Maximum Vehicle Pitch/Yaw Angle (degrees)	Maximum Engine Gimbal Angle (degrees)
Control Design 1	4.6618	0.8475	5.6722	0.71725	8.9482	5.1723
Control Design 2	2.1462	0.1756	2.2410	0.1496	12.0432	20.00

Both designs very capably flew the desired trajectory. Control design 1 had slightly greater error than control design 2 and had significant oscillations in the gimbal and rotation angles. Control design 2 more closely followed the commanded trajectory but doing so required larger control inputs.

4.1.3 Jump Trajectory Stability Results

It is critical to perform an accurate stability analysis on the control designs to ensure there is adequate margin throughout the trajectory. For the purposes of this application, adequate margins are defined to be 6 dB of gain margin, 30 degrees of phase margin, and 0.05 seconds of delay margin. The frequency domain simulation is used to generate stability margins throughout the flight profile. The results of the stability analysis are shown below in Table 4-3.

Table 4-3: Summary of Jump Trajectory Stability Results

	Maximum Positive Gain Margin (dB)	Minimum Positive Gain Margin (dB)	Maximum Positive Phase Margin (deg)	Minimum Positive Phase Margin (deg)	Maximum Positive Delay Margin (sec)	Minimum Positive Delay Margin (sec)
Control Design 1 Y-axis	12.00	2.25	134.45	6.95	0.35	0.01
Control Design 1 Z-axis	11.38	5.63	132.92	27.64	0.33	0.03
Control Design 2 Y-axis	13.31	12.84	58.06	56.18	0.09	0.08
Control Design 2 Z-axis	13.78	13.39	58.30	56.41	0.09	0.09

These results show that control design 2 has larger gain and delay margins than control design 1. This is because the gains in control design 1 change with time. The gains begin very small and the control design has adequate margin but as time approaches the end of a stage the gains become extremely large and margins are reduced greatly. The vehicle is even momentarily unstable for portions of the flight profile because of this but is able to fly through the instability. The constant gains of control design 2 which are scaled for the vehicle mass properties at the specified time result in stability margins that deviate very little throughout the flight profile. To properly visualize the control response, closed loop step responses were generated. The step response, although an approximation, allows the time domain response of the controller to be visualized. The step responses for both control designs at the end of the trajectory are shown below in Figure 4-7.

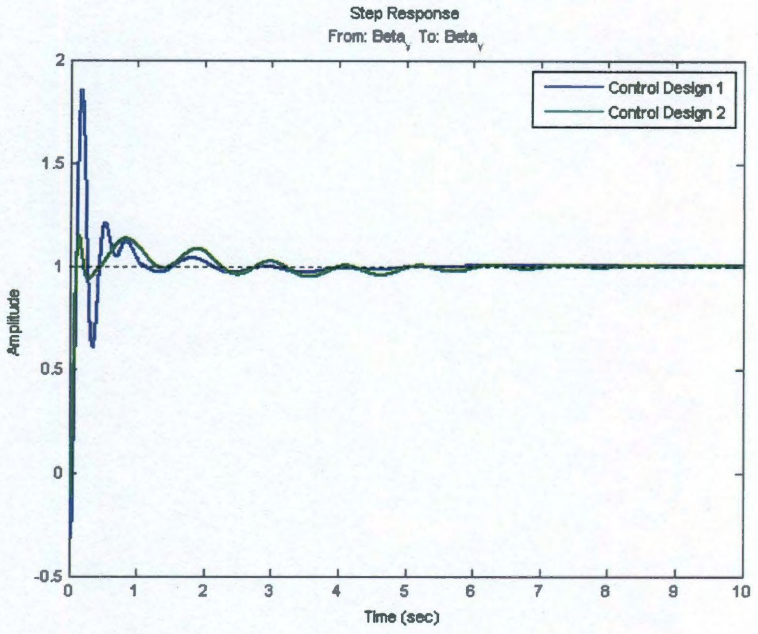

Figure 4-7: Control Design Jump Trajectory Closed Loop Step Responses

The step response plots show that control design 1 has slightly larger overshoot but less settling time than the step response of control design 2. Although control design 1 becomes unstable during portions of the flight it is still able to fly the trajectory however control design 2 is stable throughout the profile and is able to more accurately fly the trajectory.

4.2 High Fidelity Trajectory

The jump trajectory was designed to validate the basic capabilities of each of the control designs to follow a commanded trajectory in all directions. In order to fully compare the control designs a more demanding trajectory is desired in order to push the limits of the controller. The high fidelity trajectory was designed to require the vehicle to fly a considerable distance in a short time while either ascending or descending for the entire profile. This requires the vehicle to provide a larger gimbal angle to provide the

necessary control to increase velocity and follow the commanded trajectory. The high fidelity trajectory initially starts on the ground 1.7 km downrange. The vehicle lifts off to an altitude of 50 feet before beginning a translation of 1.7 km back to the origin. The vehicle ascends to an altitude of .5 km while translating. Once the vehicle reaches this altitude it immediately begins descending to an altitude 75 m off of the ground while continuing its translation. The vehicle then enters a short hover descends and lands. A visualization of this trajectory is shown in Figure 4-8.

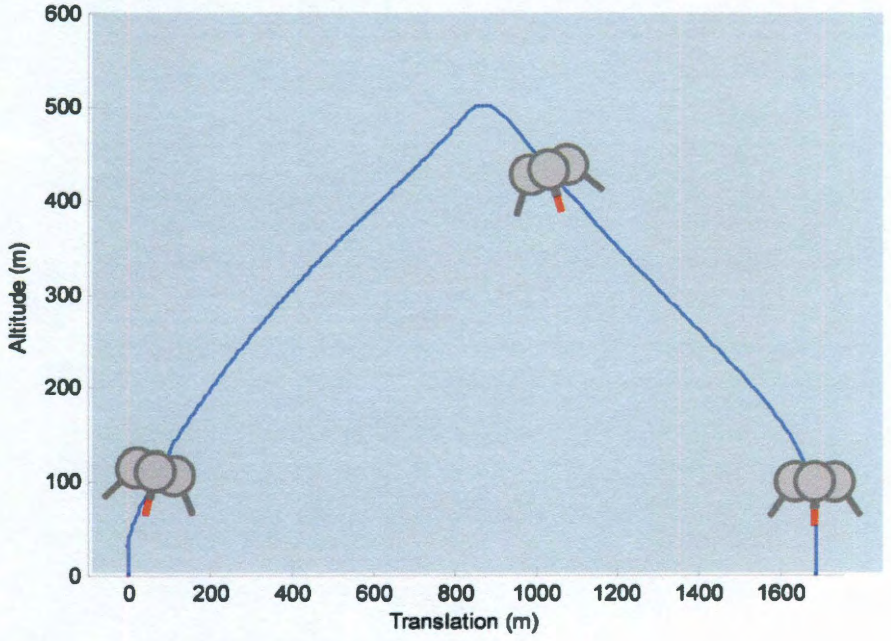

Figure 4-8: Visualization of High Fidelity Trajectory

4.2.1 Control Gain Selection

The methods described in Chapter 3 can be used to develop optimal control designs for the high fidelity trajectory in the same fashion as the jump trajectory. Since the control design is fixed with respect to time it is again desirable to design gains at a

point halfway through the translation phase. This technique should optimize stability throughout the entire translation phase. Additionally it is beneficial to tune the cost function to the specified trajectory as well. For the high fidelity trajectory increasing performance criteria weighting may be necessary in order to follow the trajectory, although stability margins may be sacrificed. The optimal gains for the high fidelity trajectory are shown below in Table 4-4.

Table 4-4: Optimal Control Gains for High Fidelity Trajectory

	ω_{rot} (Hz)	ζ_{rot}	ω_{trans} (Hz)	ζ_{trans}	ω_{Thrust} (Hz)	ζ_{Thrust}
Control Design 1	0.7511	0.9777	N/A	N/A	N/A	N/A
Control Design 2	0.4762	0.8662	0.0915	0.6034	0.5000	1.0000

The control gains are found from the frequency and damping using the same relationship as equation (4.1). The gains are scaled using the same gain scaling as in the jump trajectory (4.2). These control designs show the increase in the rotational control gains as the controller is designed to better meet the performance requirements of the high fidelity trajectory.

4.2.2 High Fidelity Trajectory Performance Results

The simulation is run for a constant time of 152 seconds. The controller is run at 25 Hz and guidance is run at 2 Hz. The trajectory is flown without any disturbances assuming ideal knowledge of the vehicle states and mass parameters. The results from this ideal simulation show how the control designs perform under the most optimal conditions in order to understand their expected performance. The actual flown position

of the vehicle is plotted with respect to the commanded trajectory and is shown below for each of the control designs.

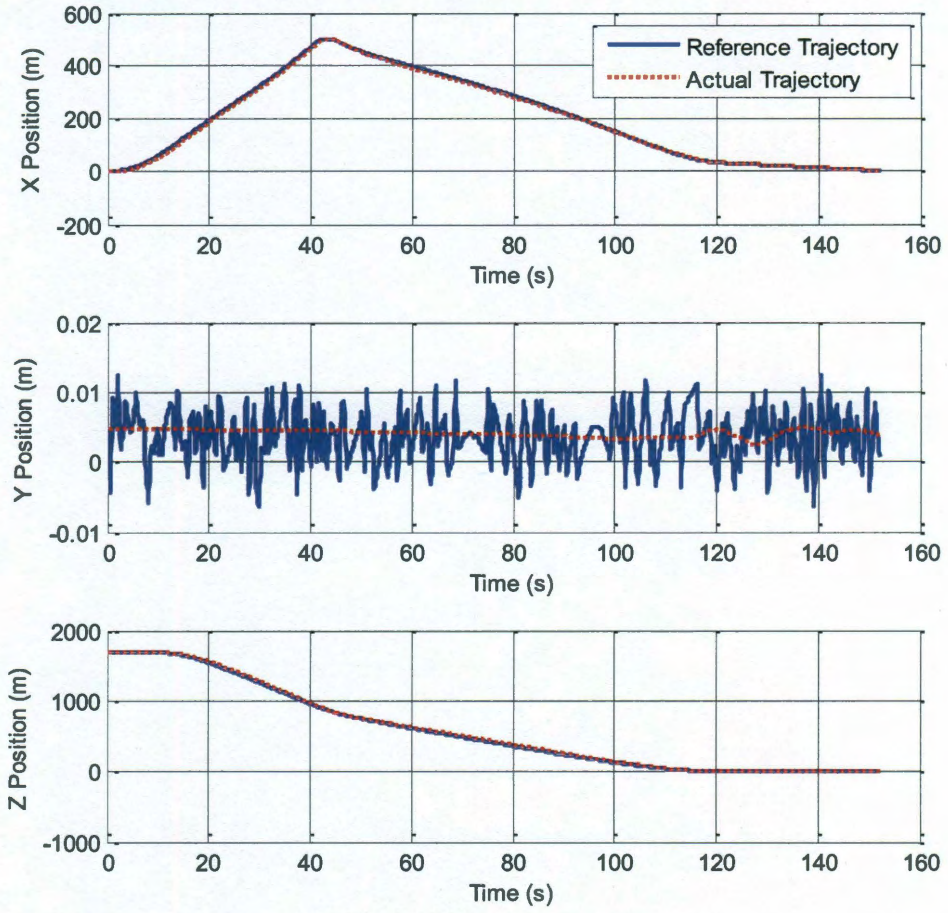

Figure 4-9: Control Design 1 Position Compared with Reference High Fidelity Trajectory

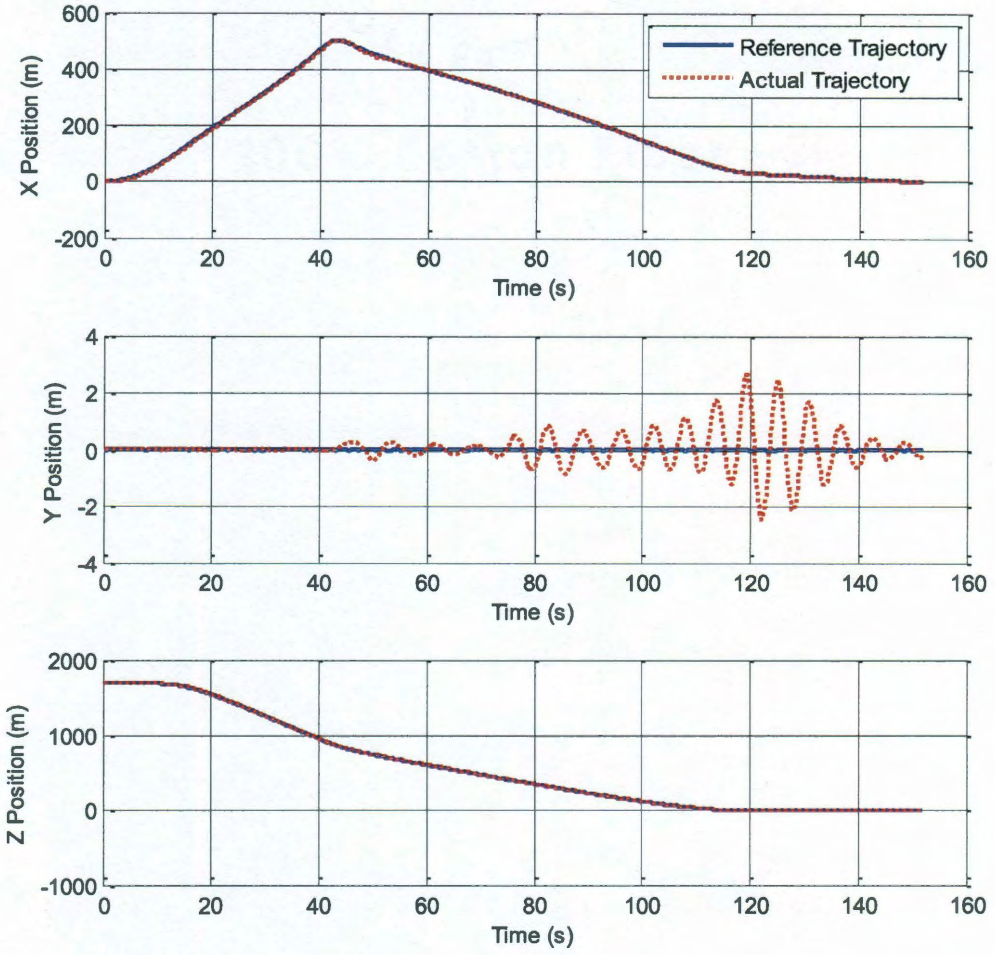

Figure 4-10: Control Design 2 Position Compared with Reference High Fidelity Trajectory

These results initially show that control design 1 and control design 2 are both able to fly the more demanding high fidelity very similarly under ideal conditions. It is important to note that the reference signal of the Y position is inherently noisy which is done on purpose as part of the high fidelity trajectory design. In order to accurately analyze how well each of the controllers performed the position error of the vehicle with respect to the

commanded trajectory are plotted over time for each control design. These error plots are shown in Figure 4-11.

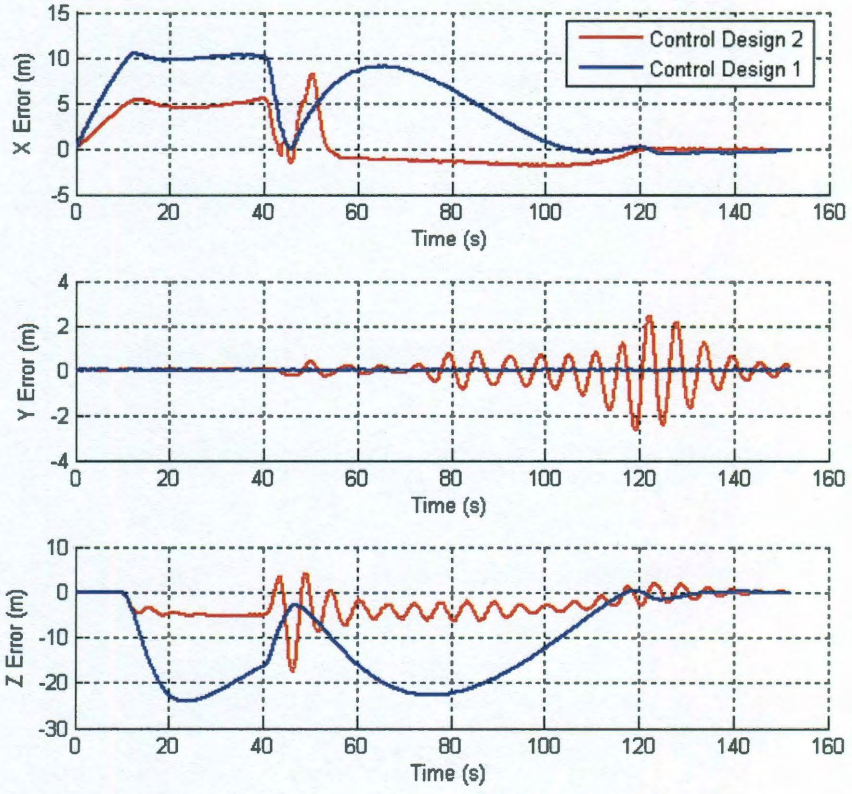

Figure 4-11: High Fidelity Trajectory Position Error

These error plots show that although both control designs fly the high fidelity trajectory well, with the exception of the Y position which is commanded to zero, control design 2 in general is able to fly the trajectory with less error. However, control design 1 is able to fly the trajectory more smoothly than control design 2.

To understand the behavior of the vehicle throughout the trajectory it is important to analyze the rotational behavior of the system in addition to the translational behavior. The rotation of the vehicle with respect to time is shown below in Figure 4-12.

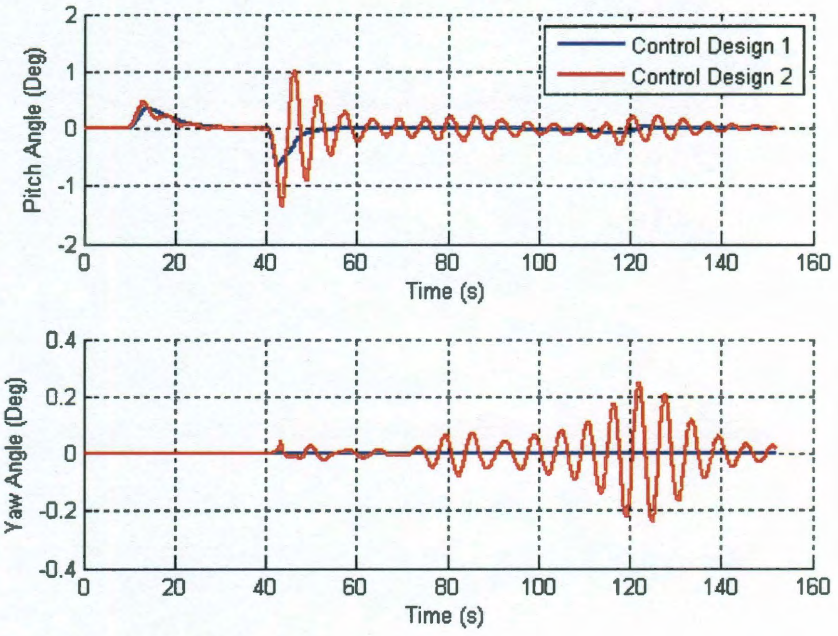

Figure 4-12: High Fidelity Trajectory Rotation Angle Performance

The rotation angle plots show that similar to the jump trajectory both control designs result in rotation on a similar order of magnitude. Control design 1 offers smoother rotation throughout the flight profile than control design 2. The more frequent corrections of the rotation angle found in the results for control design 2 are present because the controller is directly correcting to properly follow the position more accurately at a rate of 25 Hz where as control design 1 is only indirectly correcting for error at a much slower rate of 2 Hz. Although the increased corrections allow the vehicle to more accurately track the trajectory they can lead to an increase in the slosh motion of the propellant tanks.

A general summary of high fidelity trajectory performance results for both controller designs is shown below.

Table 4-5: Summary of High Fidelity Trajectory Performance Results

	Maximum Vertical Position Error (m)	Average Vertical Position Error (m)	Maximum Horizontal Position Error (m)	Average Horizontal Position Error (m)	Maximum Vehicle Pitch/Yaw Angle (degrees)	Maximum Engine Gimbal Angle (degrees)
Control Design 1	10.4302	4.6474	24.1555	5.3362	0.6412	20.00
Control Design 2	8.1600	2.0417	17.5314	0.2634	1.3734	20.00

Control designs 1 and 2 both had similar maximum position errors in the vertical direction. On average control design 2 had less vertical error than control design 1 however this error was still relatively small. Control design 2 had less maximum and average translational position error than control design 1. Both control designs saturated the gimbal at least once during the flight however control design 1 had approximately half the maximum angular rotation of control design 2. This shows that although control design 1 appeared to more smoothly follow the trajectory the maximum and average errors were slightly larger than control design 2. Therefore although control design 2 had oscillations in its velocity, it was still able to perform better than control design 1.

4.2.3 High Fidelity Trajectory Stability Results

It is essential that the controller designs are stable throughout the entire flight and that the controller has adequate margins to properly fly the trajectory under less than ideal conditions. Without margin, delays in the system or perturbations to the vehicle or controller could result in instability and compromise the vehicles ability to fly the trajectory. For the purposes of this application, adequate margins are defined to be 6 dB of gain margin, 30 degrees of phase margin, and 0.05 seconds of delay margin. The

frequency domain simulation is used to generate stability margins throughout the flight profile. The results of the stability analysis are shown below in Table 4-6.

Table 4-6: Summary of Jump Trajectory Stability Results

	Maximum Positive Gain Margin (dB)	Minimum Positive Gain Margin (dB)	Maximum Positive Phase Margin (deg)	Minimum Positive Phase Margin (deg)	Maximum Positive Delay Margin (sec)	Minimum Positive Delay Margin (sec)
Control Design 1 Y-axis	7.14	5.08	62.21	40.86	0.05	0.03
Control Design 1 Z-axis	7.04	5.03	61.42	40.56	0.05	0.02
Control Design 2 Y-axis	15.56	12.60	61.14	57.08	0.12	0.08
Control Design 2 Z-axis	15.68	13.09	61.23	57.47	0.12	0.09

The stability analysis shows that the minimum margins are met for control design 2 but there are again times that control design 1 does not meet the required stability margins. The margins for control design 1 are still better than for the jump trajectory design however the control design still becomes unstable at certain points of the flight as the vehicle approaches the end of each stage of the trajectory. This is similar to the results for the jump trajectory. For the high fidelity case control design2 on average has more phase margin, gain margin, and delay margin than control design 1. To properly visualize the controller's responses step responses are made of each control design at the end of the flight. Although the step response is an approximation it provides a visual representation of how the controller will respond to an input. The step responses for the control designs at the end of the trajectory are shown below in Figure 4-13.

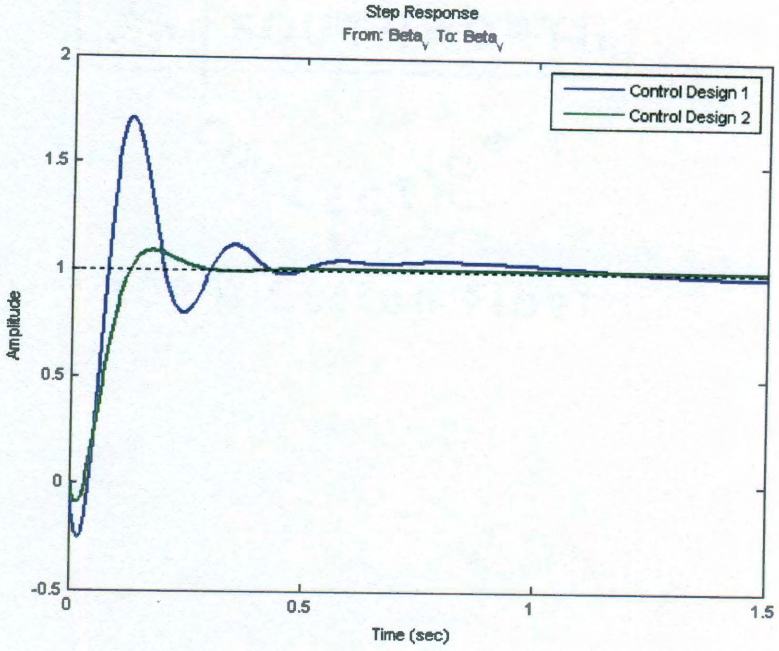

Figure 4-13: Control Design High Fidelity Trajectory Closed Loop Step Responses

The step responses of both control designs show stable controllers. Control design 1 has slightly more overshoot but slightly less settling time than control design 1. The complete frequency domain analysis shows that control design 2 provides stability and adequate margin for the vehicle throughout the entire flight profile and control design 1 although able to follow the trajectory does not provide adequate stability at all points of the trajectory because of the variation in gain with time.

4.3 Lunar Descent Trajectory

The final comparison of the control designs is to test them in a realistic application for the gimbaled engine lander. Since the mission of a vehicle of this type would most likely be as a planetary lander, the final trajectory design simulates landing on the moon. The vehicle begins 5 km above the desired landing site and 2 km up-range simulating the

vehicle having previously deorbited and entering its terminal descent phase. The vehicle then flies 2 km downrange in the Y direction and descends to an altitude of 50 meters above the landing site. The trajectory then simulates detecting an obstacle, for example a field of boulders, and immediately translates 100 meters in the Z direction in under 20 seconds to avoid the obstacle, descends and lands. A visualization of this scenario is shown in Figure 4-14: Visualization of Lunar Descent Trajectory Figure 4-14.

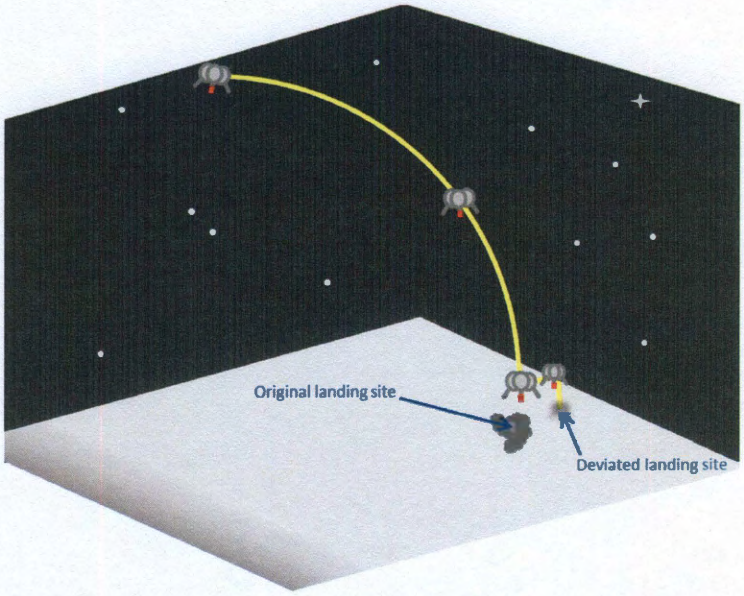

Figure 4-14: Visualization of Lunar Descent Trajectory

4.3.1 Control Gain Selection

Optimal control designs were developed using the methods described in Chapter 3. The control gains were optimized for the flight profile of the lunar descent trajectory. The control gains are designed to be optimal at a point halfway through the translation

phase of the trajectory. By designing to the midway point of the translation the mass properties and thrust profile of the vehicle are approximated as the average mass properties for the translation allowing the control design to be optimal for the average vehicle state since the control gains are fixed. The gains were designed using the frequency domain simulation attempting to maximize stability margins while minimizing rise time and settling time in the time domain. The optimal gains for the lunar descent trajectory are shown below in Table 4-7.

Table 4-7: Optimal Control Gains for Lunar Descent Trajectory

	ω_{rot} (Hz)	ζ_{rot}	ω_{trans} (Hz)	ζ_{trans}	ω_{Thrust} (Hz)	ζ_{Thrust}
Control Design 1	0.4518	1.1174	N/A	N/A	N/A	N/A
Control Design 2	0.4372	0.9785	0.0465	0.6996	0.5000	1.0000

The control gains are found from the frequency and damping using the same relationship as equation (4.1). The gains are scaled using the same gain scaling as in the jump trajectory (4.2). These control designs show the decrease in the rotational control gains as the optimal design is trying to maximize the controller's stability in order to fly the desired trajectory.

4.3.2 Lunar Descent Trajectory Performance Results

The simulation is run for a constant time of 361.5 seconds. Since this trajectory simulates a lunar descent, the vehicle is flown with gravity that varies with vehicle altitude. The variable lunar gravity allows the vehicle to run considerably longer than the previous simulations since less thrust is needed and fuel is conserved. The controller is run at 25 Hz and the guidance is run at 2 Hz. The trajectory is flown without any

disturbances in order to understand the behavior of the control designs in the most ideal of cases. The flown position trajectory is plotted with the commanded position trajectory for each of the control designs. The results are shown in Figure 4-15 and Figure 4-16.

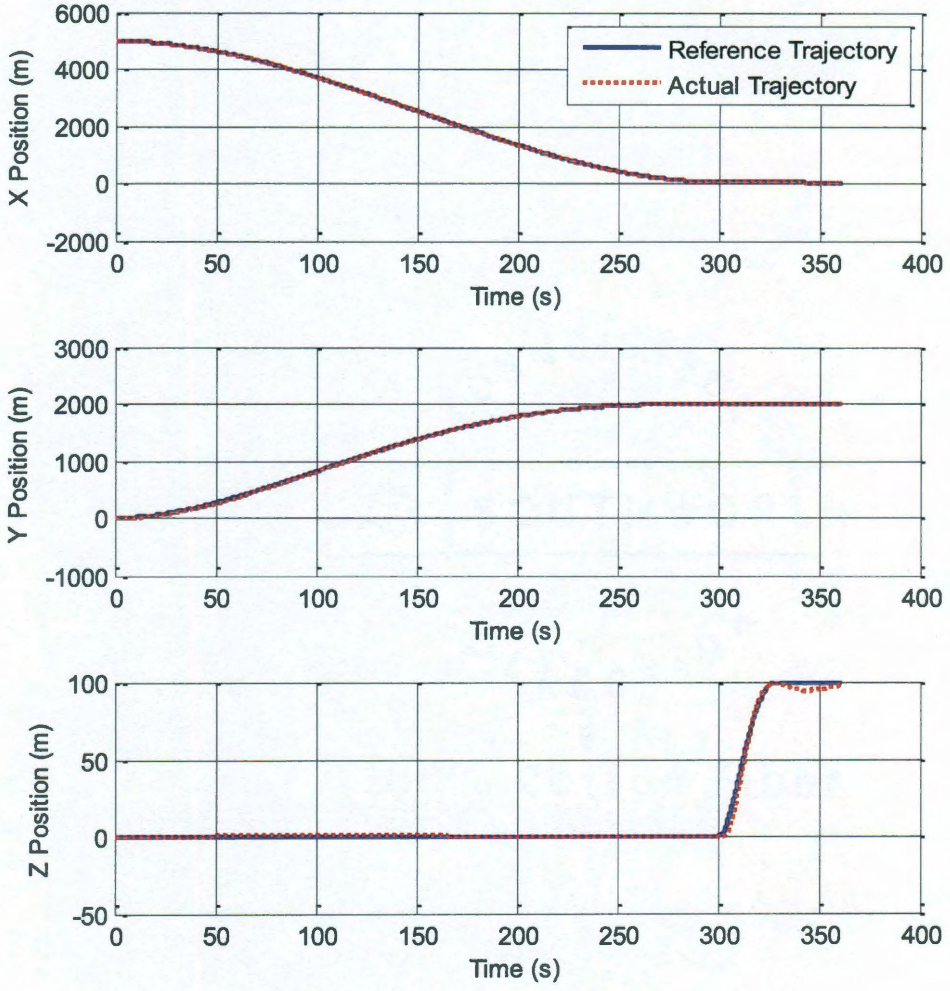

Figure 4-15: Control Design 1 Position Compared with Reference Lunar Descent Trajectory

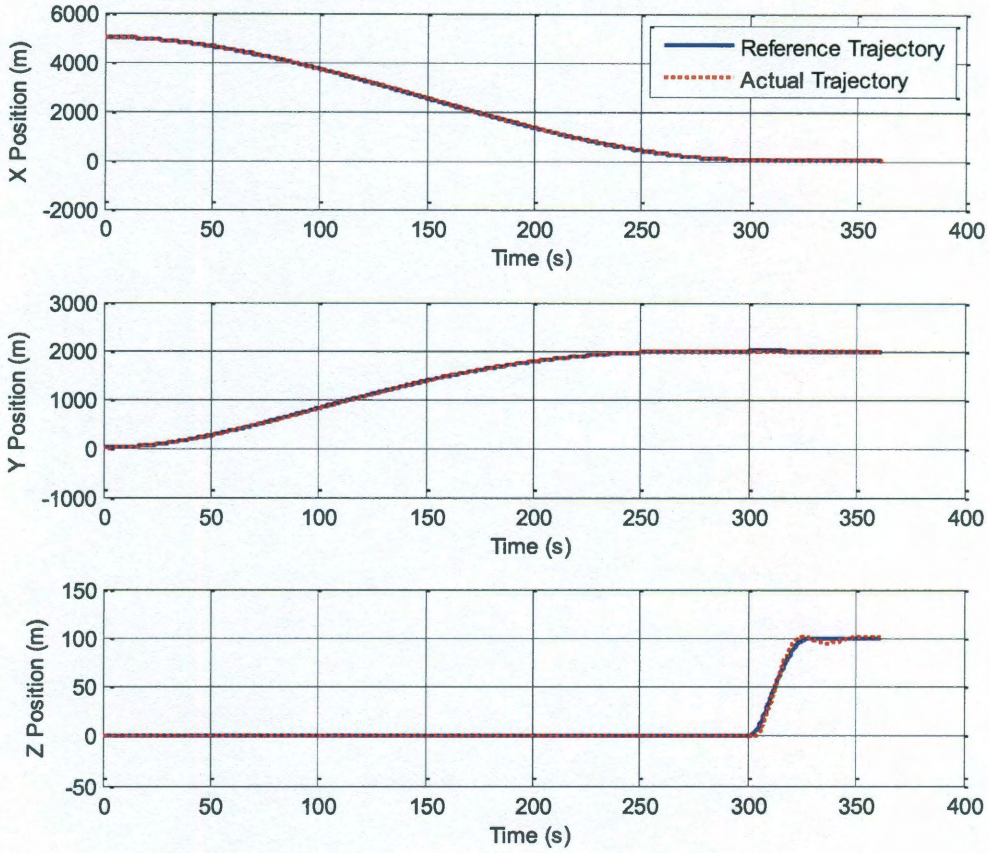

Figure 4-16: Control Design 2 Position Compared with Reference Lunar Descent Trajectory

The position results show that control design 1 follows the commanded position trajectory almost identically to control design 2. The only significant error in either trajectory appears to be the slight oscillations seen in both designs during the abrupt Z direction translation at the end of the flight. In order to examine the error in more detail plots showing the position error of each control design with respect to the commanded position are shown in Figure 4-17:

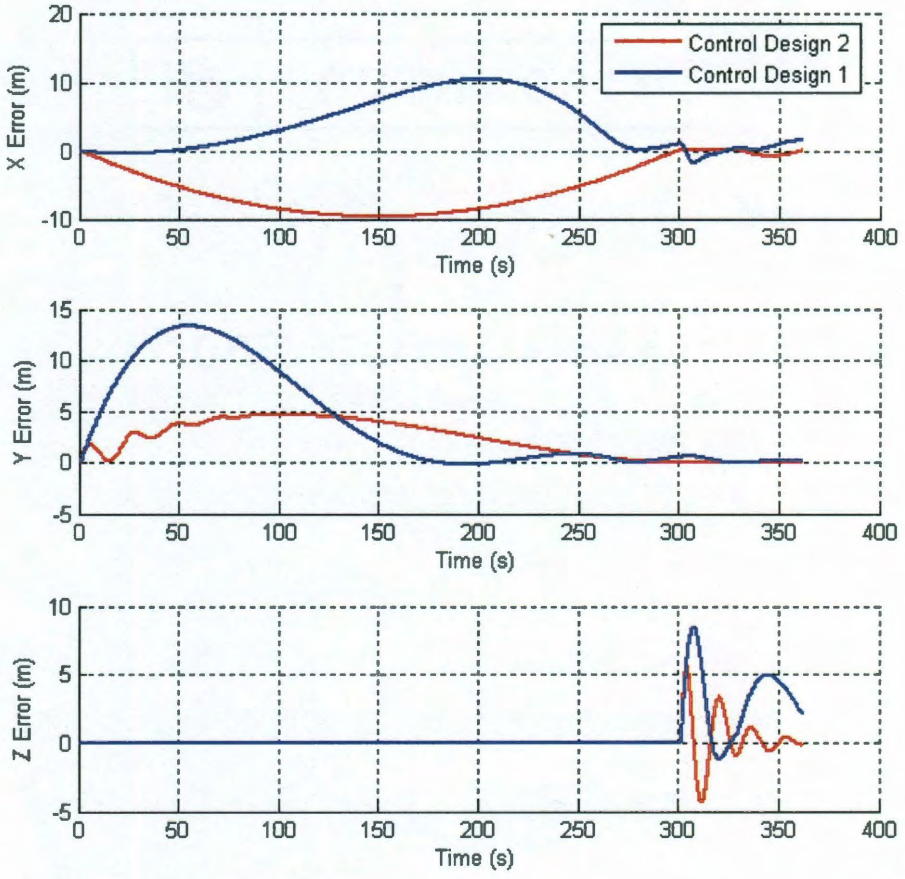

Figure 4-17: Lunar Descent Trajectory Position Error

The position error plots show that both designs have position error on a similar order of magnitude. Although control design 2 appears to have higher vertical position error, the translational error appears slightly smaller than control design 1. Control design 2 shows no significant error at the terminal state and arrives at the deviated landing site properly where as control design 1 shows an error of approximately 2 meters at the terminal state.

In order to understand the full behavior of the vehicle it is important to analyze the rotation of the vehicle in addition to the translation. The rotational angles of the vehicle for each of the control designs are shown below in Figure 4-18.

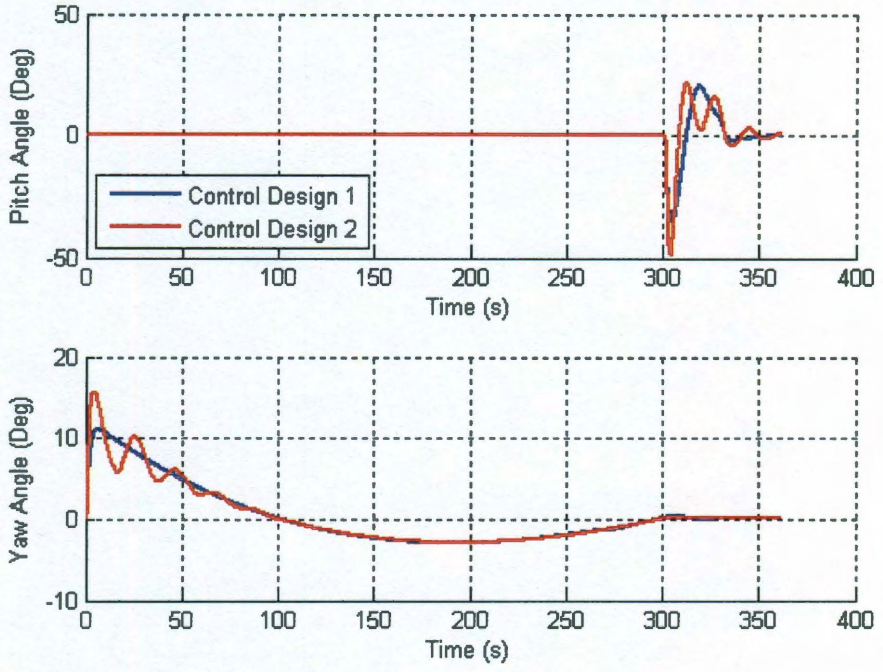

Figure 4-18: Lunar Descent Trajectory Rotation Angle Performance

The rotational angles of the vehicle show that both designs result in nearly identical rotational behavior of the vehicle. Rotation of the vehicle creates lateral acceleration of the propellant. A general summary of the performance results for the lunar descent trajectory are shown below in Table 4-8.

Table 4-8: Summary of Lunar Descent Trajectory Performance Results

	Maximum Vertical Position Error (m)	Average Vertical Position Error (m)	Maximum Horizontal Position Error (m)	Average Horizontal Position Error (m)	Maximum Vehicle Pitch/Yaw Angle (degrees)	Maximum Engine Gimbal Angle (degrees)
Control Design 1	10.4247	3.7825	13.3119	10.8836	34.8651	20.00
Control Design 2	9.6717	5.3309	7.5084	1.3899	37.2820	20.00

Control design 1 had less average vertical position error than control design 2 however the maximum and average horizontal position errors were larger. Control design 1 had a maximum angle of rotation that was slightly less than control design 2 as well. Both control designs saturated the gimbal control at least once however control design 2 flew the trajectory with slightly less error on average than control design 1. In a trajectory that requires 5 km of vertical movement and 2 km of translation the largest translational error seen by control design 2 was just over 7 meters and the maximum error seen by control design 1 was only 13 meters.

4.3.3 Lunar Descent Trajectory Stability Results

The stability of the vehicle is absolutely critical to the analysis of the control designs, particularly for the lunar descent trajectory. This is because the lunar descent trajectory most accurately models a realistic application of the vehicle and control designs. A loss of stability due to unforeseen perturbations or delays could cause the vehicle to crash during its critical phases of flight. It is important that the control design for this trajectory have the largest margins since the stability is critical to the survival of the vehicle. The vehicle must have a minimum of 6 dB of gain margin, 30 degrees of phase margin, and 0.05 seconds of delay margin. The frequency domain simulation is

used to generate stability margins throughout the flight profile. The results of the stability analysis are shown below in Table 4-9.

Table 4-9: Summary of Lunar Descent Trajectory Stability Results

	Maximum Positive Gain Margin (dB)	Minimum Positive Gain Margin (dB)	Maximum Positive Phase Margin (deg)	Minimum Positive Phase Margin (deg)	Maximum Positive Delay Margin (sec)	Minimum Positive Delay Margin (sec)
Control Design 1 Y-axis	10.72	0.23	116.94	1.03	0.27	0.001
Control Design 1 Z-axis	10.45	0.31	114.30	1.50	0.27	0.001
Control Design 2 Y-axis	13.33	13.08	58.76	56.93	0.08	0.08
Control Design 2 Z-axis	13.72	13.52	59.63	57.89	0.09	0.09

Control design 2 has significant stability margin to fly the lunar descent trajectory under less than ideal conditions. Control design 1 again has points where the margins are reduced beyond acceptable levels as the gains are increased significantly as the vehicle approaches the end of a stage. In order to properly visualize the response of the controllers step response plots were created to give an approximate view of the controller's response to a reference step command. The resulting step response plots for the control designs at the end of the trajectory are shown below in Figure 4-19.

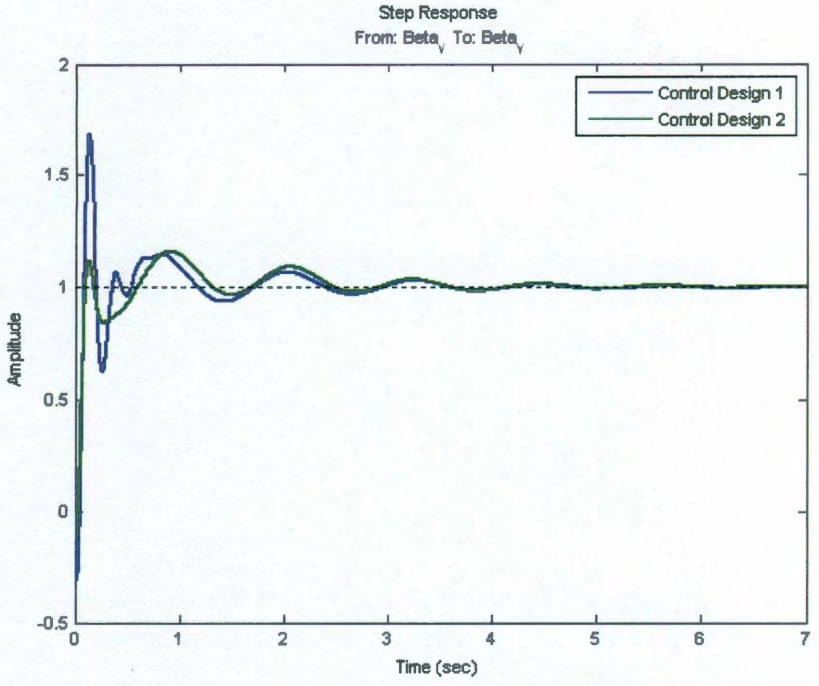

Figure 4-19: Control Design 1 Lunar Descent Trajectory Closed Loop and Step Response

The step response of both systems shows that there is significant overshoot but the controllers are able to fly the trajectory. The frequency domain analysis verifies the stability of control design 2 and that it provides adequate margin for the lunar descent trajectory. Although control design 1 does not always have adequate margin it is still able to fly the trajectory.

4.4 Monte Carlo Analysis

In order to verify the robustness of each of the control designs it is necessary to test them under less than ideal conditions. For this reason, a Monte Carlo simulation was developed to test the control designs with errors in all aspects of the controller's knowledge. The Monte Carlo simulation is a powerful tool that can be used to gather statistical data through simulation [24].

4.4.1 State and Vehicle Parameter Error Simulation

To analyze the statistical ability of the control designs to handle disturbance, all sensed data from the environment that the controller uses to determine the appropriate control command was given random error. This includes the state information such as sensed position, velocity, rotation, and angular rate as well as mass property estimates used to scale the control gains such as vehicle mass, inertia, and center of mass location.

Table 4-10: Summary of Monte Carlo Parameter Variation

	Normally Distributed Error Value	**Uniformly Distributed Error Value**
Inertial Position	Nominal Value +/- 5%	Nominal Value +/- 5%
Inertial Velocity	Nominal Value +/- 5%	Nominal Value +/- 5%
Body Quaternion	Nominal Value +/- 5%	Nominal Value +/- 5%
Body Angular Rate	Nominal Value +/- 5%	Nominal Value +/- 5%
Total Vehicle Mass	Nominal Value +/- 5%	Nominal Value +/- 5%
Total Vehicle Inertia	Nominal Value +/- 5%	Nominal Value +/- 5%
Vehicle Composite Center of Mass	Nominal Value +/- 5%	Nominal Value +/- 5%

Each signal was multiplied by an individual random error with an individual random seed number. The error was first assumed to be normally distributed with a mean of zero and assumed to be no greater than 5%; statistically this meant that 5% error represented three standard deviations from the mean error of zero. The normal distribution is a reasonable assumption for error because the central limit theorem states that a large number of individual estimates each having its own independent errors will

create a normal distribution [25]. The jump trajectory and the respective jump trajectory control designs were used to test the control designs with the errors described above. The simulations were run 1000 times for each control design with random seed numbers being generated for each iteration. The resulting position plots for the respective control designs are shown in Figure 4-20 and Figure 4-21.

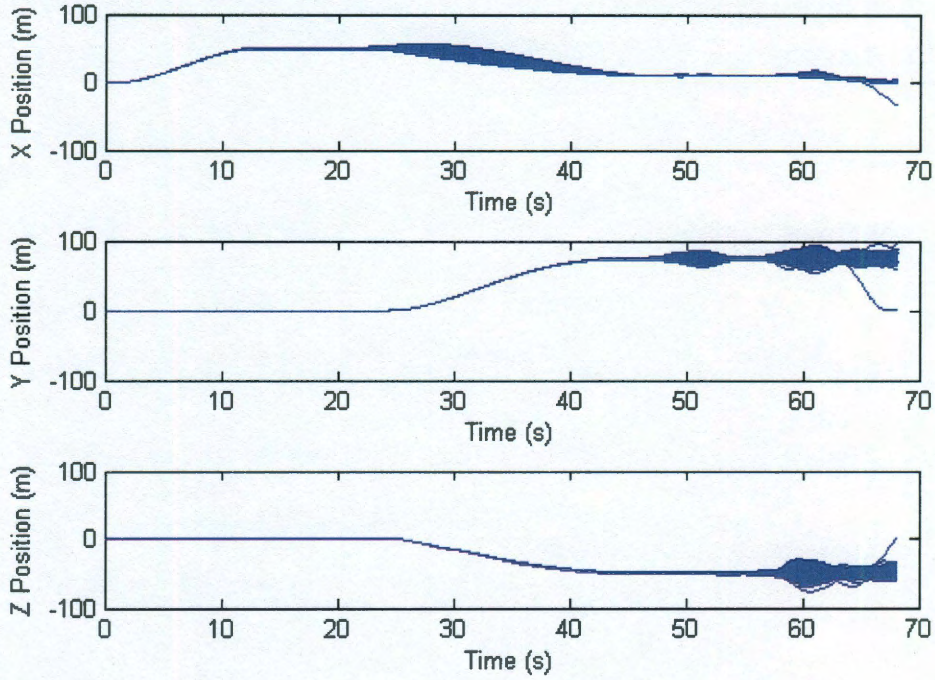

Figure 4-20: Control Design 1 Position Jump Trajectory Normally Distributed Error Monte Carlo for n=1000 Samples

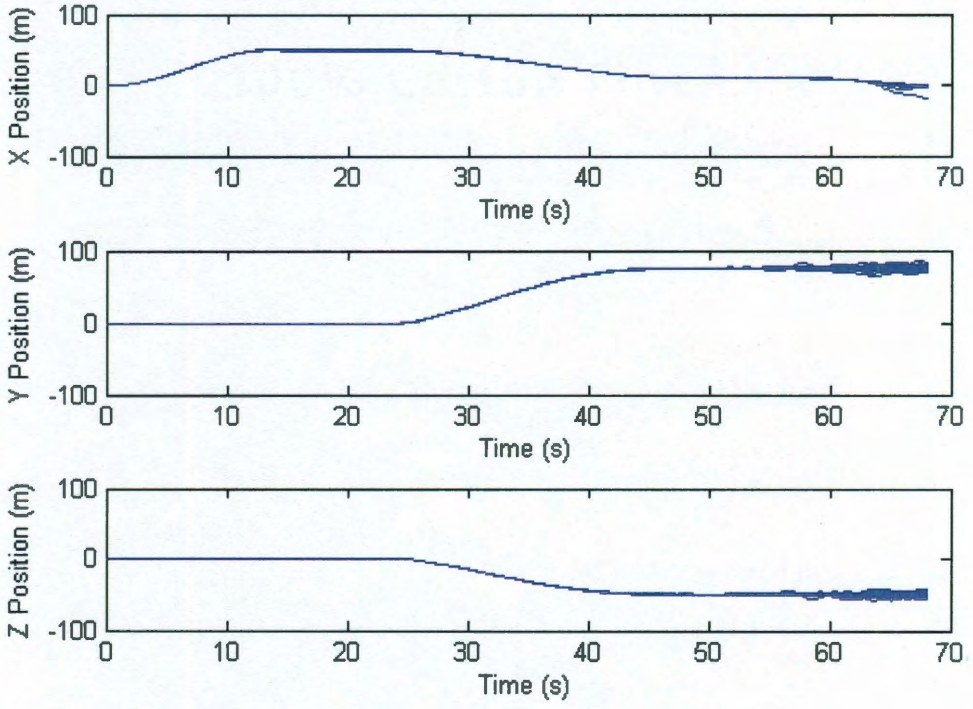

Figure 4-21: Control Design 2 Position Jump Trajectory Normally Distributed Error Monte Carlo for n=1000 Samples

These results show that control designs 1 and 2 both were stable and able to fly the trajectory under less than ideal conditions. Control design 1 showed significantly larger variation in the position plots, particularly during the terminal phase. Additionally, points of large variation can be seen in control design 1 where the vehicle is approaching the end of a stage and the guidance control gains are becoming very large. This is a disadvantage of the legacy architecture. Control design 2 was in general better able to handle perturbations than control design 1 which can be seen in a plot of the normalized position error shown in Figure 4-22.

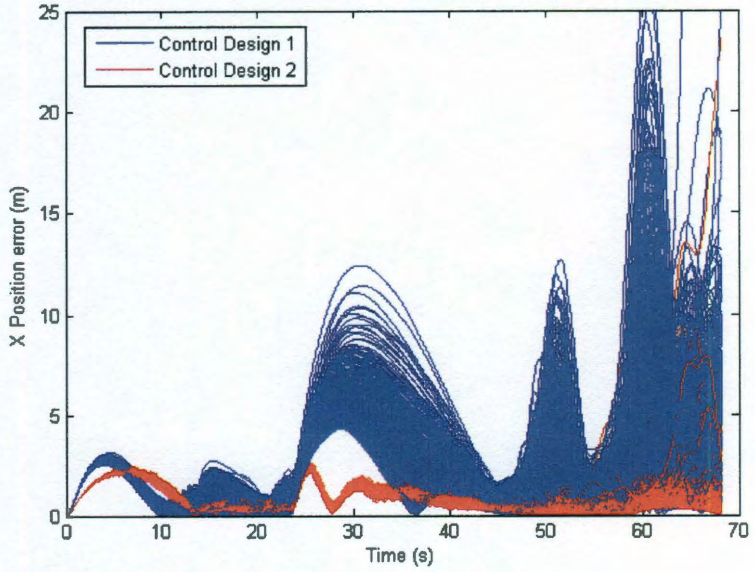

Figure 4-22: Normalized Position Error for Normally Distributed Error Monte Carlo for n=1000 Samples

In order to be thorough in the analysis of each control design a similar simulation was setup assuming that the error was uniformly distributed and not normally distributed. This assumption should result in generally larger average errors because for a uniform distribution the probability of a larger magnitude error occurring is now equal to the probability of a smaller error occurring [26]. The error was assumed to be uniformly distributed between -5% and 5%. A Monte Carlo simulation was run 1000 times using the jump trajectory simulation and control designs. The resulting position plots of all Samples are shown in Figure 4-23 and Figure 4-24.

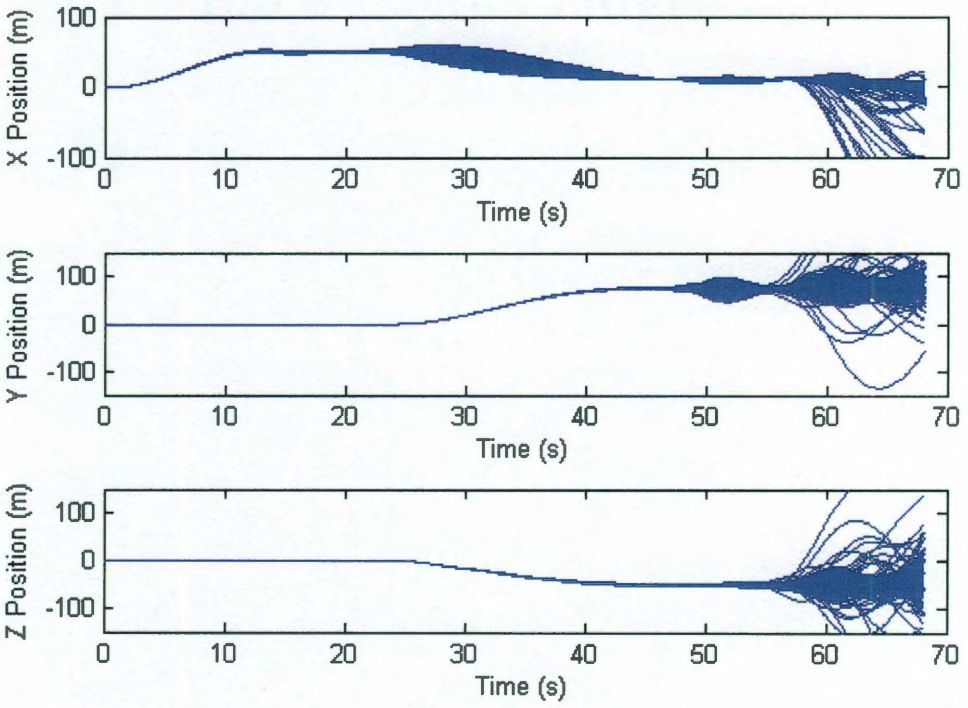

Figure 4-23: Control Design 1 Position Jump Trajectory Uniformly Distributed Error Monte Carlo for n=1000 Samples

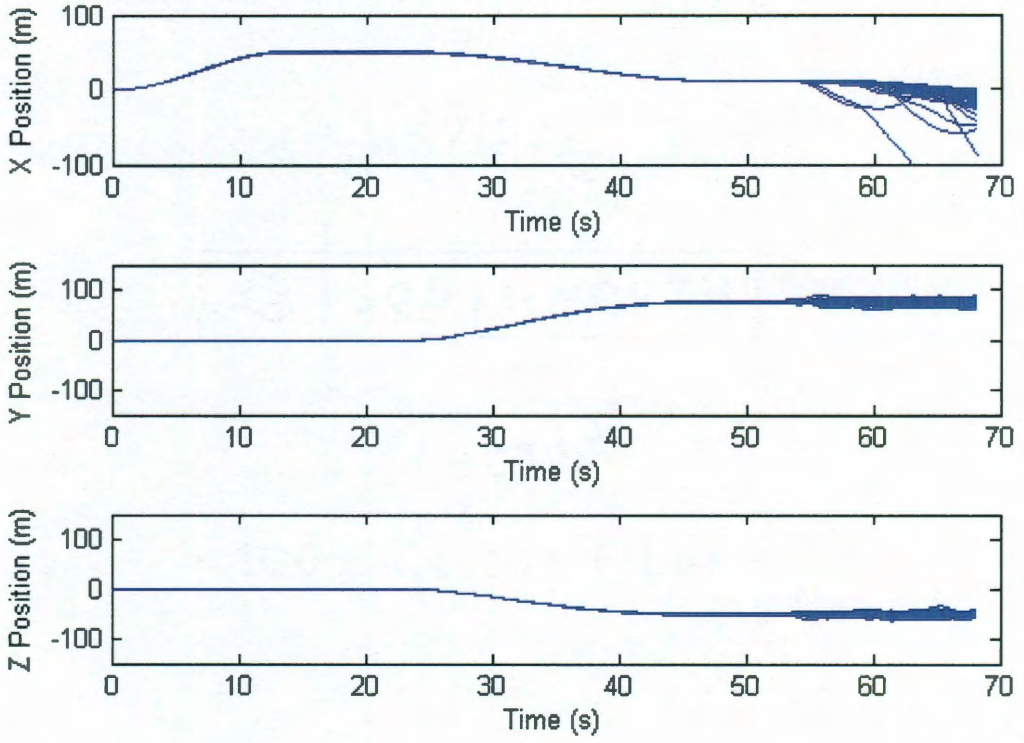

Figure 4-24: Control Design 2 Position Jump Trajectory Uniformly Distributed Error Monte Carlo for n=1000 Samples

These results show that control design 2 was generally better able to handle the perturbations in the system. This can be seen because of the significantly smaller variation in position plots between control design 2 and control design 1. Large deviations in position can also be seen at the end of each stage of flight in control design 1 which is again caused by the large guidance correction gains in the legacy architecture design. The normalized position error for the two designs is shown in Figure 4-25.

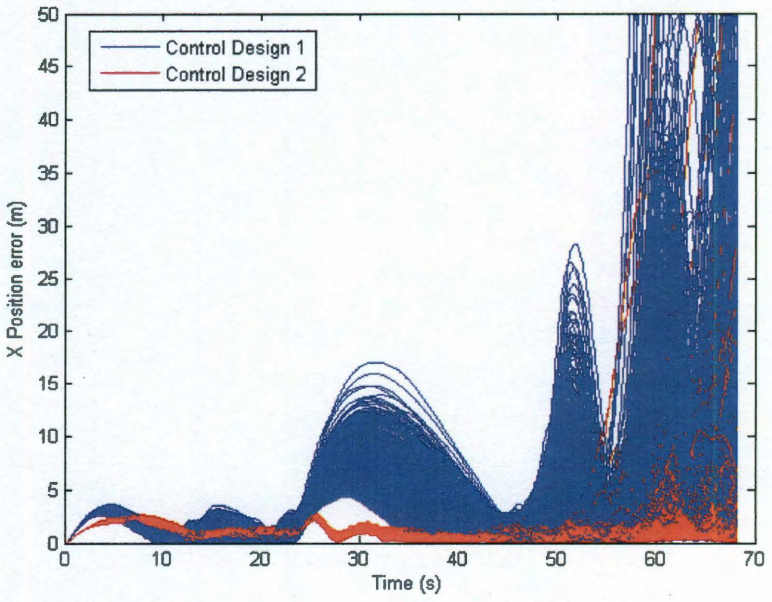

Figure 4-25: Normalized Position Error for Uniformly Distributed Error Monte Carlo for n=1000 Samples

A summary of the Monte Carlo simulation results for the distributions of position and velocity error relative to the commanded trajectory are shown in Table 4-11 and Table 4-12.

Table 4-11: Summary of Monte Carlo Position Results

	Mean Maximum X Position Error Magnitude (m)	Maximum X Position Error Standard Deviation (m)	Mean Maximum Y Position Error Magnitude (m)	Maximum Y Position Error Standard Deviation (m)	Mean Maximum Z Position Error Magnitude (m)	Maximum Z Position Error Standard Deviation (m)
Control Design 1 Normally Distributed Error	3.7585	1.7661	7.3182	3.4966	6.4472	3.2028
Control Design 2 Normally Distributed Error	2.2846	0.6210	2.2416	0.8315	1.4025	0.8688
Control Design 1 Uniformly Distributed Error	8.9397	23.3216	17.1968	27.1634	17.0334	26.4830
Control Design 2 Uniformly Distributed Error	3.3250	8.3007	3.4218	2.3026	2.6941	2.2239

Table 4-12: Summary of Monte Carlo Velocity Results

	Mean Maximum X Velocity Error Magnitude (m/s)	Maximum X Velocity Error Standard Deviation (m/s)	Mean Maximum Y Velocity Error Magnitude (m/s)	Maximum Y Velocity Error Standard Deviation (m/s)	Mean Maximum Z Velocity Error Magnitude (m/s)	Maximum Z Velocity Error Standard Deviation (m/s)
Control Design 1 Normally Distributed Error	1.7205	0.6724	6.2874	2.2549	5.8082	2.0727
Control Design 2 Normally Distributed Error	0.9830	0.2918	1.8999	1.2202	1.4855	1.3200
Control Design 1 Uniformly Distributed Error	3.8173	3.9499	11.7839	6.6318	10.9743	6.9915
Control Design 2 Uniformly Distributed Error	1.6060	1.8061	3.6181	2.9925	3.4384	2.8749

This verifies that not only did control design 2 have less maximum error in position and velocity for both distributions but the error of control design 2 also varied significantly less than control design 1. This can be seen from the much larger standard deviations of control design 1's error. As a general result control design 2 provides greater performance and robustness in its ability to handle perturbations to the system.

4.4.2 Throttle Error Simulation

Accurately modeling the response of a rocket engine is a difficult and expensive task. Up to this point the results of this thesis have assumed ideal thrust and performance from the engine. In a real environment there are always perturbations of the rocket engine's performance that will affect the throttle response. A comparison of the performance of each control design with less than ideal throttle response must be

performed in order to fully compare the designs. To realistically simulate the error in a rocket engine three main errors are applied to the system. The first error is a constant bias term that is less than the ideal throttle response. This simulates the engine underperforming by a constant amount. In real life this underperformance could be caused by things such as tank pressure differences or inaccuracies in the engine model. The next error is uniformly distributed random error. This error essentially allows for random variation in the throttle with time. This error models dynamic random perturbations to the system that could be caused by such things as changing chamber pressure, temperature and pressure variation, or varying propellant flow rate. The final error is a sinusoidal error on the throttle response. This error simulates the cyclical variation of rocket engine performance that is observed over time [27]. The visual representation of each of these errors can be seen in Figure 4-26.

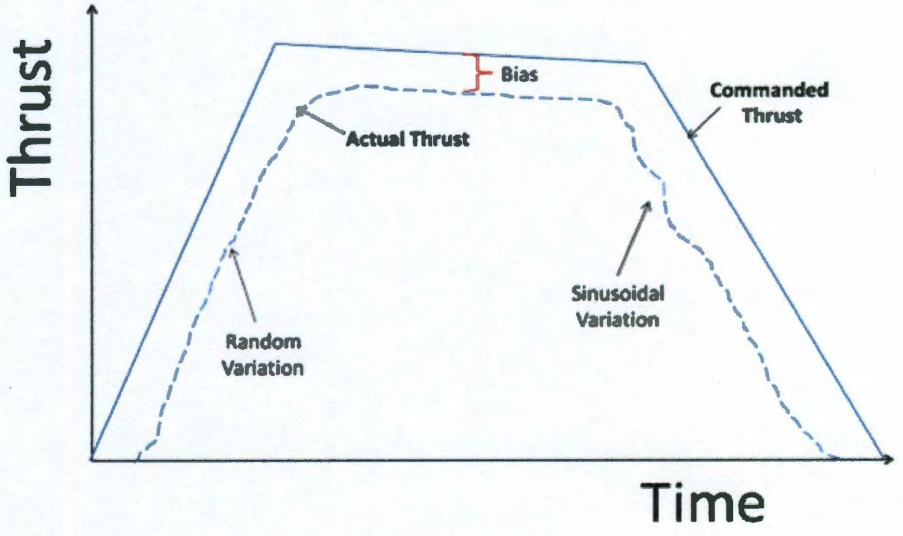

Figure 4-26: Thrust Error Model

The simulated thrust on the vehicle is represented in equation (4.3) as the summation of these three errors

$$\hat{T} = T + T\left(-K_{bias}\left(1 + \gamma\frac{t}{t_{final}}\right) + K_{rand} + K_{sin}\sin(\omega t)\right), \quad (4.3)$$

where

$\hat{T}$- Actual thrust

T- Commanded thrust

K_{bias}- Random bias gain

K_{rand}- Random error gain

K_{sin}- Sinusoidal error gain

γ- Time delay scaling factor

ω- Sinusoidal error frequency

t- Time

t_{final}- Engine cutoff time.

To properly simulate the engine behavior a Monte Carlo simulation is used to run the simulation 1000 times and record the error in the vehicle response. The variation of the throttle error model parameters used in the simulation can be seen in Table 4-13.

Table 4-13: Summary of Thrust Error Monte Carlo Parameter Variation

	Error	**Range**
Throttle Bias	$-K_{bias}\left(1+\gamma\frac{t}{t_{final}}\right)T$	$K_{bias} = 0.03$ $\gamma = 1$
Random Noise	$K_{rand}T$	K_{rand}= +/- 0.03
Sinusoidal Error	$K_{sin}\sin(\omega t)\,T$	$K_{sin} = 0.03$ $\omega = 10\,Hz$

The simulation was run 1000 times and the resulting position responses for each control design are plotted in Figure 4-27 and Figure 4-28.

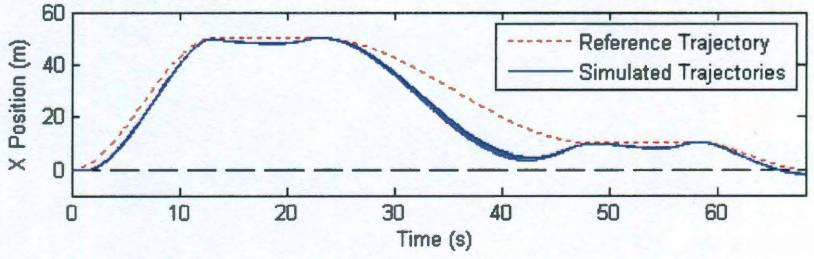

Figure 4-27: Control Design 1 X Position with Uniformly Distributed Thrust Error Monte Carlo for n=1000 Samples

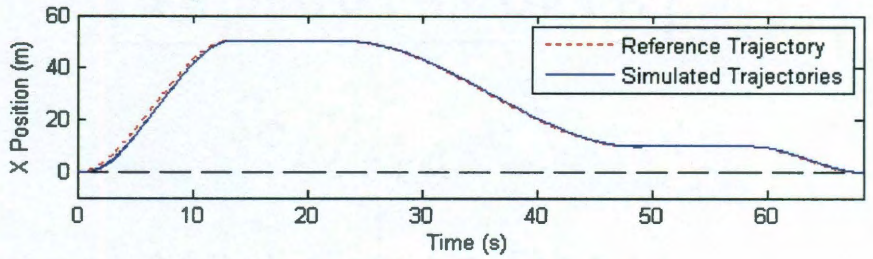

Figure 4-28: Control Design 2 X Position with Uniformly Distributed Thrust Error Monte Carlo for n=1000 Samples

These position plots show that control design 1 has significant variation in its position when it experiences throttle error. The variation is the largest in the X direction which represents the vehicles altitude. The error in the vertical position of control design 1 almost causes it to penetrate the ground represented by a line drawn at 0 meters at approximately 40 seconds into the flight. At the terminal state the vehicle actual goes "below ground" since no ground model is present in the dynamics. This could cause significant damage to the vehicle in real life and is a large flaw of the first control design. Control design 2 shows minimal variation in its response and does not penetrate the ground during any of the simulations. The position error experienced by both control designs is shown in Figure 4-29.

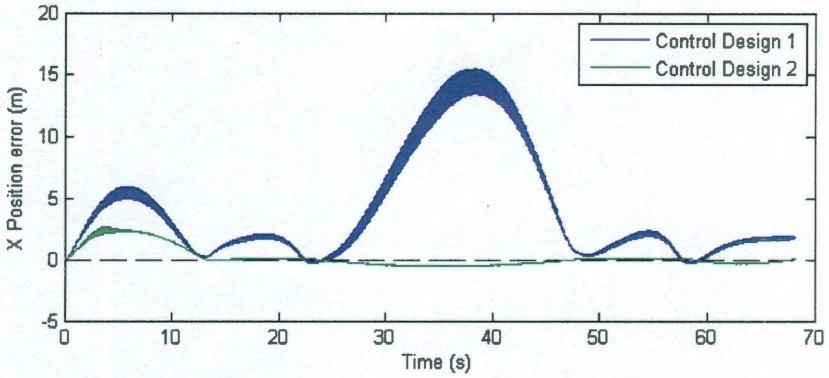

Figure 4-29: Position Trajectory Error for Uniformly Distributed Thrust Error Monte Carlo for n=1000 Samples

Significantly greater error is visible in the simulations of control design 1 as was expected. The distribution of the error in control design 1 is also more spread out than that of control design 2. These results show a large advantage of control design 2. Control design 1 would require extremely accurate modeling of the engine performance in order to accurately fly the trajectory. This modeling is extremely expensive and time intensive. Additionally, the flight profile would need to be "pre-planned" to account for the modeled response of the rocket engine. It is important to also note that the position error is largest at the beginning of each guidance stage. Because the correction gains are significantly small initially, the throttle cannot correct for error fast enough. As the end of the vehicle approaches the end of the stage these gains become higher and error is reduced. This can be seen in Figure 4-30.

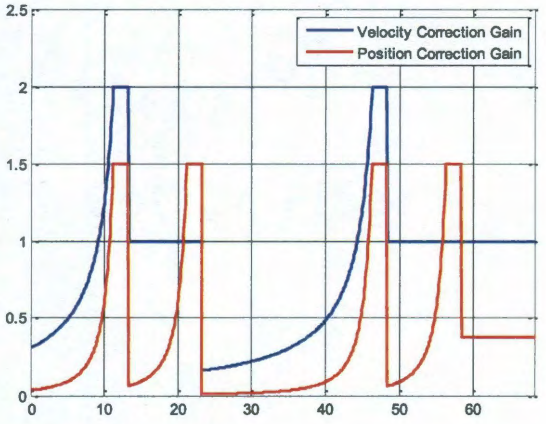

Figure 4-30: Control Design 1 Correction Gains for Throttle Error Simulation

It is not advantageous to further increase the guidance correction gains in control design 1 to achieve better performance because further increase will further reduce stability. The performance of control design 2 is almost unaffected by variation and error in the throttle. Control design 2 does not need any significant modeling of the engine behavior to fly the trajectory. The robustness to throttle error seen in control design 2 is a natural benefit of its design where the throttle is commanded through vertical position and velocity and not through a predetermined acceleration command.

4.5 Filter Performance

The real world environment that the vehicle will face is never ideal. Perturbations from the environment, sensor error, and delays in the system are just a few of the real world factors that hinder the stability and performance of the vehicle. In order to enhance the vehicles robustness to maintain stability and increase performance a filter is added to the control design. Filters can be used to reduce the effects of specific frequency ranges while at the same time magnifying the effects of other frequencies [28]. Applied to the

GNC system, the filter is able to increase stability margins by attenuating noise and reducing the effects of uncontrollable modes of the open loop system. Since most noise has a higher frequency than the actual signal a lowpass filter is desirable for application to this vehicles control designs. An ideal lowpass filter provides 0 dB of amplification for low frequencies and after a specified cutoff frequency the filter de-amplifies the signal to attenuate the effects of higher frequency signals. Another way of viewing this is that an ideal lowpass filter amplifies higher frequencies by a negative magnitude dB and amplifies low frequencies by 0 db or a magnitude of 1 [29]. An example of the amplification of a lowpass filter over a range of frequencies is shown below:

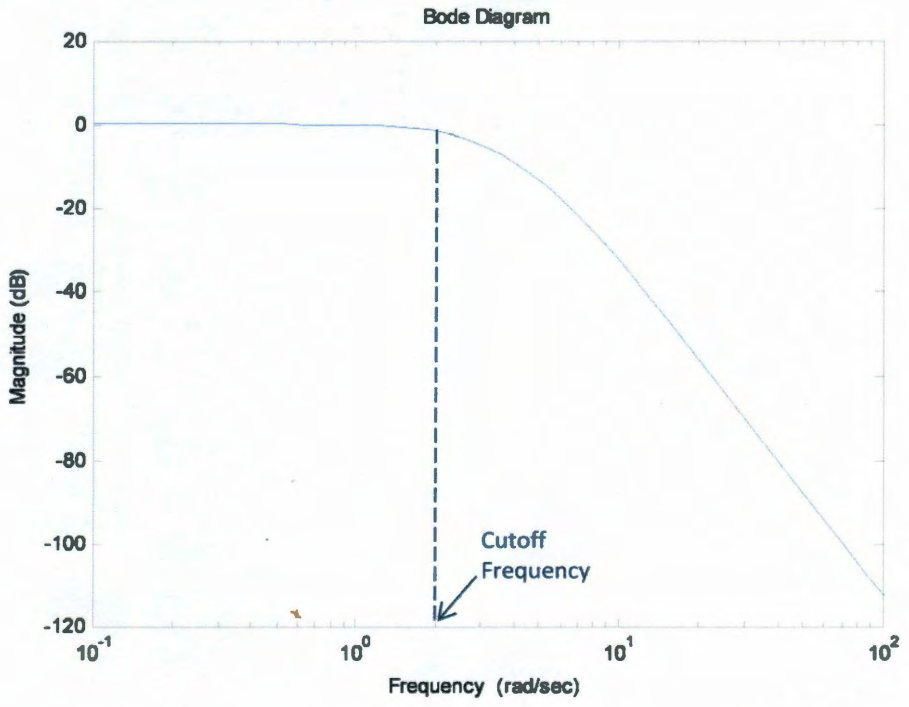

Figure 4-31: Lowpass Filter Magnitude Response

4.5.1 Filter Design Stability

In order to attenuate the effects of slosh and limit excessive gimbal chatter caused by noise it is essential to design filters for the control designs. Filters are optimally designed to reduce gimbal chatter and slosh and also improve stability using the methods described in Chapter 3. The lunar design trajectory is chosen to demonstrate the effects of an optimal filter design on both stability and performance. An optimal filter is designed for the lunar descent trajectory for a point 200 seconds into the trajectory. The optimal lowpass filter is given by the transfer function

$$system\_filter = \frac{0.1473s^4+3.564s^3+71.75s^2+263.4s+3440}{s^4+25.47s^3+272.8s^2+1426s+3440}. \quad (4.4)$$

In order to visualize the filter's response in the frequency domain, a Bode plot of the filter is shown below in Figure 4-32.

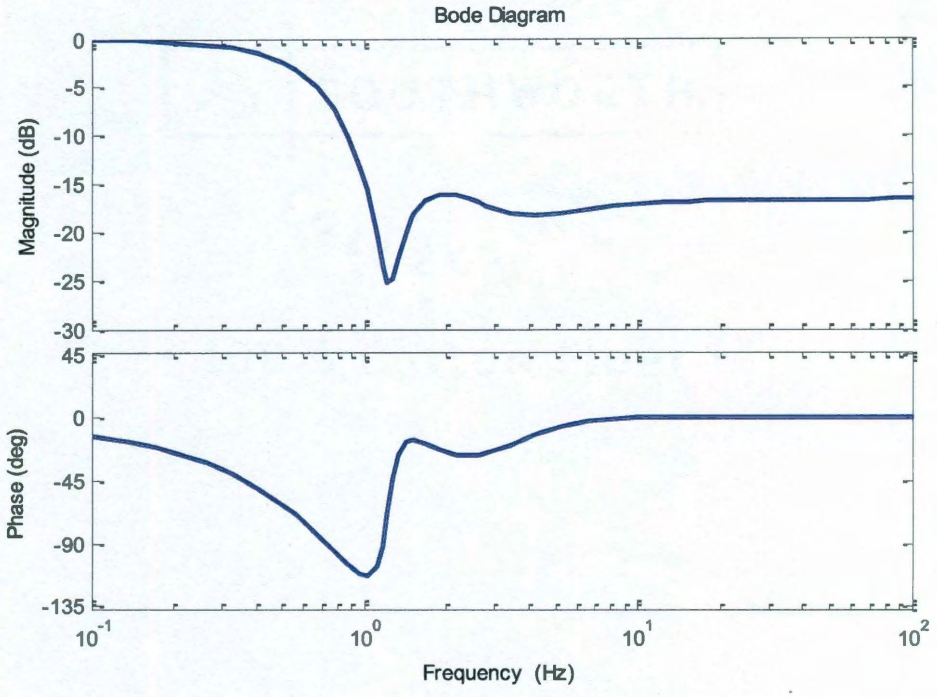

Figure 4-32: Lunar Descent Trajectory Optimal Lowpass Filter Design

The frequency response of the filter shows that after a frequency of approximately 0.1 Hz the magnitude response drops off significantly. The magnitude response also shows an attenuation of higher frequencies by at least -15 dB which will significantly reduce high-frequency chatter in the gimbal control.

4.5.2 Filtered Lunar Descent Response

To test the performance of the filter in the time domain the lunar descent trajectory simulation was run using the arbitrary fixed gains shown in Table 4-1.

Table 4-14: Fixed Control Gains for Filtered Lunar Descent Trajectory

	ω_{rot} (Hz)	ζ_{rot}	ω_{trans} (Hz)	ζ_{trans}
Control Design 1	0.15	0.75	N/A	N/A
Control Design 2	0.15	0.75	0.01	0.8

The controller gains were selected to be identical for the two control designs to compare the two control designs with the same filter and gains. The position plots of the two control designs are shown in Figure 4-33 and Figure 4-34.

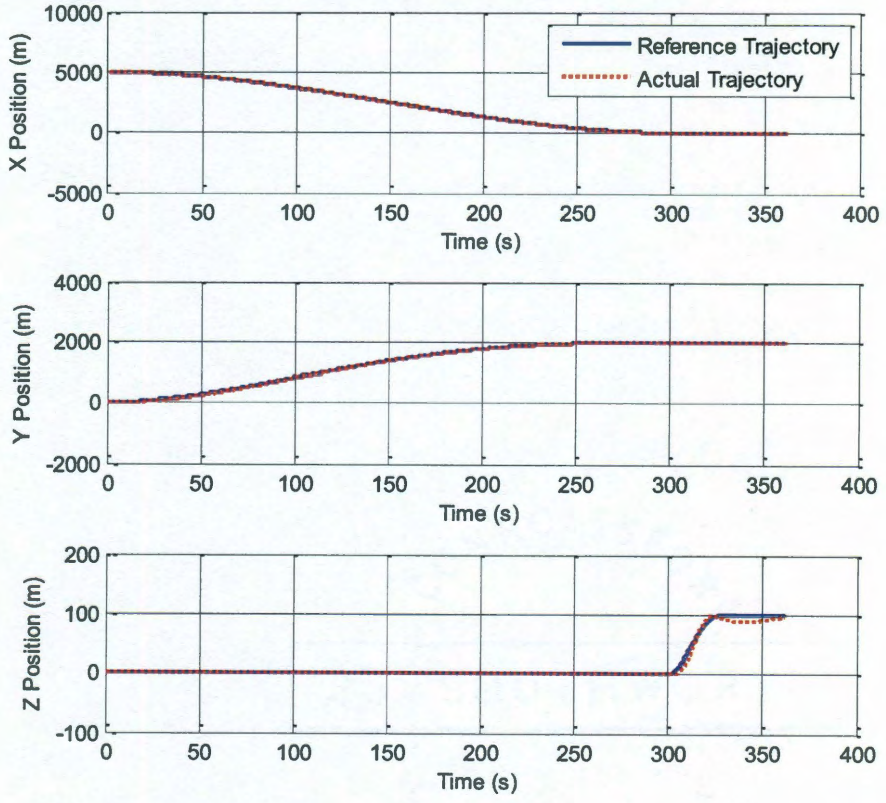

Figure 4-33: Filtered Control Design 1 Position Compared to Reference Trajectory

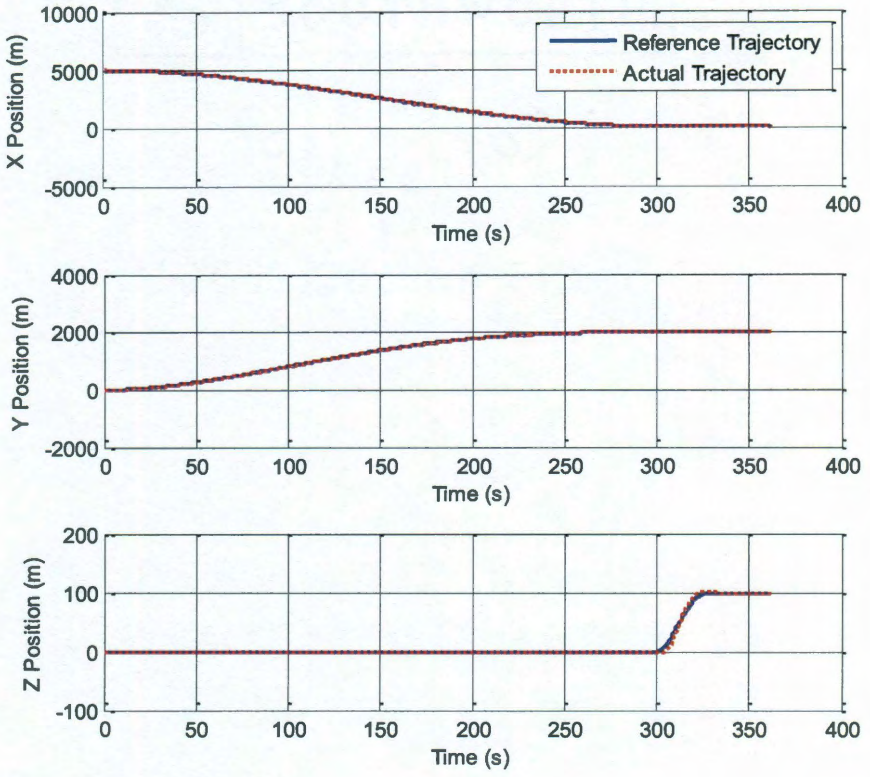

Figure 4-34: Filtered Control Design 2 Position Compared to Reference Trajectory

The control designs are both able to fly the commanded trajectory. The position plots show control design 2 more closely follows the commanded reference trajectory. To more closely examine the difference between the controllers and their ability to follow the trajectory a plot of the control design position errors with respect to the reference trajectory is shown in Figure 4-35.

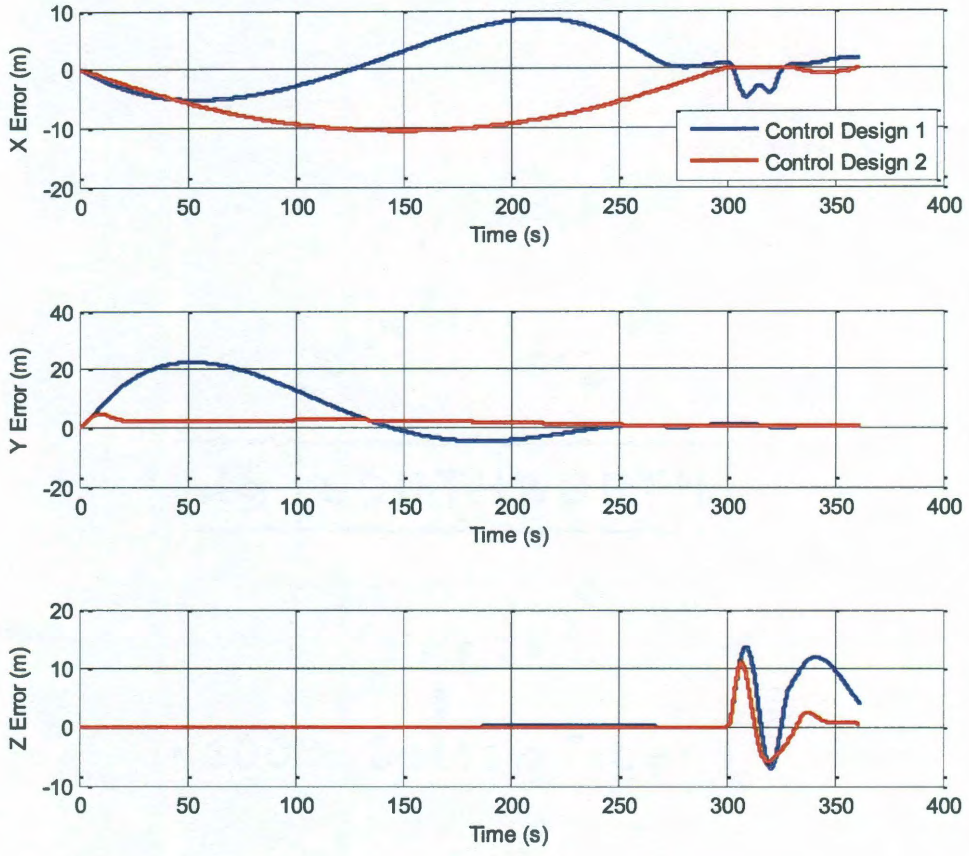

Figure 4-35: Filtered Control Design Position Error Comparison

The error plot shows the significantly reduced error of control design 2 both throughout the trajectory and in the terminal state. The capability of control design 2 to directly correct position and velocity errors allows the design to more closely follow the trajectory.

A significant benefit of the filter is the reduction in high frequency chatter of the gimbal. This has a smoothing effect on the gimbal response. The filtered gimbal engine response of control designs 1 and 2 are shown in Figure 4-36.

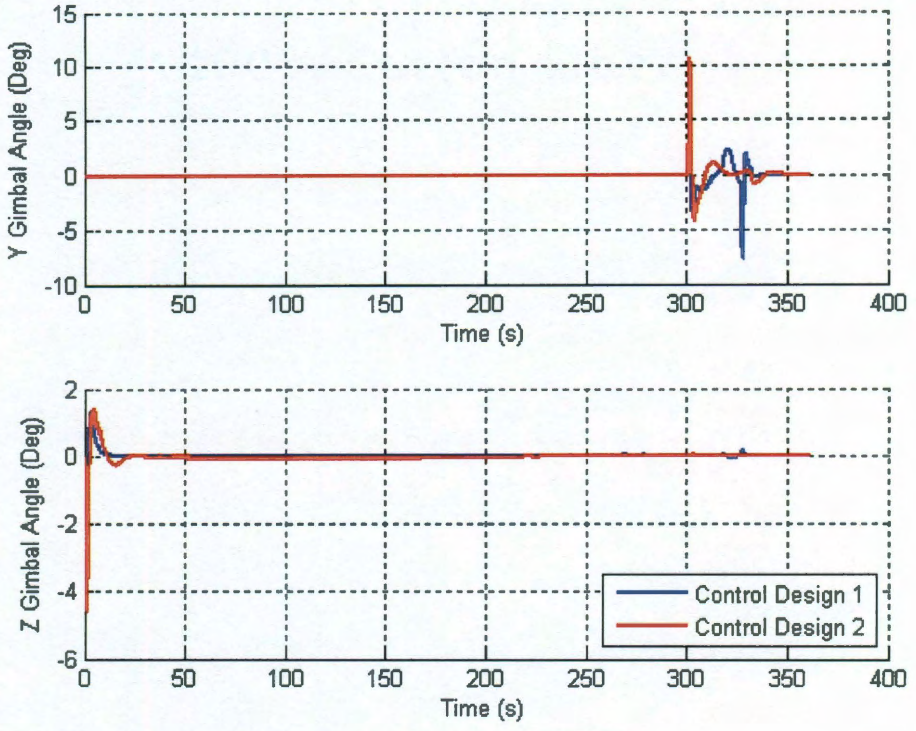

Figure 4-36: Filtered Control Design Gimbal Angles

The gimbal responses of both control designs are extremely smooth. Excess gimbal motion is greatly reduced resulting in greater efficiency and smaller overall gimbal magnitudes. The reduced gimbal chatter caused by the filter should also greatly reduce propellant slosh motion as seen in Figure 4-37.

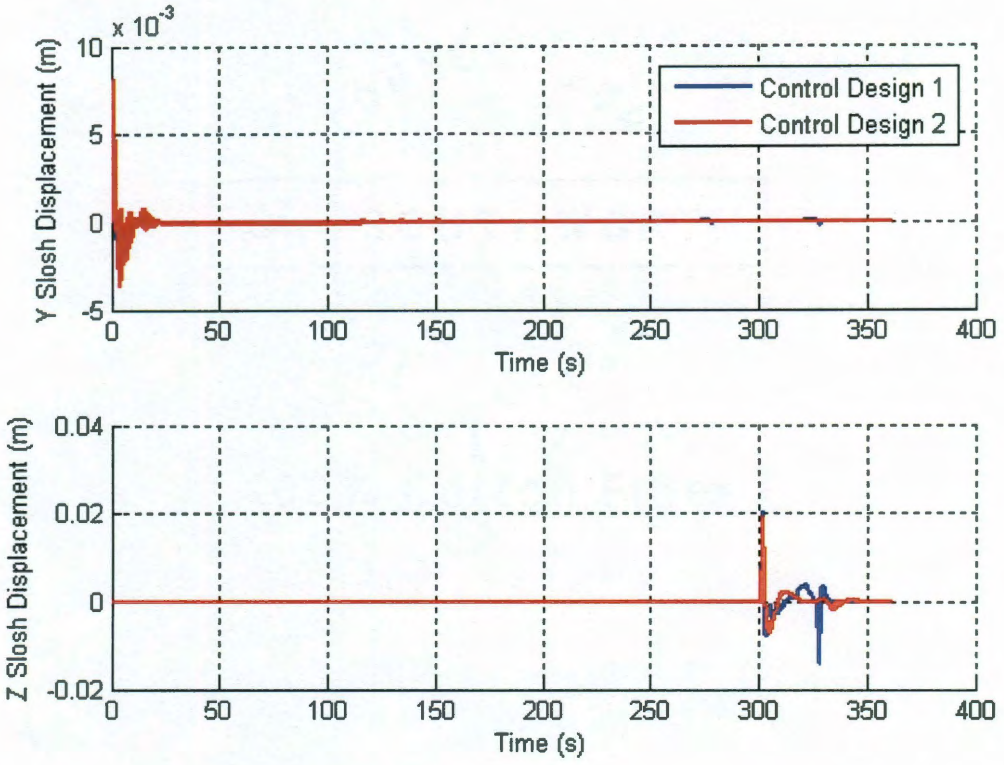

Figure 4-37: Filtered Control Design Slosh Displacements

The gimbal response shows that not only does the filter reduce the spikes and chatter seen in the unfiltered response but it also reduces the magnitude of the gimbal angle. This is because the smoothing effects of the filter limit control and instability and help reduce slosh motion. Therefore less control is required to accomplish the same task as the unfiltered design. These results show the benefits of filters as tools to increase stability increase performance and increase efficiency.

Although both filtered control designs were able to follow the trajectory it is necessary to analyze the stability margins of the designs. The stability margins of the control designs are plotted over time in Figure 4-38.

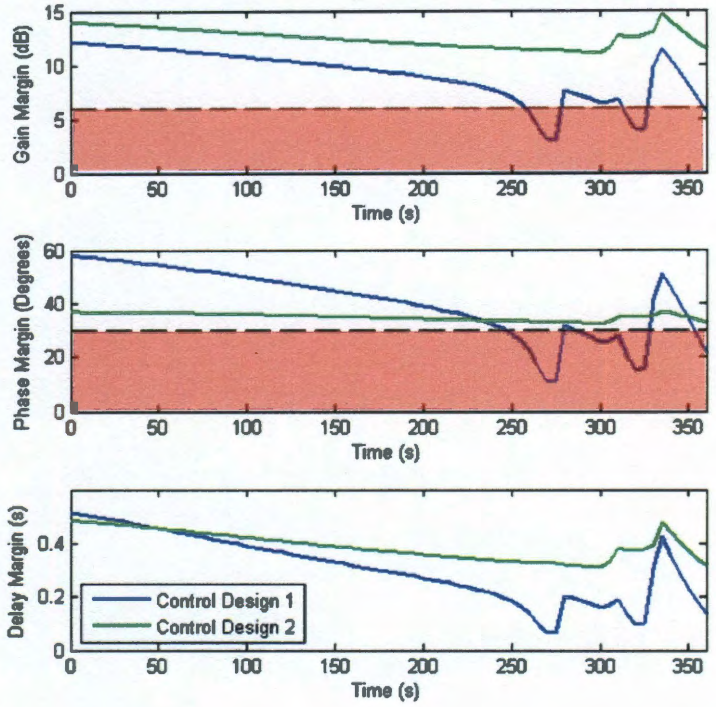

Figure 4-38: Comparison of Filtered Control Design Stability Margins for Lunar Descent Trajectory

The stability results show that control design 2 has relatively constant stability margins that are always above the minimum requirements of 6 dB gain margin and 30 degrees phase margin. The margins of control design 1 vary significantly with time and there are several portions of the flight profile where control design 1 does not meet the minimum stability requirements. This is because the guidance correction gains of control design 1 increase greatly as the vehicle approaches the end of a guidance stage. Since the gains are inversely scaled by the time to go till the stage is complete the gains become very large near the end of a stage which reduces margin. The correction gains over time are shown in Figure 4-39.

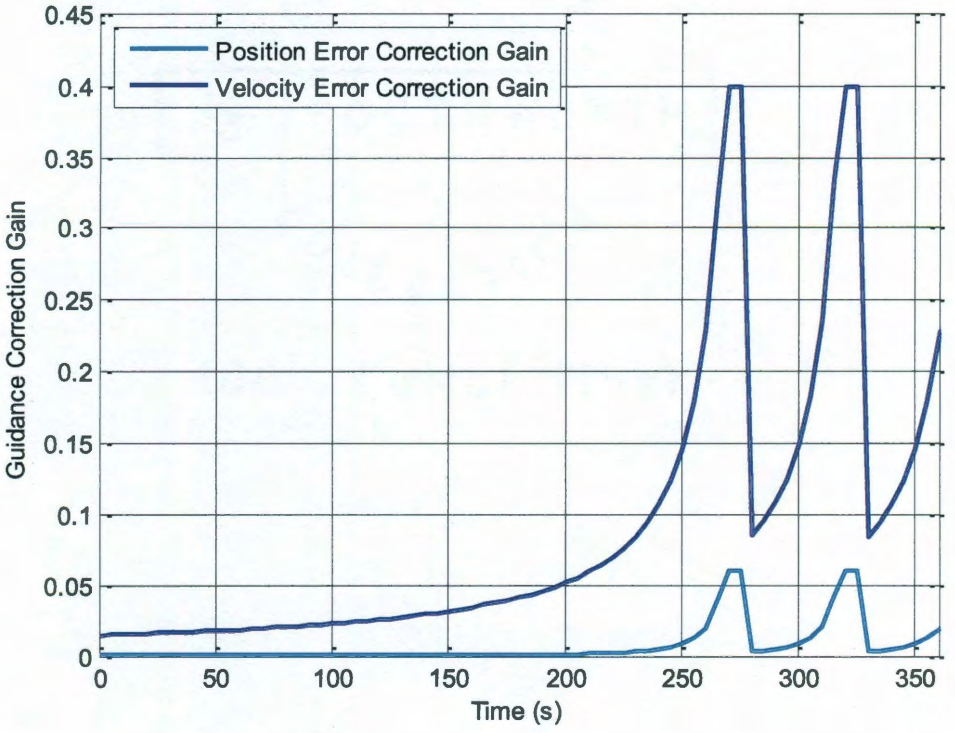

Figure 4-39: Time History of Guidance Correction Gains for Lunar Descent Trajectory

The above figure shows that as the vehicle approaches the end of a stage, the guidance correction gains of control design 1 increase exponentially. The discontinuities in the gains are present because the guidance gains are being sampled every 5 seconds. If they were sampled more frequently these discontinuities would be removed. The exponential increase of the gains of control design 1 greatly reduces the stability margins of the vehicle. This could cause the vehicle to become unstable if significant perturbations are experienced. Control design 2 maintains significant margin and therefore will be more robust and able to fly through larger disturbances.

4.6 Optimal Vehicle Geometry Design

The improvements to vehicle stability and performance through the design of optimal controllers and filters have already been shown. In order to further increase the stability and performance of the vehicle, the geometry and design of the vehicle can also be optimized. The largest source of instability is the sloshing propellant. Traditionally, slosh has been reduced through adding baffles to the propellant tanks. However, this approach only increases the effective damping of the slosh model. The location of the sloshing propellant tanks has a significant effect on the vehicle's stability. Therefore, any optimal control design should focus on placing the propellant tanks in the ideal location to limit the effects of slosh. Since the two predominant tank designs are spherical and cylindrical and each tank design has different behavior and mass properties, the results for the two tank designs will be discussed separately. Cylindrical tanks have the distinct advantage of reducing the effects of slosh since only a portion of the propellant inside them is modeled as slosh. However spherical tanks are typically able to handle greater pressures and offer the most efficient volume for carrying propellant.

4.6.1 Optimal Design for Spherical Tank Vehicle

The optimal tank configuration is dependent on the inertia and mass properties of the vehicle therefore arbitrary fixed mass properties were chosen for the vehicle. The vehicle was assumed to have two sets of coaxial propellant tanks meaning the vehicle had a total of four propellant tanks, two fuel tanks and two oxidizer tanks. The oxidizer tanks share a common axis in the body frame and the fuel tanks share a common axis in the body frame. In a typical application, the vehicle's oxidizer tanks weigh more than the

vehicle's fuel tanks and this configuration creates symmetry of the vehicle about the centerline.

The optimal vehicle geometry analysis was performed using the methods described in Chapter 3. The previous results and analysis from the filter and control designs showed that the sloshing fuel was the significant factor in determining the controllability of the vehicle. This is because the sloshing propellant creates a large amount of motion when excited by the controller. The difficulties created by slosh can be seen in the form of a spike as shown for an arbitrary tank configuration in the frequency domain in Figure 4-40.

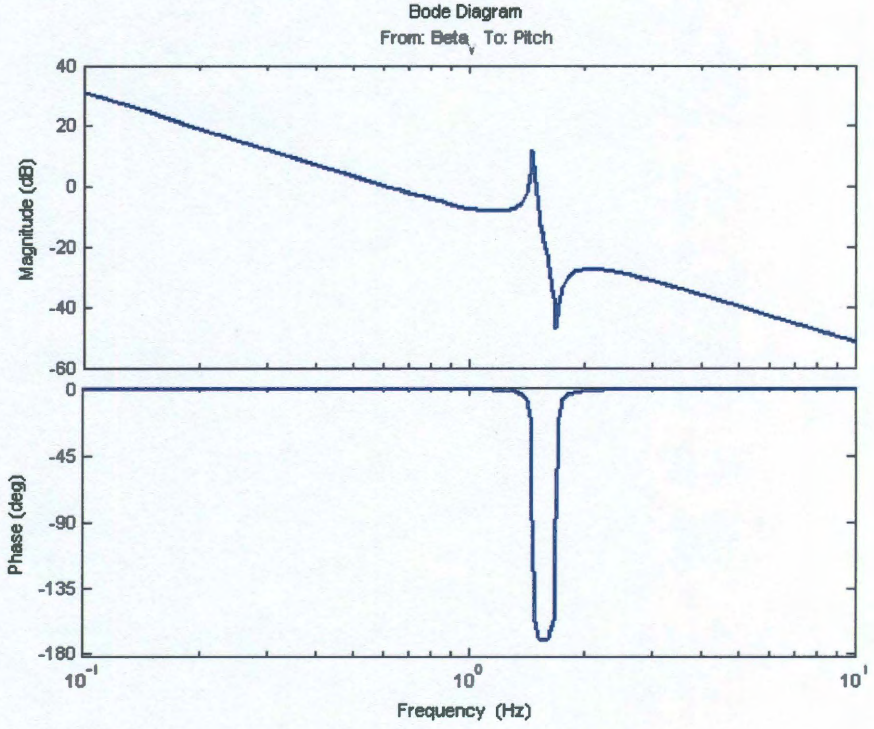

Figure 4-40: Magnitude Spike Created by Sloshing Propellant

The sloshing propellants effect on the frequency response is very significant. Therefore the optimal configuration of the tanks in terms of stability will be considered as the point where this magnitude spike is the least significant.

The spherical tanks were placed at a fixed horizontal distance from the centerline and a sweep was performed moving the tanks at an even height upwards. The tanks were then fixed in the vertical direction and moved horizontally to find the optimal configuration of the tanks with respect to vertical and horizontal position. All other parameters remained constant. This process could be iterated until the ideal location was found. During the analysis it was noted that the frequency spike began in one orientation and as the tanks vertical location was increased, the frequency spike disappeared, and then as the tanks vertical location increased further, it reappeared in the opposite orientation as before. Various propellant masses and horizontal starting distances were tested but the result always repeated itself. The location where the magnitude spike in the open loop frequency response of the plant disappeared was then referred to as the "neutral line". If the tanks were placed beneath the neutral line the magnitude spike increased on the lower frequency end and decreased on the higher frequency end. After the neutral line, the opposite was true. The behavior of the magnitude spike can be seen in Figure 4-41.

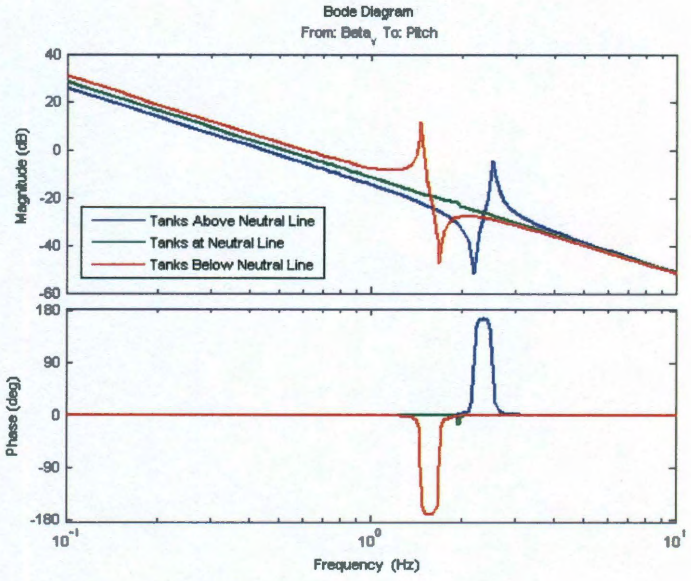

Figure 4-41: Visualization of Magnitude Spike as Tank Elevation is Changed

In order to explain why this behavior was happening pole-zero maps of the open loop plants were created. The resulting pole-zero locations are shown in Figure 4-42.

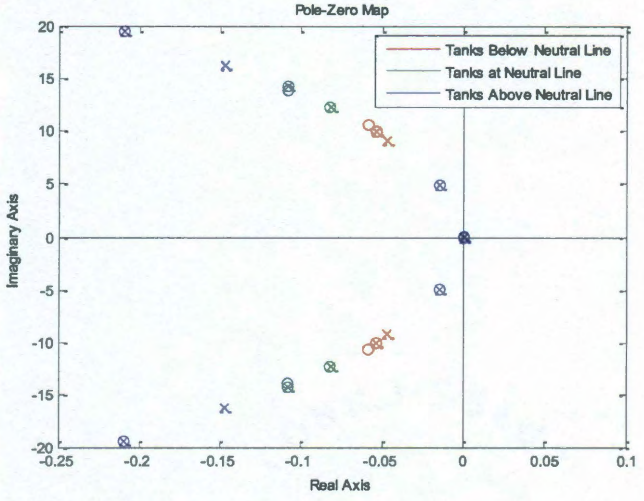

Figure 4-42: Comparison of Pole-Zero Locations as Tank Elevation is Changed

The pole-zero plots show that for the case where the tanks are at the neutral line and the spike disappears, the poles and zeros cancel each other perfectly. When the tanks are below the neutral line the free zeros are further away from the imaginary axis than the free poles. When the tanks are above the neutral line the free poles are further away than the free zeros.

A theory was developed that the removal of the spike caused by slosh was due to the tanks being located at the center of percussion. The center of percussion is the point where the translational acceleration created by a force on the body is canceled by the rotational acceleration. That is to say that no impulse is created on the body about its' point of rotation. Figure 4-43 demonstrates this concept. Assuming that O is the fixed point of rotation, C is the rigid body's center of mass, then B is the objects center of percussion where the force F, applied in the plane of rotation, generates no impulse about O. It is important to note that O is the center of percussion for point B [30].

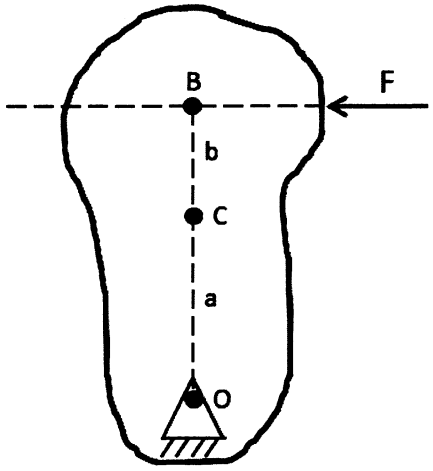

Figure 4-43: Definition of the Center of Percussion

The equation describing the location of the center of percussion is given by [30] as

$$ma = \frac{I_c}{b}, \tag{4.5}$$

where

m- Total mass of the rigid body

I_c- Inertia about the center of mass with respect to the plane of rotation

a- Length from the point of rotation O to the center of mass of the rigid body

b- Length from the center of mass of the rigid body to the center of percussion.

To apply this principle to slosh for the gimbaled vehicle, imagine point O as the gimbal point and point C as the vehicles composite center of mass. If the propellant mass center is placed at point B then by the converse property that O is the center of percussion for point B, a force applied at the gimbal O will result in no translational excitement and therefore no slosh at the point B.

Since the location of the center of percussion is relative to the center of mass and the inertia about the center of mass and both of these parameters are changing as the location of the tanks changes, it becomes an optimization problem to place the tanks at the center of percussion. In order to do this the tanks were iteratively placed at the center of percussion by minimizing the error between the tanks location and the location of the center of percussion. The tanks were then placed at the calculated center of percussion. In order to verify the theory of the center of percussion the sweep analysis was performed and the tanks were moved until the spike in the frequency response disappeared. The tank location was compared to the center of percussion location and found to be identical. The open loop Bode plots comparing the original location of the propellant tanks with Bode plots when they were placed at the center of percussion can be seen in Figure 4-44.

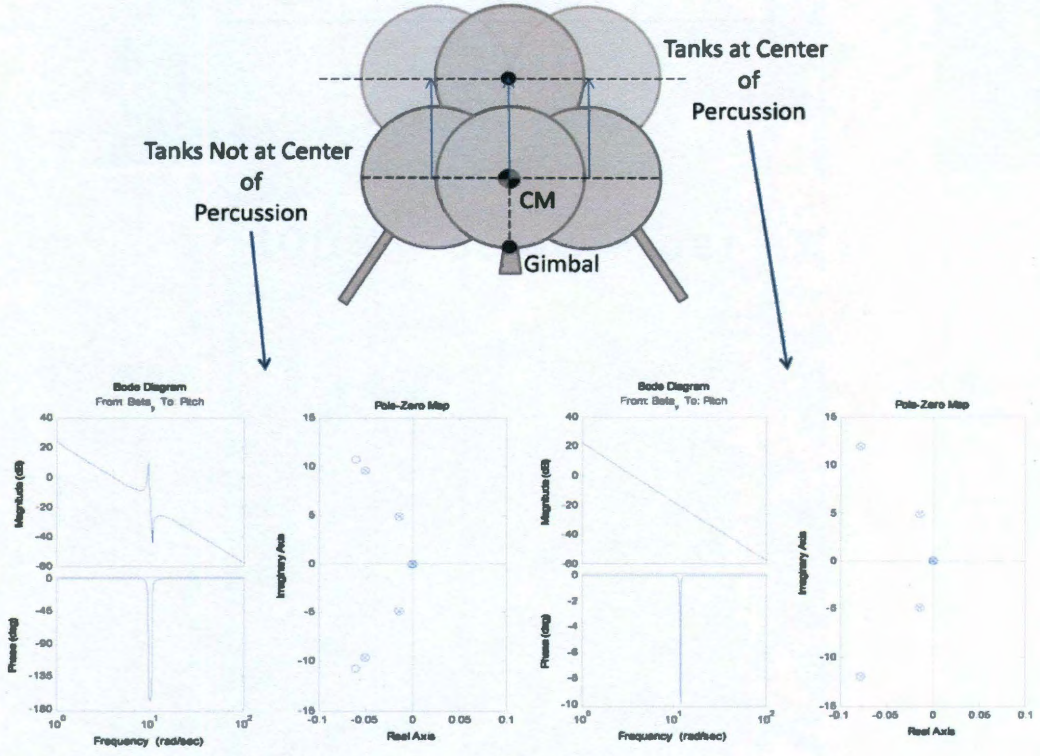

Figure 4-44: Center of Percussion Effect on Open Loop Bode Plot

This shows that the optimal location for the location of the tanks places the center of mass of the slosh at the center of percussion. There are several difficulties to implementing this in the real world. The first is that the mass of the propellant and the height of the propellant changes over time. In order to overcome this, a tank would need to be designed such that the center of mass of the propellant is always at the center of percussion. Another option would be to design the tank so that the propellant is at the center of percussion during the most critical phase of flight. Even if the propellant is not perfectly at the center of percussion the closer it is, the less the effect on slosh. The next significant issue is that of the asymmetry created by having different propellant tank masses. This will cause the inertia about one axis of rotation to be different from the

other. This means that the optimal height of the tanks for rotation about one axis will result in the tanks being located away from the optimal center of percussion when rotating about the other axis. To overcome this, the tanks could be filled to equal masses or the vehicle could be designed in such a way that the inertias are symmetric about both rotational axes. The final note of significant import is that since slosh is assumed to have no displacement in the vertical direction it is only the height of the propellant that matters, the tanks can be placed at any distance away from the vehicle so long as they are at the center of percussion. For each incremental distance away from the vehicle the tanks are there is a center of percussion for which the tank location is optimal. The optimal location of the sloshing propellant center of mass for a four tank design with various total vehicle propellant loads relative to the mass of the airframe is shown in Figure 4-45. The total propellant mass m_{prop} of all four tanks for each optimal location curve is set equal to a proportion of the vehicles airframe mass m_a.

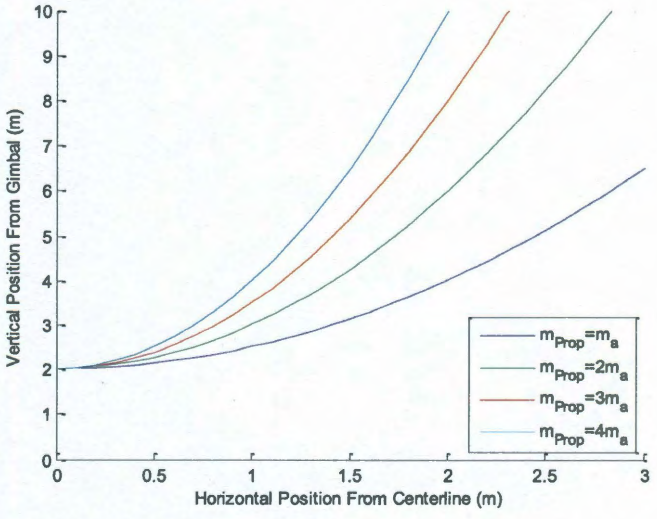

Figure 4-45: Optimal Location of Individual Propellant Center of Mass for Various Total Propellant Loads for Spherical Tanks

It is important to note that this chart shows the optimal individual location for one of the four total tanks even though the various propellant loads in the legend are in terms of the total mass of all four tanks. This chart allows the tanks to be located in the optimal horizontal location to meet mission and launch vehicle requirements and the optimal vertical location of the propellant tanks will then be defined.

4.6.2 Optimal Design for Cylindrical Tank Vehicle

A sweep analysis for cylindrical tanks was also performed. The resulting determination was that the optimal location for the cylindrical tanks should also be to place the slosh mass at the center of percussion just as was done with the optimal spherical tank design. The only difference is that now the sloshing propellant is not the entire slosh mass and therefore it is only a small percentage of the total propellant mass. Therefore unlike the spherical tanks where the propellant center of mass needed to be placed at the center of percussion, for cylindrical tanks the center of mass of only the slosh component of the propellant needs to be located at the center of percussion. A visualization of this is shown in Figure 4-46.

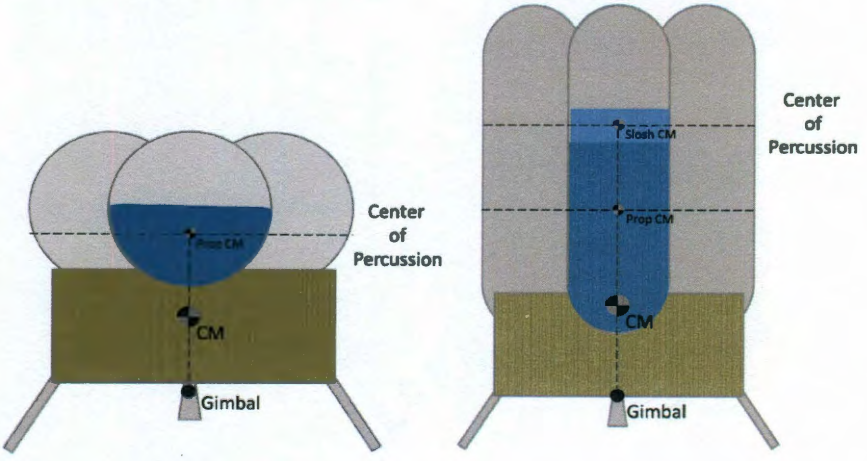

Figure 4-46: Comparison of Tank Geometry Optimal Locations

A script file was developed similar to the one used to place the propellant center of mass at the center of percussion for the spherical tanks. The resulting optimal vertical locations of the slosh center of mass for various propellant loads with respect to horizontal distances from the centerline are shown in Figure 4-47. The total propellant mass m_{prop} of all four tanks for each optimal location curve is again set equal to a proportion of the vehicles airframe mass m_a.

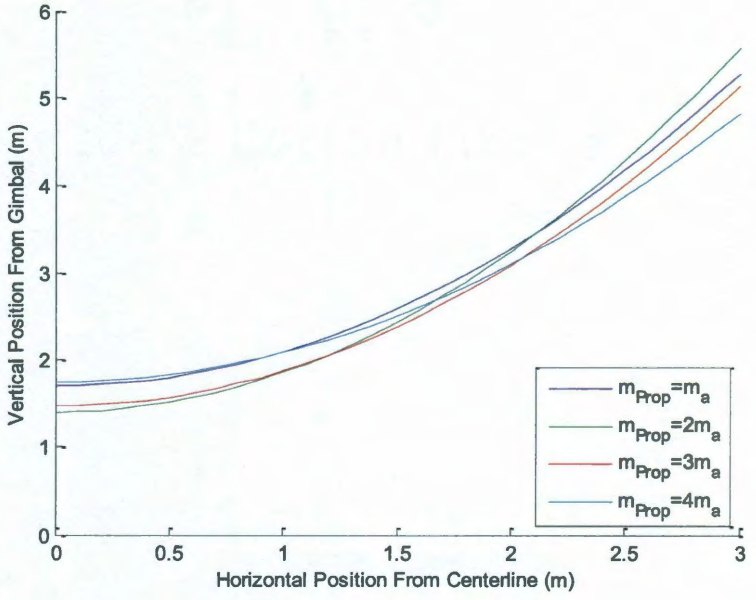

Figure 4-47: Optimal Location of Individual Slosh Mass Center of Mass for Various Total Propellant Loads for Cylindrical Tanks

This shows that the optimal locations for the slosh center of mass are very different than the spherical tank analysis. The optimal location for the slosh center of mass for cylindrical tanks is significantly lower than the optimal location for spherical tanks. Additionally, the optimal location curves shown in Figure 4-47 change shape and shift depending on the proportion of propellant mass compared to the airframe mass. This

phenomena was not observed for spherical tanks. This occurs because the apparent slosh mass of a cylindrical tank is only a portion of the height of the propellant in the tank. As the fluid level in the tank is increased, the amount of relative slosh mass does not necessarily increase linearly. Since the optimal location is a function of inertia and composite center of mass both of which vary nonlinearly as the propellant load and tank locations change, this creates the shifts and shape changes in the optimal location plots shown above.

4.6.3 Comparison of Spherical and Cylindrical Tanks

In general it is economic and simpler to use spherical tanks. However, if stability and slosh is of major concern as is the case with a gimbaled engine vehicle of this design, then cylindrical tanks are advantageous. The cylindrical tanks have only a small percentage of the propellant that is considered slosh mass. Cylindrical tanks also have significantly lower optimal locations than spherical tanks. These observations have several beneficial implications since not only can the propellant tanks be placed lower on the vehicle which saves space, but the effects of the slosh are minimized because only a small mass is considered dynamic. For these reasons from a stability standpoint, it is beneficial to use cylindrical tanks compared to spherical tanks.

5 Closure

The goal of this thesis has been to develop robust control designs for gimbaled rocket engine vehicles. Control designs using a traditional GNC architecture have been examined as the legacy approach to the control of the vehicle's thrust and gimbal angle. This thesis has also examined new control designs that gave the controller full capability to manipulate all of the vehicle states through controlling the vehicle's thrust and gimbal angles. The importance and design of filters to improve vehicle stability and performance have also been examined. Additionally, a study has been performed to determine the optimal vehicle configurations for both spherical and cylindrical propellant tanks in order to reduce slosh and increase stability.

The historical legacy approach of control design 1 has been found able to follow the trajectories with only a small amount of error when there were no disturbances on the vehicle. This design has the benefit of a guidance correction that is scaled by time ensuring in theory that the vehicle arrives at the correct state by the desired time. However, because the gains on the guidance correction in the legacy architecture become extremely large as the vehicle approaches the end of the stage, the vehicle inherently approaches instability as the stability margins of the closed loop system are greatly reduced. When disturbances were not enforced on the vehicle and its sensors the lack of margin was not as significant of an issue. Once disturbances were added to the vehicle the issues created by the reduced stability margins were obvious. Although the vehicle never went fully unstable during the Monte Carlo simulation, large errors were seen in the vehicle states as they approached the terminal point of each stage of the trajectory.

These errors degraded the vehicle performance and led to inefficiencies that increase fuel consumption and could possibly endanger the vehicle.

The proposed new approach of control design 2 has been found able to follow all of the trajectories with minimal error. The benefit of this design is that the controller is able to actually control all states of the vehicle. In the legacy approach as seen in control design 1, the controller did not have full control of the vehicle because it did not have the ability to directly control thrust. Instead the thrust was pre-determined by guidance and the controller was forced to output that thrust. Control design 2 only required the guidance block to tell the controller where the vehicle should go. Then, using state information the controller was able to determine the necessary thrust, follow the trajectory, and correct for any significant position or velocity errors. The improved performance of the new control approach is best shown when there are disturbances on the vehicle. The Monte Carlo analysis showed that control design 2 provided significantly less error in all directions than control design 1. Additionally, control design 2 provides nearly constant stability margins throughout the flight which exceed the minimum margins at all times. This is beneficial because unlike the legacy approach, the new design does not fly in and out of periods of stability which greatly improves performance, safety, and efficiency of the vehicle.

The advantages of control design 2 with regards to throttle control have been clearly demonstrated. Control design 1 is significantly less able to fly a given trajectory with error in the engine. In the real world this would require that expensive and labor intensive analysis be performed on the rocket engine in order to confidently fly the legacy design. Control design 2 is able to handle all thrust perturbations extremely well with

minimum variation. This new approach requires almost no analysis of the engine performance and is still able to follow the trajectory almost flawlessly.

Filters not only increase the stability margins of the system but they also smooth out the vehicle control response which further adds to stability by reducing slosh. Although for certain vehicle designs where slosh has high damping or the controller is designed well enough a filter is not necessary in simulation, it is highly recommended to design and fly filters in real applications. The added benefits of increased stability and the smoothing effects of the filter help reject real world disturbances that are encountered and may even help eliminate unforeseen difficulties that could not be modeled or observed in simulation.

The optimal vehicle configuration analysis of this thesis has revealed that there is an optimal location to place the vehicle tanks to increase the stability of the vehicle and reduce the effects of slosh. This optimal tank location is the location such that the center of mass of the sloshing propellant is at the vehicle's center of percussion. For spherical tanks the problem is relatively simple because the slosh center of mass is the center of mass of all of the propellant in the tank. For cylindrical tanks the problem becomes slightly more complex since the effective slosh center of mass is a function of the density of the propellant, radius of the tank, and height of the liquid in the tank. A challenge to placing the slosh center of mass at the center of percussion is that these parameters vary with time. This means that the effects of slosh will only be eliminated at one propellant level. Further analysis could be done in order to determine an optimal shape of the tank to eliminate slosh at all points however the complexity of this shape in the application of a pressure vessel may prove to be not worth the design cost. Another option would be to

place the tanks at a particular location such that slosh was reduced the most during a critical point in the flight or even simpler at the middle point of propellant use so as to average the reduction in slosh over the trajectory.

Ultimately, the exploration of the controller and filter designs in terms of stability and performance as well as the analysis of the optimal propellant tank configuration provide several viable options to improve vehicle designs and GNC architectures for a gimbaled engine rocket. The proposed new GNC architecture offers a way to pre-plan trajectories through guidance and the controller provide the inputs to fly these trajectories. Further exploration into this topic should explore the problem of optimal real time control. Optimal terminal control could solve the problem of how to get to a specified target or set of target waypoints without the need for preplanning trajectories. This could allow for true autonomy where the vehicle would essentially only need to be programmed with a final destination ahead of time. The vehicle could then calculate the optimal control to arrive at that terminal state on the fly. The waypoints or terminal destination could be updated in the middle of the flight if necessary. This autonomy could prove extremely beneficial for many applications both on this planet and away from it.

The analysis and methods developed in this thesis are not limited to the problem of a gimbaled engine lander. The linear state-space model could be adapted for use on a vehicle with any number of sloshing propellant tanks, vehicle mass properties, or type of propulsion. The same architectures developed in this thesis could be expanded with only minor effort to develop optimal GNC architectures for launch vehicles, helicopters, ducted fan vehicles, or any other application of a gimbaled engine vehicle that may exist.

The future applications of this thesis are therefore only bounded by the creativity and technological advances of the vehicles this world can create.

Bibliography

[1] J. Sellers, W. Astore, R. Giffen, and W. Larson, *Understanding Space: An Introduction to Astronautics*, 3rd ed. Learning Solutions, 2007.

[2] C. S. Draper et al., "Apollo Guidance and Navigation," *Space Navigation and Control*, vol. 1, Jun. 1965.

[3] K. R. Duda, M. C. Johnson, and T. J. Fill, "Design and Analysis of Lunar Lander Manual Control Modes," presented at the IEEE/AIAA Aerospace Conference, Big Sky, MT, 2008, p. 1–16.

[4] M. C. Johnson, "A Parameterized Approach to the Design of Lunar Lander Attitude Controllers," presented at the AIAA Guidance, Navigation, and Control Conference and Exhibit, Keystone, CO, 2006.

[5] W. J. Larson and J. R. Wertz, *Space Mission Analysis and Design, 3rd edition*, 3rd ed. Microcosm Press, 1999.

[6] A. Klumpp, "Apollo Lunar Descent Guidance," *Automatica*, vol. 10, pp. 133-146, 1974.

[7] S. R. Ploen and A. Behcet A., Aron, "A Comparison of Powered Descent Guidance Laws for Mars Pinpoint Landing," presented at the AIAA/AAS Astrodynamics Specialist Conference and Exhibit, Keystone, CO, 2006, pp. 1-16.

[8] R. D. Braun, with B. A. Steinfeldt and M. J. Grant, Daniel A., "Guidance, Navigation, and Control System Performance Trades for Mars Pinpoint Landing," *Journal of Spacecraft and Rockets*, Jun. 2009.

[9] S. H. Crandall, *Dynamics of Mechanical and Electromechanical Systems*. Krieger Pub Co, 1982.

[10] R. D. Knight, *Physics for Scientists and Engineers: A Strategic Approach*, United States ed. Addison Wesley, 2003.

[11] W. Harris, "Comparison of Guidance Methods for an Autonomous Planetary Lander," Rice University, 2011.

[12] J. A. Frosch and D. P. Vallely, "Saturn AS-501/S-IC Flight Control System Design," *Journal of Spacecraft*, vol. 4, pp. 1003-1009, Aug. 1967.

[13] B. Noble, *Applied Linear Algebra 2ND Edition*. Prentice Hall, 1977.

[14] P. Mitiguy, *Advanced Dynamics & Motion Simulation For Propfessional Mechanical, Aerospace, and Biomechanical Engineers*, Student Edition. Stanford University, 2009.

[15] B. Friedland, *Control System Design: An Introduction to State-Space Methods*. Dover Publications, 2005.

[16] J. G. Reid, *Linear System Fundamentals: Continuous and Discrete, Classic and Modern*. McGraw-Hill Companies, 1983.

[17] W. S. Levine, *The Control Handbook*. Jaico Publishing House, 2005.

[18] J. B. Kuipers, *Quaternions and Rotation Sequences: A Primer with Applications to Orbits, Aerospace and Virtual Reality*. Princeton University Press, 2002.

[19] N. S. Nise, *Control Systems Engineering, 4th Edition*, 4th ed. Wiley, 2003.

[20] D. McClean, *Automatic Flight Control Systems*. Prentice Hall, 1990.

[21] R. Humble, G. Henry, and W. Larson, *Space Propulsion Analysis and Design with Website*, 1st ed. Learning Solutions, 2007.

[22] F. T. Dodge, "The New 'Dynamic Behavior of Liquids in Moving Containers'," *Southwest Research Institute, San Antonio, Texas*, 2000.

[23] P. C. Hughes, *Spacecraft Attitude Dynamics*. Dover Publications, 2004.

[24] I. Elishakoff, *Probabilistic Theory of Structures*, 2nd ed. Dover Publications, 1999.

[25] D. A. Vallado, *Fundamentals of Astrodynamics and Applications*, 3rd ed. Microcosm Press/Springer, 2007.

[26] C. L. Chiang, *Statistical Methods of Analysis*, 1st ed. World Scientific Publishing Company, 2003.

[27] G. P. Sutton and O. Biblarz, *Rocket Propulsion Elements, 7th Edition*, 7th ed. Wiley-Interscience, 2000.

[28] R. E. Ziemer and W. H. Tranter, *Principles of Communication: Systems, Modulation and Noise, 5th Edition*, 5th ed. Wiley, 2001.

[29] R. D. Strum and D. E. Kirk, *First Principles of Discrete Systems and Digital Signal Processing*. Prentice Hall, 1988.

[30] D. T. Greenwood, *Principles of Dynamics*, 2nd ed. Prentice Hall, 1987.